

**A COMPARATIVE STUDY ON THE PHOTOCATALYTIC  
DEGRADATION OF ORGANIC DYE IN THE PRESENCE OF  
BIOCHAR COMPOSITES USING VARIOUS OXIDANTS**

**LAW ZHI XUAN**

**A project report submitted in partial fulfilment of the  
requirements for the award of Bachelor of Engineering  
(Honours) Chemical Engineering**

**Lee Kong Chian Faculty of Engineering and Science  
Universiti Tunku Abdul Rahman**

**April 2020**

**DECLARATION**

I hereby declare that this project report is based on my original work except for citations and quotations which have been duly acknowledged. I also declare that it has not been previously and concurrently submitted for any other degree or award at UTAR or other institutions.

Signature :   
\_\_\_\_\_

Name : Law Zhi Xuan  
\_\_\_\_\_

ID No. : 1503433  
\_\_\_\_\_

Date : 12/5/2020  
\_\_\_\_\_

**APPROVAL FOR SUBMISSION**

I certify that this project report entitled “**A COMPARATIVE STUDY ON THE PHOTOCATALYTIC DEGRADATION OF ORGANIC DYE IN THE PRESENCE OF BIOCHAR COMPOSITES USING VARIOUS OXIDANTS**” was prepared by **LAW ZHI XUAN** has met the required standard for submission in partial fulfilment of the requirements for the award of Bachelor of Engineering (Honours) Chemical Engineering at Universiti Tunku Abdul Rahman.

Approved by,

Signature :   
\_\_\_\_\_

Supervisor : Dr Pang Yean Ling

Date : 15/5/2020

Signature :   
\_\_\_\_\_

Co-Supervisor : Dr Shuit Siew Hong

Date : 15/5/2020

The copyright of this report belongs to the author under the terms of the copyright Act 1987 as qualified by Intellectual Property Policy of Universiti Tunku Abdul Rahman. Due acknowledgement shall always be made of the use of any material contained in, or derived from, this report.

© 2020, Law Zhi Xuan. All right reserved.

## **ACKNOWLEDGEMENTS**

I would like to thank everyone who had contributed to the successful completion of this project. I would like to express my gratitude to my research supervisor, Dr. Pang Yean Ling and co-supervisor, Dr. Shuit Siew Hong for their invaluable advice, guidance and enormous patience throughout the development of the research.

## ABSTRACT

The conversion of carbon-rich biomass into valuable material is an environmentally-friendly way for its utilization. In this study, coconut shell-derived biochar, graphitic carbon nitride (g-C<sub>3</sub>N<sub>4</sub>), g-C<sub>3</sub>N<sub>4</sub>/biochar, titanium dioxide (TiO<sub>2</sub>)/biochar, zinc oxide (ZnO)/biochar and ferric oxide (Fe<sub>2</sub>O<sub>3</sub>)/biochar were synthesized and characterized by using scanning electron microscopy coupled with energy-dispersive X-ray spectroscopy (SEM-EDX), X-ray diffraction (XRD), Fourier-transform infrared spectroscopy (FTIR), thermogravimetric analysis (TGA), surface area analysis using Branauer-Emmett-Teller (BET) method, UV-Vis diffuse reflectance spectroscopy (DRS) and zeta potential analysis. The SEM images illustrated the porous structure of biochar, flakes-like structure of g-C<sub>3</sub>N<sub>4</sub> and the immobilization of nanometer-sized metal oxides on the biochar. The XRD and FTIR results of composite materials showed characteristic peaks of g-C<sub>3</sub>N<sub>4</sub> and other metal oxides, indicated that g-C<sub>3</sub>N<sub>4</sub> and metal oxides were well-immobilized on the biochar. TGA results presented the improvement of thermal stability of g-C<sub>3</sub>N<sub>4</sub>/biochar as compared to pure g-C<sub>3</sub>N<sub>4</sub>. Surface area analysis results showed that biochar could increase the specific surface area and average pore volume of catalyst sample. The band gap energies of g-C<sub>3</sub>N<sub>4</sub>, g-C<sub>3</sub>N<sub>4</sub>/biochar, TiO<sub>2</sub>/biochar, ZnO/biochar and Fe<sub>2</sub>O<sub>3</sub>/biochar were found to be 2.7 eV, 2.47 eV, 3.17 eV, 3.02 eV and 2.11 eV, respectively. Furthermore, zeta potential analysis proved that catalyst presented positively charged surface under acidic conditions, which favour the adsorption and subsequent degradation of anionic dye. Among different biochar composites, g-C<sub>3</sub>N<sub>4</sub>/biochar was found to be the best photocatalyst in the degradation of Methyl Orange. Besides, it was found that peroxymonosulfate (PMS) oxidizing agent could oxidized Methyl Orange better as compared to hydrogen peroxide (H<sub>2</sub>O<sub>2</sub>) and persulfate (PS), owing to the huge amount of hydroxyl radical (•OH) and sulphate radical (SO<sub>4</sub>•<sup>-</sup>) generated. The effect of parameters such as catalyst dosage (0, 0.25, 0.50, 0.75, 1.0 and 1.25 g/L), PMS oxidant dosage (0, 0.2, 0.4, 0.6, 0.8 and 1.0 mM) and solution pH (pH 1, 3, 5, 7, 9 and 11) on the photocatalytic degradation of Methyl Orange were investigated. The highest degradation efficiency (92.71 %) was achieved at catalyst dosage of 0.75 g/L, PMS oxidant dosage of 0.6 mM and solution pH

3, which were further validated by using response surface methodology (RSM). According to the results of RSM, degradation efficiency of 96.63 % could be obtained under the optimum parameter condition (catalyst dosage of 0.75 g/L, PMS oxidant dosage of 0.57 mM and solution pH 3.48). In addition, the photocatalytic degradation of Methyl Orange using g-C<sub>3</sub>N<sub>4</sub>/biochar was found to have follow pseudo first order kinetic model. The overall chemical oxygen demand (COD) removal efficiency under the optimum operating condition was found to be 67.2 %. In short, g-C<sub>3</sub>N<sub>4</sub>/biochar could be a promising material in wastewater treatment process due to its good photocatalytic activity.

## TABLE OF CONTENTS

<b>DECLARATION</b>		<b>i</b>
<b>APPROVAL FOR SUBMISSION</b>		<b>ii</b>
<b>ACKNOWLEDGEMENTS</b>		<b>iv</b>
<b>ABSTRACT</b>		<b>v</b>
<b>TABLE OF CONTENTS</b>		<b>vii</b>
<b>LIST OF TABLES</b>		<b>x</b>
<b>LIST OF FIGURES</b>		<b>xi</b>
<b>LIST OF SYMBOLS / ABBREVIATIONS</b>		<b>xiv</b>
<b>LIST OF APPENDICES</b>		<b>xvii</b>
<b>CHAPTER</b>		
<b>1</b>	<b>INTRODUCTION</b>	<b>1</b>
1.1	Water Pollution in Malaysia	1
1.2	Background of Dyes	2
1.3	Dye Removal Method	5
1.3.1	Biological Removal Method	5
1.3.2	Physical Removal Method	6
1.3.3	Chemical Removal Method	7
1.4	Problem Statement	8
1.5	Aim and Objectives	9
1.6	Scopes of the Study	9
<b>2</b>	<b>LITERATURE REVIEW</b>	<b>11</b>
2.1	Biochar	11
2.1.1	Biochar vs Activated Carbon	13
2.1.2	Activation of Biochar	14
2.2	Metal Oxide and Non-Metal Based Photocatalyst	15
2.3	Biochar Composites	16
2.4	Characterization of Catalyst	17

2.4.1	Scanning Electron Microscopy with Energy Dispersive X-Ray (SEM-EDX)	17
2.4.2	X-Ray Diffraction (XRD)	20
2.4.3	Fourier-Transform Infrared Spectroscopy (FTIR)	21
2.4.4	Thermogravimetric Analysis (TGA)	23
2.4.5	Surface Area Analysis	24
2.5	Advanced Oxidation Processes (AOPs)	25
2.5.1	Photolysis	27
2.5.2	Photocatalysis	27
2.5.3	Other Advanced Oxidation Processes	29
2.6	Design of Experiment	31
2.7	Parameter Studies	34
2.7.1	Effect of Different Types of Oxidants	34
2.7.2	Effect of Catalyst Dosage	35
2.7.3	Effect of Oxidant Dosage	36
2.7.4	Effect of Solution pH	37
2.8	Kinetic Study	37
<b>3</b>	<b>METHODOLOGY AND WORK PLAN</b>	<b>39</b>
3.1	Materials and Chemicals	39
3.2	Equipment	40
3.3	Overall Experiment Flowchart	40
3.4	Experimental Setup	41
3.5	Synthesis of Catalysts	43
3.5.1	Synthesis of Biochar from Coconut Shell	43
3.5.2	Synthesis of Biochar Composites	43
3.6	Characterization of Catalysts	44
3.7	Parameter Studies	46
3.7.1	Effect of Different Types of Catalyst	46
3.7.2	Effect of Different Types of Oxidant	46
3.7.3	Effect of Catalyst Dosage	46
3.7.4	Effect of Oxidant Dosage	47
3.7.5	Effect of Solution pH	47
3.8	Design of Experiment	47

3.9	Kinetic Study	48
3.10	Liquid Sample Analysis	50
<b>4</b>	<b>RESULTS AND DISCUSSION</b>	<b>52</b>
4.1	Characterization of Catalysts	52
4.1.1	SEM-EDX	52
4.1.2	XRD	54
4.1.3	FTIR	57
4.1.4	TGA	58
4.1.5	Surface Area Analysis	59
4.1.6	UV-Vis Diffuse Reflectance Spectroscopy (DRS)	61
4.1.7	Zeta Potential Analysis	63
4.2	Parameter Studies	65
4.2.1	Effect of Different Types of Catalyst	65
4.2.2	Effect of Different Types of Oxidant	66
4.2.3	Effect of Catalyst Dosage	67
4.2.4	Effect of Oxidant Dosage	69
4.2.5	Effect of Solution pH	70
4.3	Optimization Studies	71
4.3.1	Regression Analysis	71
4.3.2	Response Surface Analysis	75
4.3.3	Model Validation and Experimental Confirmation	78
4.4	Kinetic Studies	79
4.5	Chemical Oxygen Demand (COD) Removal	81
<b>5</b>	<b>CONCLUSIONS AND RECOMMENDATIONS</b>	<b>83</b>
5.1	Conclusions	83
5.2	Recommendations for future work	84
	<b>REFERENCES</b>	<b>85</b>
	<b>APPENDICES</b>	<b>94</b>

## LIST OF TABLES

Table 1.1:	Classification of Dyes Based on Application (Adegoke and Bello, 2016)	3
Table 1.2:	Fixation Degree of Dyes on Textile (Ammayappan, Jose and Raj, 2016)	4
Table 2.1:	Elemental Composition of Raw Biomass (Cagnon, et al., 2009)	12
Table 2.2:	Infrared Radiation Absorption of Common Functional Groups (Winter, 2016)	22
Table 2.3:	Oxidation Potential of Common Oxidants (Rodriguez, et al., 2008)	26
Table 3.1:	Materials and Chemicals Used in Experiment	39
Table 3.2:	Properties of Methyl Orange	40
Table 3.3:	Instruments Used in Experiment	41
Table 3.4:	Actual Values of Variables and Their Coded Levels Used in CCD	48
Table 3.5:	Experiment Matrix of CCD	49
Table 4.1:	EDX Results of Different Catalysts	55
Table 4.2:	Surface Area Analysis Results of Different Catalyst	59
Table 4.3:	Experimental Results for the Three Independent Variables	72
Table 4.4:	ANOVA Results for Photocatalytic Degradation Efficiency of Methyl Orange	74
Table 4.5:	Experimental and Predicted Results Conducted at Optimized Condition for Model Validation	78
Table 4.6:	Rate Coefficient for Photocatalytic Degradation of Methyl Orange Under Different Temperature	80

## LIST OF FIGURES

Figure 1.1:	Assessment of Pollution Load by Source of Water Pollution in 2017 (DOE, 2018)	2
Figure 2.1:	Specimen Interaction of SEM-EDX (Challa, 2009)	18
Figure 2.2:	X-ray Generation Process (Nanakoudis, 2018)	18
Figure 2.3:	SEM Image of (a) Biochar (b) TiO <sub>2</sub> /biochar (Khataee, et al., 2017)	19
Figure 2.4:	EDX Spectrum of TiO <sub>2</sub> /biochar (Khataee, et al., 2017)	19
Figure 2.5:	XRD Patterns of ZnO/biochar, ZnO and Biochar (Gholami, et al., 2019)	21
Figure 2.6:	Spectra for Biochar and Fe <sub>2</sub> O <sub>3</sub> /Biochar (Chaukura, Murimba and Gwenzim 2015)	23
Figure 2.7:	Plot of Mass Change Against Temperature (Guwahati, 2016)	23
Figure 2.8:	TGA Analysis of Biochar and Iron-modified Biochar (Sun, et al., 2019)	24
Figure 2.9:	Hydrogen Atoms Abstraction (Ragnar, et al., 1999)	27
Figure 2.10:	Mechanism of Photocatalytic Oxidation	28
Figure 2.11:	Degradation of Red 2G by Hydroxyl and Peroxyl Radicals (Bruin, 2015)	29
Figure 2.12:	Mechanism of Sonolysis Oxidation (Wang and Xu, 2012)	31
Figure 2.13:	CCD model	32
Figure 2.14:	Response Surface and Contour Plots (Mortazavian, Saber and James, 2019)	34
Figure 3.1:	Overall Research Flowchart on This Study	42
Figure 3.2:	Schematic Diagram for Photocatalytic Degradation of Dyes	43

Figure 4.1:	SEM Images of (a) Biochar, (b) g-C <sub>3</sub> N <sub>4</sub> , (c) g-C <sub>3</sub> N <sub>4</sub> /biochar, (d) TiO <sub>2</sub> /biochar, (e) ZnO/biochar and (f) Fe <sub>2</sub> O <sub>3</sub> /biochar	53
Figure 4.2:	XRD patterns of (a) Biochar, (b) g-C <sub>3</sub> N <sub>4</sub> , (c) g-C <sub>3</sub> N <sub>4</sub> /biochar, (d) TiO <sub>2</sub> /biochar, (e) ZnO/biochar and (f) Fe <sub>2</sub> O <sub>3</sub> /biochar	56
Figure 4.3:	FTIR Spectra of (a) Biochar, (b) g-C <sub>3</sub> N <sub>4</sub> , (c) g-C <sub>3</sub> N <sub>4</sub> /biochar, (d) TiO <sub>2</sub> /biochar, (e) ZnO/biochar and (f) Fe <sub>2</sub> O <sub>3</sub> /biochar	57
Figure 4.4:	TGA Plot of Different Catalyst	58
Figure 4.5:	Nitrogen Adsorption-Desorption Isotherms on the Surface of Different Catalyst	60
Figure 4.6:	Pore Size Distribution of Biochar, g-C <sub>3</sub> N <sub>4</sub> , g-C <sub>3</sub> N <sub>4</sub> /biochar, TiO <sub>2</sub> /biochar, ZnO/biochar and Fe <sub>2</sub> O <sub>3</sub> /biochar	61
Figure 4.7:	Absorbance Spectra of g-C <sub>3</sub> N <sub>4</sub> , g-C <sub>3</sub> N <sub>4</sub> /biochar, TiO <sub>2</sub> /biochar, ZnO/biochar and Fe <sub>2</sub> O <sub>3</sub> /biochar	62
Figure 4.8:	Band Gap Energy of (a) g-C <sub>3</sub> N <sub>4</sub> , (b) g-C <sub>3</sub> N <sub>4</sub> /biochar, (c) TiO <sub>2</sub> /biochar, (d) ZnO/biochar and (e) Fe <sub>2</sub> O <sub>3</sub> /biochar	63
Figure 4.9:	Zeta Potential of Biochar, g-C <sub>3</sub> N <sub>4</sub> and g-C <sub>3</sub> N <sub>4</sub> /biochar	64
Figure 4.10:	Effect of Different Catalyst on the Photocatalytic Degradation of Methyl Orange (Catalyst Dosage = 1 g/L, Natural Solution pH)	65
Figure 4.11:	Effect of Different Oxidant on the Photocatalytic Degradation of Methyl Orange (Catalyst Dosage = 1 g/L, Oxidant Dosage = 1 mM, Natural Solution pH = 6.5)	67
Figure 4.12:	Effect of Catalyst Dosage on the Photocatalytic Degradation of Methyl Orange (Oxidant Dosage = 1 mM, Natural Solution pH = 6.5)	68
Figure 4.13:	Effect of Oxidant Dosage on the Photocatalytic Degradation of Methyl Orange (Catalyst Dosage = 0.75 g/L, Natural Solution pH = 6.5)	69

Figure 4.14: Effect of Solution pH on the Photocatalytic Degradation of Methyl Orange (Catalyst Dosage = 0.75 g/L, Oxidant Dosage = 0.6 mM)	70
Figure 4.15: Predicted and Actual Values for Photocatalytic Degradation of Methyl Orange ( $R^2 = 0.9989$ )	75
Figure 4.16: Perturbation Plot for Three Factors Study	76
Figure 4.17: Effect of Three Factors on the Photocatalytic Degradation of Methyl Orange at Fixed (a) Solution pH 3 (b) Oxidant Dosage 0.4 mM and (c) Catalyst Dosage 0.5 g/L	77
Figure 4.18: Pseudo First Order Reaction Kinetic Plot for Photocatalytic Degradation of Methyl Orange	79
Figure 4.19: Arrhenius Plot of $\ln k_{app}$ versus $1/T$	81
Figure 4.20: COD Removal Efficiencies of Methyl Orange (Adsorption = -30 to 0 min ; Degradation = 0 to 120 min)	82

**LIST OF SYMBOLS / ABBREVIATIONS**

$\eta$	order of reflection
$\lambda$	wavelength
$d$	lattice spacing
$\theta$	angle
$L$	crystallite size
$K$	shape factor
$B$	peak width
$X$	weight of nitrogen adsorbed
$P/P_0$	relative pressure
$X_m$	monolayer capacity
$C$	constant
$S$	total surface area
$L_{av}$	Avogadro's number
$A_m$	cross sectional area
$M_v$	molar volume
$E^o$	oxidation potential
$Y$	predicted response
$\beta$	coefficient
$n$	number of factor
$X$	coded value
$\varepsilon$	random error
$T$	temperature
$r$	reaction rate
$[A]$	concentration of reactant A
$[B]$	concentration of reactant B
$k_{app}$	apparent reaction constant
$C$	concentration of organic dye
$t$	reaction time
$R^2$	determination of coefficient
$A_0$	pre-exponential factor
$E_a$	activation energy

$\text{NH}_3\text{N}$	ammoniacal nitrogen
$-\text{C}=\text{C}-$	alkene group
$-\text{C}=\text{N}-$	imine group
$-\text{C}=\text{O}$	carbonyl group
$-\text{N}=\text{N}-$	azo group
$-\text{NO}_2$	nitro group
$-\text{NO}$	nitroso group
$-\text{NH}_2$	amino group
$-\text{NR}_2$	amino group
$-\text{NHR}$	amino group
$-\text{COOH}$	carboxyl group
$-\text{SO}_3\text{H}$	sulfonate group
$-\text{OH}$	hydroxyl group
$-\text{OCH}_3$	methoxy group
$\bullet\text{OH}$	hydroxyl radical
$\text{SO}_4\bullet^-$	sulfate radical
$\text{TiO}_2$	titanium dioxide
$\text{ZnO}$	zinc oxide
$\text{Fe}_2\text{O}_3$	ferric oxide
$\text{H}_2\text{O}_2$	hydrogen peroxide
PS	persulfate
PMS	peroxymonosulfate
$\text{Zn}(\text{NO}_3)_2$	zinc nitrate
TTIP	titanium isopropoxide
$\text{FeCl}_3$	iron (III) chloride
$g\text{-C}_3\text{N}_4$	graphitic carbon nitride
$\text{CO}_3^{2-}$	carbonate ion
$\text{PO}_4^{2-}$	phosphate ion
$\text{Na}_2\text{S}_2\text{O}_8$	sodium persulfate
$\text{K}_2\text{S}_2\text{O}_8$	potassium persulfate
$\text{KHSO}_5$	potassium peroxymonosulfate
HCl	hydrochloric acid
NaOH	sodium hydroxide
$\text{K}_2\text{CO}_3$	potassium carbonate

$\text{NH}_4\text{OH}$	ammonium hydroxide
$e^-$	electron
$h^+$	hole
$\bullet\text{O}_2^-$	superoxide radicals
$\text{Fe}^{2+}$	ferrous ion
$\text{Fe}^{3+}$	ferric ion
$\text{HO}_2\bullet$	peroxyl radical
$\text{S}_2\text{O}_8^{2-}$	persulfate ion
$\text{HSO}_5^-$	peroxymonosulfate ion
$\text{S}_2\text{O}_8\bullet^-$	persulfate radical
$\text{SO}_5\bullet^-$	peroxymonosulfate radical
$\text{H}^+$	hydrogen ion
$\text{OH}^-$	hydroxide ion
DOE	Department of Environment
EQR	environmental quality report
BOD	biochemical oxygen demand
SS	suspended solid
COD	chemical oxygen demand
AOPs	advanced oxidation processes
SEM	scanning electron microscopy
EDX	energy dispersive X-ray
XRD	X-ray diffraction
FTIR	Fourier-transform infrared spectroscopy
TGA	thermogravimetric analysis
BET	Brunauer-Emmett-Teller
UV	ultraviolet irradiation
DRS	diffuse reflectance spectroscopy
CCD	central composite design
DOE	design of experiment
RSM	response surface methodology
ANOVA	analysis of variance
ATR	attenuated total reflectance
ICP-OES	inductively coupled plasma – optical emission spectroscopy

## **LIST OF APPENDICES**

APPENDIX A: Calibration Curve of Organic Dye	94
--	----

## CHAPTER 1

### INTRODUCTION

#### 1.1 Water Pollution in Malaysia

Water plays an important role in supporting human life as well as preserving the biological diversity of Earth. Unfortunately, water pollution became a global issue since a few years ago as it caused around 2 million deaths per year (Chen, et al., 2019). In this 21<sup>st</sup> century, the water pollution issue becomes more critical mainly due to the increasing population. The rapid growth in the global population gives rise to the increasing demand for various resources, which leads to the development of urban cities and industries. The discharging of wastewater into water bodies can be categorized into point source and non-point source. A point source is an identifiable pollution source at which wastewater from industry will be collected through a pipe or drain before being discharged into a water body while a non-point source of pollution consists of wastewater from a wide area and the source is not easy to be identified (EPA Victoria, 2018).

Malaysia is a developing and rapidly urbanizing country, which creates a large amount of wastes daily. Various types of wastes generated from human activities, agricultural land, industries and transportation are being disposed into water bodies, including streams, rivers and oceans. According to the Environment Quality Report (EQR) 2017 prepared by Department of Environment (DOE) Malaysia as shown in Figure 1.1, the total pollution load of biochemical oxygen demand (BOD), suspended solid (SS) and ammoniacal nitrogen ( $\text{NH}_3\text{N}$ ) in Malaysia's water sources were 545 tonnes/day, 909 tonnes/day and 190 tonnes/day, respectively. Among five types of water pollution sources, including sewage, piggery, agro-based industry, wet market and manufacturing industry, sewage is the largest contributor to total pollution load in Malaysia (DOE, 2018). Thus, municipal wastewater treatment is highly necessary for every area including rural areas and urban cities to reduce the pollution load of sewage.

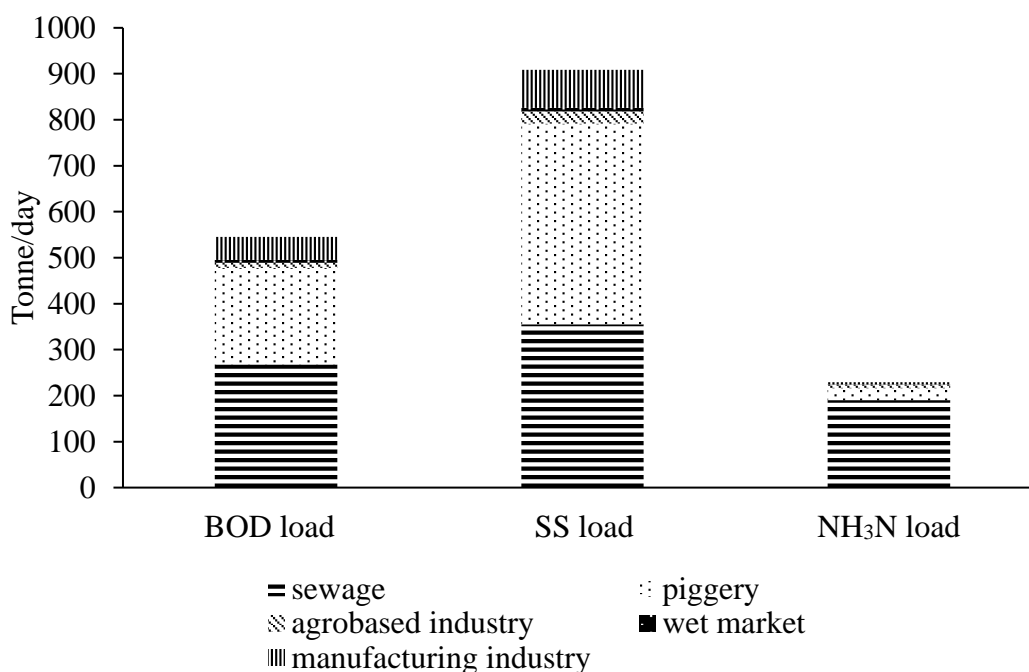


Figure 1.1: Assessment of Pollution Load by Source of Water Pollution in 2017 (DOE, 2018)

## 1.2 Background of Dyes

A dye is a substance that imparts colour to substrate through chemical bonding. The molecular structure of dye consists of a chromophore, a colour-bearing group that allows the absorption of visible light, which causes the dye to have the ability to generate a various colour. Besides, dyes consist of auxochromes, which modifies the ability of chromophore to absorb light (Lyon, 2010). The significant types of chromophore are alkene ( $-C=C-$ ), imine ( $-C=N-$ ), carbonyl ( $-C=O$ ), azo ( $-N=N-$ ), nitro ( $-NO_2$ ) and nitroso ( $-NO$ ), while some common auxochromes are amino ( $-NH_2/-NR_2/-NHR$ ), carboxyl ( $-COOH$ ), sulfonate ( $-SO_3H$ ), hydroxy ( $-OH$ ) and methoxy ( $-OCH_3$ ) (Rangabhashiyam, Anu and Selvaraju, 2013).

Dyes can be categorized into natural dyes and synthetic dyes. Natural dyes are produced naturally from sources such as trees, vegetables, plants, insects and lichens. The application of natural dyes started 4000 years ago in Egypt and various evidence shows that the ancients had attempted to extract natural dyes from various plants and flowers. However, there are only limited type of natural dyes can be used as most of the dyes extracted are unstable. Examples of natural dyes are alizalin, a red dye extracted from the madder plant

and indigo, a blue dye extracted from indigo plant (Stothers and Abrahart, 2019). Synthetic dyes are produced from the reaction of two or more chemicals. Nowadays, synthetic dyes are more preferable to be used in dyeing industries due to their low cost and more variety of colours can be obtained from synthetic dyes by reacting to different combinations of chemicals. Synthetic dyes can be classified according to their chemical structure, based on their chromophore and auxochromes groups. They can also be classified according to their applications, as presented in Table 1.1, where acid, basic, direct, disperse, sulphur and reactive dye had different principal substrates and application methods (Adegoke and Bello, 2015).

Table 1.1: Classification of Dyes Based on Application (Adegoke and Bello, 2016)

<b>Class</b>	<b>Chemical Types</b>	<b>Principal Substrates</b>	<b>Application Method</b>
Acid	Azo, azine, anthraquinone, nitro, nitroso, triphenylmethane	Leather, inks, paper, silk, wool, nylon	Neutral to acidic dye bath
Basic	Azo, azine, acridine, oxazine, cyanine, xanthene	Inks, polyester, modified nylon, paper, polyacrylonitrile	Acidic dye bath
Direct	Azo, oxazine, stilbene, phthalocyanine	Nylon, leather, paper, rayon, cotton	Neutral or slightly alkaline baths
Disperse	Azo, nitro, styryl, anthraquinone, benzodifuranone	Plastic, acrylic, polyamide, polyester	Fine aqueous dispersions applied by high temperature and pressure;
Sulphur	Indeterminate structure	Cotton, rayon	Aromatic substrate vatted with sodium sulfide
Reactive	Azo, basic, oxazine, formazan, anthraquinone, phthalocyanine	Nylon, silk, wool, cotton	Dye's reactive site reacts with fibre's functional group

Among the various industries, the textile industry utilizes the largest amount of dyes in their manufacturing process. During dyeing processes, dyes and various chemicals will be added to the textile's fibres. Part of the dyes will not be fixed to the fabric fibre due to the low level of dye-fibre fixation. The residual dyes will be washed out and cause effluents of the textile industry to contain a high concentration of unfixed dyes (Hassan and Nemr, 2017). Table 1.2 shows the fixation degree of some common dyes used in the textile industry.

Table 1.2: Fixation Degree of Dyes on Textile (Ammayappan, Jose and Raj, 2016)

<b>Dye Classes</b>	<b>Fixation Degree (%)</b>
Acid	80-95
Basic	95-100
Direct	70-95
Disperse	90-100
Sulphur	60-90
Reactive	50-90

According to Hassan and Nemr (2017), there were around 10000 types of dye used in the textile industry and 70% of them are azo dyes, which are synthetic and complex in structure. Azo dyes possess an azo bond ( $-N=N-$ ) and consists of coupling of diazotized amine with phenol or amine. Wastewater that consisting of azo dyes might cause the conversion of azo group into aromatic amines. The accumulation of aromatic amines in ecosystem possesses toxic effect on aquatic life and sometimes mutagenic effect on human (Lade, et al., 2015). Nevertheless, the dye effluents are high in pH, temperature, chemical oxygen demand (COD), BOD, SS, salts and metals (Yaseen and Scholz, 2018). The discharging of poor-treated or untreated effluences into water bodies will contaminate surface water, soil and sediment. Thus, the wastewater treatment plant is highly necessary for all industries to ensure their effluents are well treated and their harmful contents are reduced to the standard concentration before discharged into any receiving water source.

### **1.3 Dye Removal Method**

Wastewater treatment is a major challenge for industries involving dye operation as most of the dyes are water soluble and able to change the appearance of water with its acidic properties. Dyes are highly toxic and sometimes carcinogenic to aquatic life and mammalian animals. Due to its environmental impact and health concern, various separation techniques have been used to remove dyes from industrial effluents (Kandisa, et al., 2016). The technologies for dye removal can be classified into biological, physical and chemical removal methods.

#### **1.3.1 Biological Removal Method**

Biodegradation methods have been widely used in the treatment process of industrial effluents as many microorganisms including bacteria, fungi and algae have the ability to accumulate and degrade various pollutants (Sivarajasekar and Baskar, 2015). Biological treatment is a cost-effective and eco-friendly dyes removal technique. Its advantages over physical and chemical treatment including low operating costs, low production of sludges and low emission of toxic substances (Rajeswari, Subashkumar and Vijayaraman, 2011). However, biodegradation methods possess some disadvantages. For instance, it required a large land area for operation. Besides, microbial activities are uncertain due to their disruption by chemical toxicity and diurnal variations (Sivarajasekar and Baskar, 2015).

Biological removal of dyes is generally classified into two categories, aerobic treatment and anaerobic treatment. In the past few years, many bacteria and fungi strains had been reported to have the ability in decolorizing azo dyes aerobically, and most of them are within the class of white-root fungi. The utilization of aerobic microorganisms in dye degradation is a cost-effective process and the removal of dyes can be performed without the generation of by-product. However, complete degradation of dye using these microorganisms required an extremely large reactor size due to their long growth phase and long holding time (D'Anthony, Iraca and Romero, 2017). Unlike aerobic degradation which utilizes oxygen for dye removal, anaerobic degradation method decolorizes water-soluble dyes and azo dyes using reduction reaction in the presence of hydrogen. Anaerobic bacteria is able to perform dye degradation via

reduction of azo group. Azo groups are converted into toxic and mutagenic aromatic amines under anaerobic conditions. Since the aromatic amines produced will not further be degraded automatically, a second stage treatment is required for the detoxification of aromatic amines (D'Anthony, Iraca and Romero, 2017).

### **1.3.2 Physical Removal Method**

Physical removal of dye from water sources is a separative method and not a degradative method. This is because physical removal methods just simply separate dyes from water or merely change the phase of dye, commonly from liquid phase to solid phase, without converting dyes to other harmless products. Dyes being separated from water sources are still in existence and usually required additional treatment to degrade them. The common physical methods being widely used in industries for dye removal are membrane process and adsorption.

Various membrane processes have been developed for water treatment and all of them perform removal of pollutants using similar separation mechanisms. Membrane processes such as microfiltration, ultrafiltration and nanofiltration can retain suspended solids larger than their membrane's pore size while reverse osmosis, as pressure driven technique, can be used to remove dissolved solids (Nqombolo, et al., 2017). Organic pollutants including dyes, after being separated from water through membrane filtration will form sludge. The sludge produced required additional treatment such as microbial treatment or chemical treatment to remove their hazardous contents before being disposed off. Another disadvantage of membrane process is the frequent occurrence of membrane fouling which leads to low membrane performance and indirectly causes ineffective water treatment (Nqombolo, et al., 2017).

Adsorption is one of the most promising and most frequently used water treatment techniques for the removal of organic pollutants such as dyes from industrial effluents. Adsorption performs equilibrium separation by attracting certain components from the fluid phase to an adsorbent. By utilizing surface forces through intermolecular force of attraction, the targeted solutes will be concentrated on the adsorbent surface when they contact each other (Kandisa, et al., 2016). Adsorption is a selective process as the separation quality is

affected by various physio-chemical factors such as pore size and polarity of adsorbent, molecular size, polarity and molecular mass of adsorbed materials. The removal of dyes from water can be achieved through the attachment of dyes onto the adsorbent surface via chemical or physical bond (Foo and Hameed, 2010).

### **1.3.3 Chemical Removal Method**

Chemical methods involve the addition of chemicals into effluents during the treatment process for the removal of dyes and other contaminants. These chemical techniques are efficient in removing dyes. However, environmental problems could be created due to the generation of sludge and the production of by-products. The common dye chemical removal methods include coagulation process and chemical oxidation process. Recently, a newly emerged technology, known as advanced oxidation processes (AOPs) have been applied in the water treatment process and reported to have success in degrading organic dyes effectively (Sivarajasekar and Baskar, 2015).

Chemical coagulation method is one of the most practised technologies in water decolourization. This process involves the addition of chemicals into wastewater to alter the physical state of suspended and dissolved solid. Coagulants added into water will accumulate certain contaminants and uniform mixing provided during the flocculation process allow them to form large flocs. The removal of contaminants is then achieved by sedimentation of the large flocs formed. The mechanism for dyes removal using coagulant is still not absolutely clear but it is being widely used in some developing countries. This method had been used to treat dye-containing wastewater for many years due to its low capital cost and low operating cost. However, the disadvantages of coagulation method include the ineffective removal of soluble dyes and the generation of a large amount of sludge (Verma, Dash and Bhunia, 2012).

Dyes degradation can also be achieved by the oxidation process using various oxidants. Generally, the oxidation process can convert organic compounds into carbon dioxide, water and a less hazardous inorganic compound. There are various oxidizing agents being used in degrading dyes and the most commonly used oxidizing agents are oxygen, ozone, halogen,

hydrogen peroxide and hydroxyl radicals. The utilization of hydroxyl radicals for oxidative removal of dyes is known as AOPs.

#### **1.4 Problem Statement**

Biomass existed abundantly in developing countries, especially areas with agriculture as their major economic activity (Tsamo, et al., 2019). In 2009, agricultural wastes in Malaysia were reported at around 0.122 kg/capita/day and estimated to reach 0.21 kg/capita/day by 2025 (Agamuthu, et al., 2009). Some of these agricultural wastes are potential biomass sources, such as empty fruit bunch, coconut shell, rice husk and sugarcane bagasse. Thus, effective measures have to be taken to manage this biomass in a useful and effective manner. One of the common options is the conversion of biomass to biochar via pyrolysis (Hariz, et al., 2015).

The application of biomass as an adsorbent in the wastewater treatment process arises worldwide, but it possesses limitations such as poor porosity, low specific surface area and poor cation exchange capacity. These poor adsorption capabilities can be improved by converting biomass to biochar (Tsamo, et al., 2019). Furthermore, various biochar modifications had been carried out to enhance mechanical properties as well as improve the specific surface area and porosity of biochar. For instance, biochar composites were prepared by impregnating biochar in minerals or chemicals such as metal salts (Premarathna, et al., 2019). Some of the biochar composites were found to have high potential in promoting the photocatalytic degradation of organic dyes.

Currently, some of the countries are facing water shortage as most of their water sources including rivers, streams and oceans are critically polluted and contain hazardous contaminants that exceed standard concentration. Dyes are one of the contaminants that should be concerned as they are extremely visible and affect light penetration which indirectly disrupts the aquatic ecosystem. Other than the visual appearances, most of the dyes are toxic and carcinogenic due to various types of chromophores (Yaseen and Scholz, 2018). There were some conventional dye removal methods being applied in wastewater treatment processes such as adsorption, membrane filtration and microbial action but all possess several limitations. In addition, none of these methods can provide acceptable COD reduction and decolourization.

Advanced oxidation processes (AOPs) were proposed as a great substitute to the conventional dye degradation methods as the hydroxyl ( $\bullet\text{OH}$ ) and sulfate radicals ( $\text{SO}_4\bullet^-$ ) produced during AOPs are highly reactive and have the ability to oxidize most of the organic compound including organic dyes to harmless products such as carbon dioxide and water (Nemr, Hassaan and Madkour, 2018). During AOPs, visible light or ultraviolet irradiation is usually used as an activator to activate photocatalysts such as titanium dioxide ( $\text{TiO}_2$ ) zinc oxide ( $\text{ZnO}$ ), ferric oxide ( $\text{Fe}_2\text{O}_3$ ) and graphitic carbon nitride ( $\text{g-C}_3\text{N}_4$ ) as well as oxidants such as hydrogen peroxide ( $\text{H}_2\text{O}_2$ ), persulfate (PS) and peroxymonosulfate (PMS) for the production of  $\bullet\text{OH}$  and  $\text{SO}_4\bullet^-$ .

### **1.5 Aim and Objectives**

The aim of this study is to compare the photocatalytic degradation of organic dye in the presence of biochar composites using various oxidants. This study consists of several sub-objectives, including:

- i. To synthesize and characterize pure biochar and biochar composites.
- ii. To study the process behaviour for photocatalytic degradation of organic dye under different operating conditions.
- iii. To study the reaction kinetic for photocatalytic degradation of organic dye.

### **1.6 Scopes of the Study**

The scopes of this study included the preparation and characterization of biochar composites. Biochar was first prepared by pyrolyzing coconut shells at  $500\text{ }^\circ\text{C}$ . The biochar obtained was then impregnated in chemicals including zinc nitrate ( $\text{Zn}(\text{NO}_3)_2$ ), titanium isopropoxide (TTIP), iron (III) chloride ( $\text{FeCl}_3$ ) and melamine to obtain biochar composites which are  $\text{ZnO}/\text{biochar}$ ,  $\text{TiO}_2/\text{biochar}$ ,  $\text{Fe}_2\text{O}_3/\text{biochar}$  and  $\text{g-C}_3\text{N}_4/\text{biochar}$ , respectively. After that, the synthesized catalysts were characterized by scanning electron microscopy with energy dispersive X-ray (SEM-EDX), X-ray diffraction (XRD), Fourier-transform infrared spectroscopy (FTIR), thermogravimetric analysis (TGA), surface area analysis, zeta potential analysis and UV-Vis diffuse reflectance spectroscopy (DRS).

The photocatalytic degradation of organic dye was studied using different types of biochar composites and different types of oxidants, including H<sub>2</sub>O<sub>2</sub>, PS and PMS. The degradation of organic dye was examined using UV-Vis spectrophotometer. After that, various parameter studies were carried out and the optimum operating condition was determined by using Response Surface Methodology (RSM). Kinetic study and COD analysis were also conducted under different operating condition.

## CHAPTER 2

### LITERATURE REVIEW

#### 2.1 Biochar

Biochar is a carbonaceous material, which is obtained from the thermochemical decomposition of biomass under an oxygen-limited environment (Cheng and Li, 2018). Biochar can be derived from various biowaste materials such as crop residues (wood, weed straw and rice husk), industrial wastes (empty fruit bunch and sawdust) and food wastes (orange peel, sugarcane bagasse and coconut shell). The major element of biochar is carbon and the remaining elements including oxygen, hydrogen, ash and trace amounts of inorganics such as sulphur and nitrogen. Biochar's elemental compositions are varied according to their production method and source of biomass (Cha, et al., 2016). Table 2.1 shows the composition of some raw biomass.

Conversion of biomass through pyrolysis, hydrothermal carbonization or gasification brings the production of carbon-rich biochar. The most commonly used method is pyrolysis, which is a process that thermally decompose organic materials under temperature range of 300-900 °C in an oxygen-limited condition. During pyrolysis process, cellulose, hemicellulose and lignin of biomass undergo reactions such as fragmentation, cross-linking and depolymerization to produce gaseous (syngas), liquid (bio-oil) and solid product (biochar) (Cha, et al., 2016). The proportion of biomass converted into biochar is affected by the pyrolysis temperature and the lignin content in raw materials. Generally, different biomass has maximum biochar yield at different temperature, by which lower temperature causes incomplete conversion of biomass and higher temperature favours the production of syngas. Besides, reviews suggested that higher lignin content in biomass results in higher yield of biochar, as lignin consists of largest amount of carbon (58.6 %), compared to cellulose (41.8 %) and hemicellulose structure (38.1 %) (Cagnon, et al., 2009).

Table 2.1: Elemental Composition of Raw Biomass (Cagnon, et al., 2009)

<b>Biomass</b>	<b>Hemicellulose (%)</b>	<b>Cellulose (%)</b>	<b>Lignin (%)</b>	<b>C (%)</b>	<b>H (%)</b>	<b>O (%)</b>	<b>Ash (%)</b>	<b>N (%)</b>	<b>S (%)</b>
Coconut shells	32	14	46	48.7	5.8	42.5	4.9	< 0.3	< 0.3
Apple pulp	16	16	21	41.6	6.2	47.2	0.9	< 0.3	< 0.3
Plum pulp	14.5	6.5	39	48.1	6.5	41.8	4.3	2.1	< 0.3
Plum stones	20	23	49	50.7	6.3	41.1	0.9	0.9	< 0.3
Olive stones	15	14	42	46	5.9	42.3	4.4	1.0	< 0.3
Acid olive stones	20	29	42	48.3	6.1	43.1	0.4	< 0.3	< 0.3
Soft wood	18.5	36	30.5	46.1	6.0	45.5	0.3	< 0.3	< 0.3

Biochar consists of various pore structures, functional groups and specific surface area. Besides, it has the capability of surface modification, which makes it a potential adsorbent that can be used for the removal of organic pollutants. Unlike the costly commercial activated carbon, biochar is a cost-effective and environmentally friendly adsorbent, which can adsorb heavy metals and organic materials from contaminated water. The adsorption efficiency of biochar depends on the raw biomass material used for the production of biochar. According to Cha, et al. (2016), the adsorption capability of biochar is affected by the amounts of mineral components ( $\text{CO}_3^{2-}$  and  $\text{PO}_4^{2-}$ ) contained in biochar. Besides, different types of biochar used perform the best adsorption removal rate at different pyrolysis temperature and solution pH. Apart from adsorption, biochar can also facilitate other important activities, such as catalysis, water filtration, soil amendment and carbon sequestration.

### **2.1.1 Biochar vs Activated Carbon**

The differences between biochar and activated carbon is one of the controversial topics between researchers and industries, as their applications increasingly overlap. Traditionally, activated carbon was widely used for adsorption activities, such as heavy metals removal and organic pollutants degradation. This is mainly due to its plentiful micropores and large surface areas, which lead to its outstanding sorption capacities (Hao, et al., 2018). Recently, biowaste-derived biochar has receiving much attentions and started to be used in water treatment process as an alternative of activated carbon, due to its eco-friendly and wide feedstock sources, cost-effectiveness feature and vast surface functionalities.

The term “activated carbon” is used to defined a carbon-rich material, which had been activated using a set of processing technique to increase its microporosity before carbonization process. The activation processes increase adsorption capability of carbonaceous material by removing carbon atoms from them to create nooks and crannies, which are the adsorption sites (McLaughlin, 2016). The carbonaceous sources of activated carbon include coal, lignite, petroleum pitch and biomass such as wood and bamboo. It can be seen that some of the activated carbons share the same feedstock source with biochar. However, they can be easily differentiated as biochar is an inactivated carbon by which

the biomass sources need not undergo any activation treatment prior to pyrolysis process.

In the aspect of property differences, activated carbon has higher mechanical hardness and bulk density than biochar. Besides, biochar is a less effective adsorbent as it possesses lower pore volume and specific surface area than activated carbon. Generally, activated carbon has the specific surface area ranging from 500 to more than 1500 m<sup>2</sup>/g while biochar has the specific surface area of less than 300 m<sup>2</sup>/g. However, biochar is more suitable to be used for the removal of large organic contaminants as it consists of plentiful macropores, as compared to activated carbon, which consist of extremely small micropores that are easily blocked by large organic contaminants (Hao, et al., 2018). In addition, biochar exhibits ion exchange capacity, which is generally does not owned by activated carbon. This ion exchange property is owing to the exists of carboxylic acid functionalities at biochar graphitic backbone. Activated carbon does not possess this feature as all of its side chain aliphatic groups had been removed during activation process (McLaughlin, 2016).

### **2.1.2 Activation of Biochar**

Adsorption is one of the essential steps in heterogeneous catalysis as the general catalysis mechanism involves adsorption of reactant onto catalyst active sites, reaction between reactants and desorption of products from catalyst surface. Thus, biochar has the potential to be used as heterogeneous catalyst due to its adsorption ability. Generally, the performance of a catalyst is affected by the quantity of active sites on catalyst surface and the accessibility to these active sites. Thus, specific surface area and porosity of catalyst are two major properties to determine the effectiveness of a heterogeneous catalyst (Cheng and Li, 2018). In this situation, the catalytic application of pure biochar is considerably narrow as it consists of poor porosity and low specific surface area. Thus, a variety of modification approaches had been developed to functionalize biochar or endue it with certain properties.

To enhance biochar adsorption and catalytic properties, biochar can be physically activated through its exposure to steam or carbon dioxide under high temperature. The steam activation process increases surface area of biochar through the removal of syngas, which composed of mainly hydrogen gas.

Meanwhile, it increases porosity of biochar through the removal of volatile gases (Rajapaksha, et al., 2016). For the activation process using carbon dioxide, the carbon dioxide supplied reacts with carbon of the biochar to produce carbon monoxide. The loss of carbon atoms from biochar increases porosity of biochar, contributes to the formation of microporous structure (Rajapaksha, et al., 2016).

Moreover, the creation of porous structure can be achieved at relatively lower temperature through chemical activation. To carry out chemical activation, biomass precursors will be pre-treated by activators before proceeding to routine pyrolysis process. The common activators used in this process include potassium hydroxide, zinc chloride, phosphoric acid and potassium carbonate (Cheng and Li, 2018). Besides, since biochar consists of surface functional groups that can promote the adsorption of metal precursors, biochar composites with enhanced catalytic performance can be synthesised by subjecting biochar to specific metal salts.

## **2.2 Metal Oxide and Non-Metal Based Photocatalyst**

Photocatalyst is a material which has the ability to absorb light and produce electron-hole pairs that enable reaction between the participating reactants. Generally, a good photocatalyst possesses high surface area, appropriate surface morphology, high stability and reusability (Khan, Adil and Al-Mayouf, 2015). Metal oxide based photocatalyst such as  $\text{TiO}_2$  and  $\text{ZnO}$  had proved their efficiency in water treatment process through degradation of organic pollutants.

$\text{TiO}_2$  was widely studied in the field of photocatalysis due to its eco-friendliness, low cost and high photo-activity. However, the photocatalytic application of  $\text{TiO}_2$  is limited by its large band gap energy of 3.2 eV. This feature restricts its ability to absorb visible light and only ultraviolet irradiation can be utilized for the excitation process. In this situation, additional ultraviolet source has to be equipped in the photocatalytic system as ultraviolet light account only 7% of sunlight, which is insufficient to excite the  $\text{TiO}_2$  photocatalyst (Lu, et al., 2019). Therefore, modified  $\text{TiO}_2$  had been studied extensively to overcome the limitation and to improve the photocatalytic activity of  $\text{TiO}_2$ .

$\text{ZnO}$  is an emerging photocatalyst due to its strong oxidation ability, high charge carrier mobility and toxicity free feature. Similar to  $\text{TiO}_2$ , large band gap energy possessed by  $\text{ZnO}$  of 3.3 eV limits its ability to be excited by visible light

irradiation (Das, Nikhil and Nair, 2019). On the other hand,  $\text{Fe}_2\text{O}_3$  is a common catalyst generally being used in heterogeneous Fenton reaction. It possesses narrower band gap energy of 2.2 eV, which enables it to be excited by visible light irradiation (Mallick and Dash, 2013). The incorporation of light irradiation in Fenton reaction is known as photo-Fenton process. As light source is used in photo-Fenton process, the formation of  $\bullet\text{OH}$  can be enhanced and the rate of oxidative degradation of organic pollutants can be increased (Desipio, et al., 2019).

Recently  $\text{g-C}_3\text{N}_4$ , which is an organic semiconductor, was reported as a metal-free photocatalyst that can be excited by visible light irradiation as it possesses narrow band gap energy of 2.7 eV (Li, et al., 2019). It can be prepared from the polymerization of urea, melamine, cyanamide, dicyanamide or thiourea (Jeon, Lee and Baek, 2017). Its advantages over the common metal oxide catalysts are the high stability, cheap availability and visible light responsiveness. However, the photocatalytic capability of  $\text{g-C}_3\text{N}_4$  is limited by its poor utilization efficiency of visible light and low specific surface area (Li, et al., 2019).

### **2.3 Biochar Composites**

According to literatures, various types of metal oxide-biochar composites or known as biochar-based metal oxide catalyst had been studied and developed. These including  $\text{ZnO/biochar}$ ,  $\text{TiO}_2/\text{biochar}$  and  $\text{Fe}_2\text{O}_3/\text{biochar}$  composite. These composites not only possess better catalytic performance than pure biochar, but also having superior catalytic properties if compared to their metal oxide alone.

Gholami, et al. (2019) had studied the sonocatalytic activity of  $\text{ZnO/biochar}$  in the degradation of Gemifloxacin. According to their study, the surface area and pore volume of biochar increased around 75 % and 100 %, respectively after treating it with zinc nitrate to produce  $\text{ZnO/biochar}$  composite. Besides, the study of photocatalytic degradation of sulfamethoxazole using  $\text{TiO}_2/\text{biochar}$  had been carried out by Kim and Kan (2016). This study showed that better COD removal can be achieved when  $\text{TiO}_2/\text{biochar}$  is used as photocatalyst instead of the conventional pure  $\text{TiO}_2$ . Furthermore, Chaukura, Murimba and Gwenzi (2015) had examined the adsorption capacity of

Fe<sub>2</sub>O<sub>3</sub>/biochar in the removal of Methyl Orange dye. According to the results obtained from various parameter studies, Fe<sub>2</sub>O<sub>3</sub>/biochar could consistently performed greater dye adsorption than pure biochar, which can be concluded that adsorption mechanism by biochar was enhanced by the existence of Fe<sub>2</sub>O<sub>3</sub>.

Apart from metal oxide composites, recently g-C<sub>3</sub>N<sub>4</sub>/biochar was proposed to have both superior photocatalytic and adsorptive capabilities in removing organic pollutants. Photocatalytic capacities of g-C<sub>3</sub>N<sub>4</sub> can be improved by modifying it with biochar to form a composite material. This composite material possesses greater catalytic properties than both pure g-C<sub>3</sub>N<sub>4</sub> and pure biochar. The carbonaceous biochar acts as a cocatalyst in the composite to provide sufficient catalyst active sites available for degradation of organic pollutants. Concurrently, g-C<sub>3</sub>N<sub>4</sub> also acts as a modifier for biochar by which the biochar is endowed with light-responsive self-generation capability (Pi, et al., 2015).

## **2.4 Characterization of Catalyst**

Characterization of solid catalyst is necessary for better understanding on the catalyst being synthesized and studied. The catalysts could be characterized using several technologies, including SEM-EDX, XRD, FTIR, TGA and surface area analysis.

### **2.4.1 Scanning Electron Microscopy with Energy Dispersive X-Ray (SEM-EDX)**

SEM-EDX is an imaging technique that utilizes a focused beam of highly energetic electrons to image specimens and gain information of its structure and composition. Electron microscope was developed due to the limitations of optical microscope in providing sufficient resolution and magnification. This is mainly because conventional optical microscope uses visible light with limited wavelength to create magnified image. The basic principle of SEM-EDX is the generation of secondary electrons, backscattered electrons and characteristic X-rays when the beam of electrons hit the sample surface and interact with its atoms (Joshi and Bhattacharyya, 2008). The specimen interactions of SEM-EDX are shown in Figure 2.1.

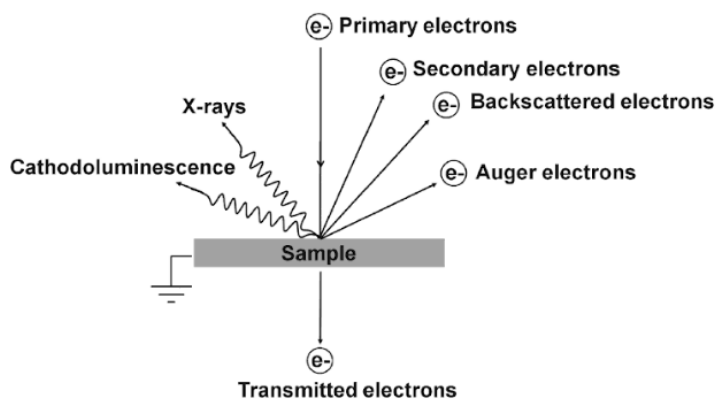


Figure 2.1: Specimen Interaction of SEM-EDX (Challa, 2009)

Backscattered electrons are incident electrons that scattered  $180^\circ$  from normal, as a result of collisions between incident electrons and specimen atoms that happen nearly normal to the incident path. These electrons can be used to determine the atomic number of the specimen. In the meantime, ionization of electrons in specimen atom occur when incident electron passes near the specimen atoms and impart some of its energy to these electrons. These ionized electrons are known as secondary electrons, which leaves the atom of specimen with small energy of around 5 eV. These secondary electrons can provide topographic information of samples (Challa, 2009). The leaving of electrons from specimen atom results in the existence of vacancies at the atom inner shell. Electrons from higher energy shell will then fall to this lower energy shell to fill up the particular vacancies. This movement of higher energy electrons causes emission of energy in the form of X-ray, as illustrated in Figure 2.2. The X-ray released possesses a characteristic energy which is unique for every element, thus act as a fingerprint of specimen (Nanakoudis, 2018).

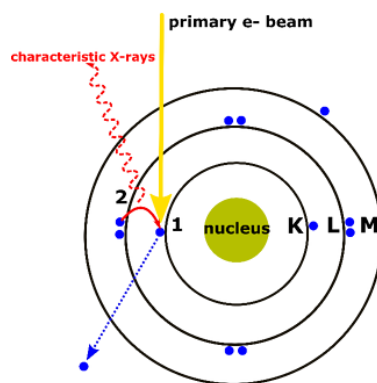


Figure 2.2: X-ray Generation Process (Nanakoudis, 2018)

In the research carried out by Khataee, et al. (2017), SEM-EDX was used to examine the surface morphology of biochar and TiO<sub>2</sub>-biochar composite. According to the SEM images shown in Figure 2.3, pure biochar possessed smooth and bulky morphology while TiO<sub>2</sub>/biochar composite consisted of fine spherical nanostructures. It is clear that TiO<sub>2</sub> nanoparticles were managed to be synthesized and immobilized on biochar surface. In addition, Figure 2.4 shows the EDX spectrum of TiO<sub>2</sub>/biochar. The strong peak of titanium observed indicated that biochar was modified by TiO<sub>2</sub>.

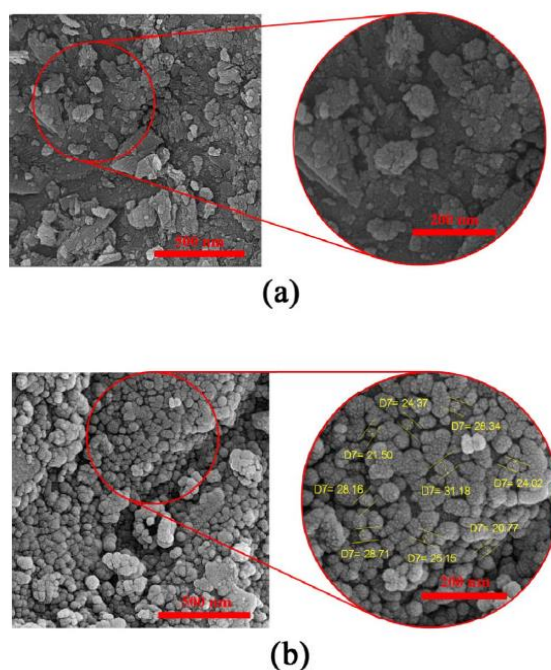


Figure 2.3: SEM Image of (a) Biochar (b) TiO<sub>2</sub>/biochar (Khataee, et al., 2017)

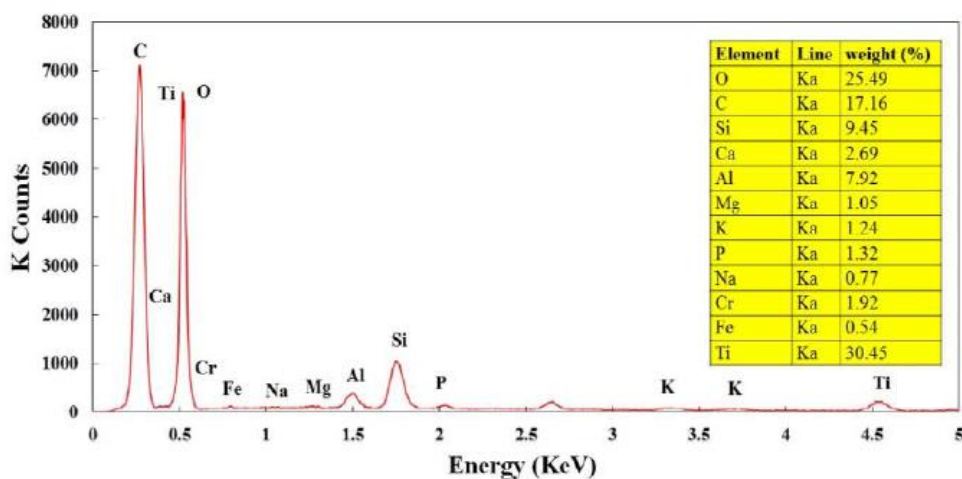


Figure 2.4: EDX Spectrum of TiO<sub>2</sub>/biochar (Khataee, et al., 2017)

### 2.4.2 X-Ray Diffraction (XRD)

XRD is an analytical technique used to characterize crystallographic structure, crystallite size and atomic spacing of solid samples. During analysis, X-rays generated by cathode ray tube will be first filtered for the production of monochromatic radiations. These radiations are then focused and directed towards the sample. When Bragg's Law stated in Equation (2.1) is satisfied, X-rays scattered by atoms are in phase and diffraction occurs at angle,  $\theta$ . The X-ray diffractions are detected from all possible direction by scanning specimen through a range of  $2\theta$  angles (Dutrow and Clark, 2019).

$$\eta\lambda = 2d \sin \theta \quad (2.1)$$

Where,

$\eta$  = integer called the order of reflection

$\lambda$  = wavelength of X-ray

$d$  = distance between two lattice planes

$\theta$  = angle between incoming X-ray and normal to the reflecting plane

In addition, the crystallite size of material can be calculated by using Scherrer's formula as shown is Equation (2.2) (Dutrow and Clark, 2019).

$$\langle L \rangle = \frac{K\lambda}{B \cos \theta} \quad (2.2)$$

Where,

$L$  = crystallite size

$K$  = shape factor often taken as 0.9

$\lambda$  = wavelength of X-ray

$B$  = peak width

$\theta$  = angle between incoming X-ray and normal to the reflecting plane

In the study of sonocatalytic activity of ZnO/biochar, Gholami, et al. (2019) characterized biochar, ZnO and ZnO/biochar using XRD. According to the XRD results shown in Figure 2.5, ZnO was immobilized on biochar surface as all detected peaks of ZnO/biochar can be matched with the detected peaks of ZnO and biochar. Besides, by applying Equation (2.2), particle size of ZnO/biochar was calculated to be around 27 nm at the strongest peak with  $2\theta$  of  $36.25^\circ$ .

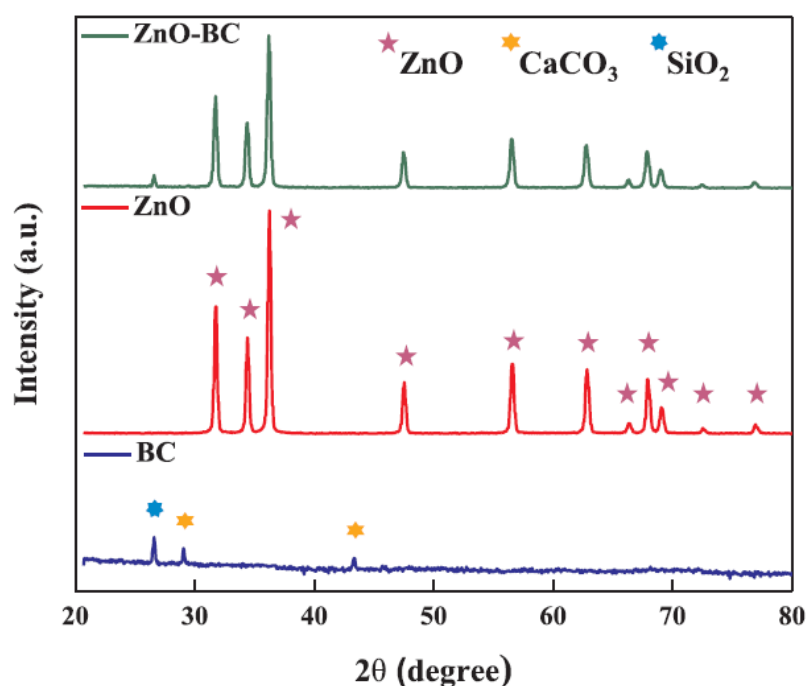


Figure 2.5: XRD Patterns of ZnO/biochar, ZnO and Biochar (Gholami, et al., 2019)

### 2.4.3 Fourier-Transform Infrared Spectroscopy (FTIR)

FTIR is a type of non-destructive vibrational technique used in material characterization, which works by obtaining infrared spectrum of absorption and emission of solid, liquid and gaseous sample. FTIR utilizes incandescent source of light to emit infrared radiation. During the analysis, infrared radiation of around  $100$  to  $10000\text{ cm}^{-1}$  is passed through a specimen by which some radiation is absorbed by functional groups of the compound and some radiation is transmitted through the organic compound. Recognition of functional groups can be done by interpreting the locations and intensities of infrared radiation

absorption as every functional group produces bond absorption at different intensity and location, as presented in Table 2.2 (Winter, 2016).

Table 2.2: Infrared Radiation Absorption of Common Functional Groups (Winter, 2016)

Function Group	Absorption Location (cm <sup>-1</sup> )	Absorption Intensity
Alkane (C-H)	2850 – 2975	Medium to strong
Alcohol (O-H)	3400 – 3700	Strong, broad
Alkene (C=C)	1640 – 1680	Weak to medium
(C=C-H)	3020 – 3100	Medium
Alkyne (C≡C)	2100 – 2250	Medium
(C≡C-H)	3300	Strong
Nitrile (C≡N)	2200 – 2250	Medium
Aromatic	1650 – 2000	Weak
Amine (N-H)	3300 – 3350	Medium
Aldehyde (CHO)	1720 – 1740	Strong
Ketone (RCOR)	1715	Strong
Ester (RCOOR)	1735 – 1750	Strong
Acid (RCOOH)	1700 – 1725	Strong

Chaukura, Murimba and Gwenzi (2015) carried out a study to characterize Fe<sub>2</sub>O<sub>3</sub>/biochar derived from pulp and paper sludge. According to the FTIR results shown in Figure 2.6, both adsorbent samples consisted of peak in the region within 3300-3400 cm<sup>-1</sup>, which indicated the presence of hydroxyl functional group. Besides, the peak possessed by biochar and Fe<sub>2</sub>O<sub>3</sub>/biochar in the region of 1590 cm<sup>-1</sup> indicated the presence of aromatic ring. Additionally, the peak of Fe<sub>2</sub>O<sub>3</sub>/biochar at around 560 cm<sup>-1</sup> indicated the existence of Fe-O bond.

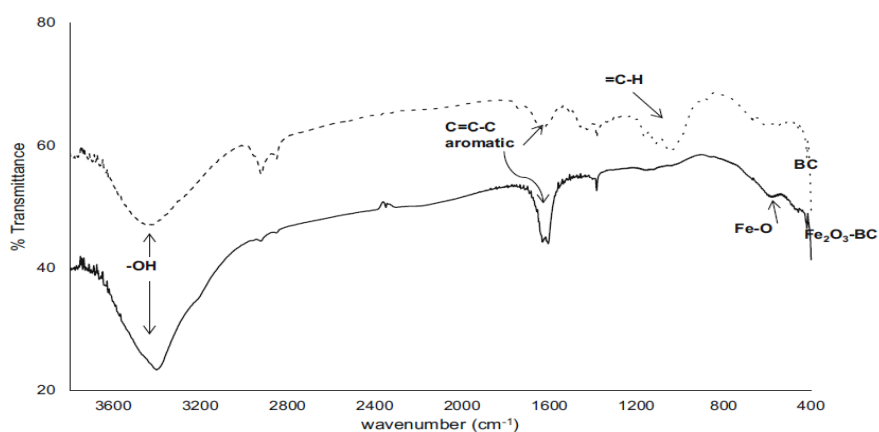


Figure 2.6: Spectra for Biochar and  $\text{Fe}_2\text{O}_3/\text{Biochar}$  (Chaukura, Murimba and Gwenzim 2015)

#### 2.4.4 Thermogravimetric Analysis (TGA)

TGA is usually carried out to investigate the thermal properties of organic compound. It analyses sample by measuring the mass change of substance as a function of temperature or time. The result of TGA is a plot of mass change versus temperature or time, as illustrated in Figure 2.7. According to Figure 2.7,  $T_i$  indicates the starting of decomposition stage by which the sample started to decompose as the influence of increasing temperature. On the other hand,  $T_f$  indicates the completion of process by which the sample stop decomposing and the remaining mass represents the amount of ashes and thermally stable residues. The mass reduction happen within  $T_i$  to  $T_f$  was varied for different substances and these changes in mass were due to various thermal events such as vaporization, oxidation, reduction, absorption and desorption (Guwahati, 2016). Sometimes, there exist one more decomposition stage before  $T_i$ , which represents mass reduction due to water loss.

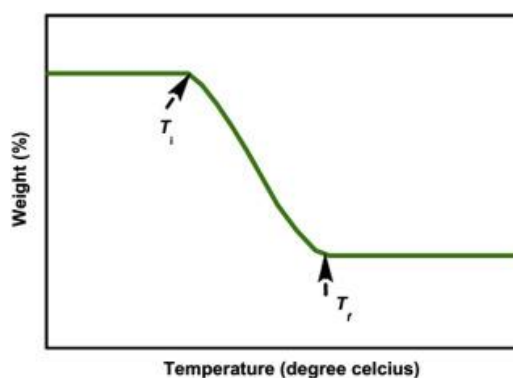


Figure 2.7: Plot of Mass Change Against Temperature (Guwahati, 2016)

Sun, et al. (2019) had studied on the removal of contaminants using Fe/biochar nanocomposite. In this study, thermal stability of pure biochar and Fe/biochar composite were evaluated using TGA. According to the TGA results illustrated in Figure 2.8, the decomposition stage of biochar was from 600 °C to 650 °C while for Fe/biochar nanocomposite was around 750 °C to 950 °C. This result proved that thermal stability of biochar was enhanced upon its impregnation in iron solution. Besides, the higher total mass loss occurred in composites was corresponded to the reduction of iron oxides to Fe<sup>0</sup>.

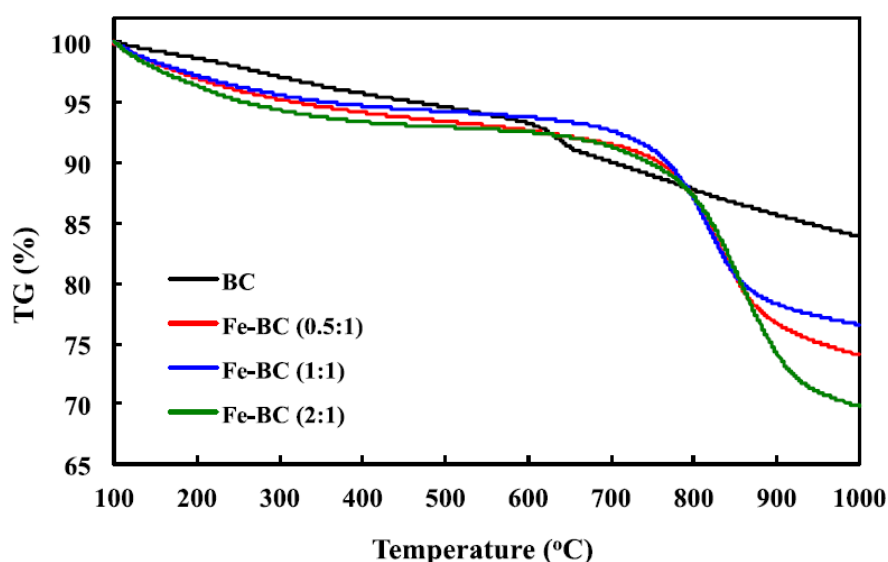


Figure 2.8: TGA Analysis of Biochar and Iron-modified Biochar (Sun, et al., 2019)

#### 2.4.5 Surface Area Analysis

Surface area analysis using BET method provides specific surface area evaluation of catalyst by nitrogen adsorption, which measured as a function of relative pressure. Nitrogen is commonly used due to its strong interaction with most solids and its availability in high purity. After the saturation pressure, no more nitrogen adsorption could occur regardless of any further increase in pressure. The sample will be removed from the nitrogen atmosphere and heated to release the adsorbed nitrogen in order to be quantified (Raja and Barron, 2012). The data collected will be displayed in the form of BET isotherm and surface area of the sample could be calculated using Equations (2.3) and (2.4).

$$\frac{1}{X[(P_0/P)-1]} = \frac{1}{X_m C} + \frac{C-1}{X_m C} \left( \frac{P}{P_0} \right) \quad (2.3)$$

$$S = \frac{X_m L_{av} A_m}{M_v} \quad (2.4)$$

Where,

$X$  = weight of nitrogen adsorbed

$P/P_0$  = relative pressure

$X_m$  = monolayer capacity

$C$  = constant

$S$  = total surface area

$L_{av}$  = Avogadro's number

$A_m$  = cross sectional area (0.162 nm<sup>2</sup> for nitrogen)

$M_v$  = molar volume (22414 mL)

## 2.5 Advanced Oxidation Processes (AOPs)

AOPs is a technique that convert organic substances into carbon dioxide, water and inorganic compounds through generation of  $\bullet\text{OH}$  and  $\text{SO}_4\bullet^-$ . It was proposed as an effective water treatment technique in 1980s due to the generation of radicals with strong oxidative power. As strong oxidizing agents, these radicals can provide sufficient destruction of organic contaminants in wastewater, and transform them into non-toxic products (Deng and Zhao, 2015). AOPs can be further categorized according to their radical generation methods. The common AOPs used in industries are photolysis, photocatalysis, Fenton process, ozonation and sonolysis.

$\bullet\text{OH}$  is one of the strongest oxidant, with an oxidation potential of around 2.8 V at 25 °C, as shown in Table 2.3. During late 19<sup>th</sup> century, other strong oxidants such as fluoride, ozone and chloride were widely used in oxidative removal of organic waste, but soon be eliminated as they are not environmentally friendly (Gosh, 2018).  $\bullet\text{OH}$  are secondary oxidants. They are produced from the combination of primary oxidants (such as hydrogen peroxide and ozone) with irradiation (ultraviolet light, ultrasound or visible light), catalyst (such as  $\text{Fe}^{2+}$ ) or photocatalyst (such as  $\text{TiO}_2$ ). Once  $\bullet\text{OH}$  are produced, they will react unselectively and rapidly with organic substances with the rate constant of around  $10^8 - 10^{10} \text{ M}^{-1}\text{s}^{-1}$  (Deng and Zhao, 2015). For hydroxyl

radicals-based AOPs, degradation of organic substances can be achieved through various reaction pathways, including hydrogen abstraction, electron transfer, radical addition and radical combination (Deng and Zhao, 2015). These reactions between  $\bullet\text{OH}$  and organic compounds generate  $\text{R}\bullet$  or  $\text{R}\bullet\text{OH}$ , which are carbon-centered radicals. These biodegradable intermediates will further react with oxidants, leading to mineralisation process, where carbon dioxide, water and inorganic salts are produced (Mazille and Spuhler, 2019).

Table 2.3: Oxidation Potential of Common Oxidants (Rodriguez, et al., 2008)

Oxidant	Oxidation Potential, $E^\bullet$ (V, 25°C)
Fluoride	3.06
Hydroxyl radical	2.80
Atomic oxygen	2.42
Ozone	2.07
Hydrogen peroxide	1.78
Permanganate	1.68
Chlorine dioxide	1.57
Hypochlorous acid	1.49
Chlorine	1.36
Oxygen	1.23

Sulfate radicals based AOPs involve generation of  $\text{SO}_4^{\bullet-}$  to mineralize organic substances. It is a good alternative to hydroxyl radicals-based AOPs as  $\text{SO}_4^{\bullet-}$  is a highly reactive species, with an oxidation potential similar to  $\bullet\text{OH}$ , which is within the range of 2.5-3.1 V (Deng and Zhao, 2015). The utilization of  $\text{SO}_4^{\bullet-}$  in degradation of organic pollutants possess some advantages over the conventional AOPs using  $\bullet\text{OH}$ . For instance,  $\text{SO}_4^{\bullet-}$  react more efficiently with organic compounds over the pH range of 2 to 8. Besides,  $\text{SO}_4^{\bullet-}$  can provide better contact and better mass transfer to targeted organic compounds as they have half-life of around 40  $\mu\text{s}$ , which is much longer than  $\bullet\text{OH}$  with half-life of 20 ns.  $\text{SO}_4^{\bullet-}$  react with organic compounds through electron transfer. This reaction can degrade organic compounds containing aromatic  $\pi$  bond and unsaturated bonds effectively (Rodriguez, et al., 2018).

### 2.5.1 Photolysis

Photolysis is a chemical process that involves interaction between photons and organic compounds. During this reaction, chemical bonds between organic compounds are broken down by photons generated from various sources such as visible light, ultraviolet light, x-ray and gamma ray (Speight, 2017). In water purification process, AOPs are often carried out by using light irradiation to decompose oxidants, such as  $H_2O_2$ , PS and PMS. Photolysis of these powerful oxidants using light irradiation will generate oxidative radicals, such as  $\bullet OH$  and  $SO_4\bullet^-$ , which enable satisfactory elimination of organic dyes (Petrier, 2015). Equations (2.5) to (2.7) summarize the generations of  $\bullet OH$  and  $SO_4\bullet^-$  through the photolysis of  $H_2O_2$ , PS and PMS, respectively. The oxidative radicals produced will attack and oxidize organic compounds through hydrogen atoms abstraction, as illustrated in Figure 2.9 (Terracciano, et al., 2018).

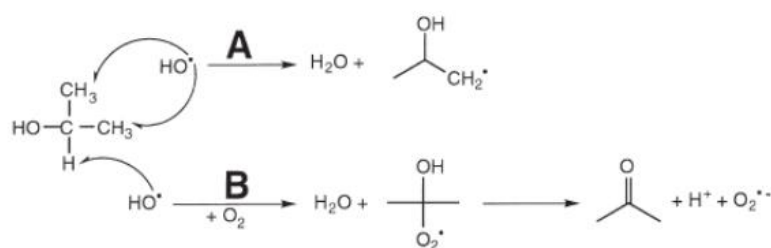


Figure 2.9: Hydrogen Atoms Abstraction (Ragnar, et al., 1999)

### 2.5.2 Photocatalysis

Heterogeneous photocatalysis is one of the effective dye degradation methods. This photocatalytic method can be achieved by using semiconductors as catalyst and light irradiation as activator. Among the various semiconductors such as  $TiO_2$ ,  $ZnO$ , cadmium sulfide and zinc sulfide,  $TiO_2$  is the most widely investigated photocatalyst due to its high chemical stability, non-toxicity, cost-effectiveness, high photo-activity and environmentally friendly features (Lu, et al., 2019).

The overall mechanism of photocatalytic oxidation is illustrated in Figure 2.10. During photocatalytic oxidation, excitation process first occurs when the light irradiation exceeds the band-gap energy of catalyst used. As shown in Equation (2.8), the unpaired electrons ( $e^-$ ) which primarily located at the valence band are promoted into the conduction band, leaving holes ( $h^+$ ) behind. The photogenerated holes when reach the surface of catalyst, react with water and surface-adsorbed hydroxyl to produce  $\cdot\text{OH}$ , as presented in Equations (2.9) and (2.10). Meanwhile, superoxide radicals ( $\cdot\text{O}_2^-$ ) are produced when the migrated electrons reached the surface of catalyst and react with adherent oxygen, as illustrated in Equation (2.11). The generation of  $\text{H}_2\text{O}_2$  will then occur in the subsequent reaction and leads to the production of more  $\cdot\text{OH}$ , as presented in Equations (2.12) and (2.13) (Zhu, Cai and Sun, 2018).

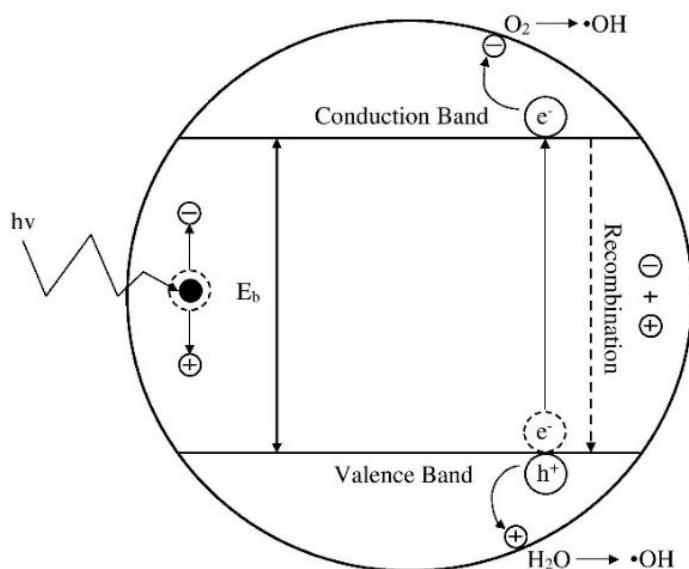
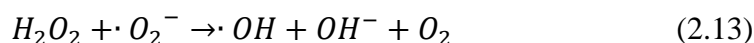
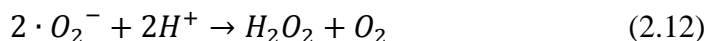


Figure 2.10: Mechanism of Photocatalytic Oxidation

### 2.5.3 Other Advanced Oxidation Processes

Fenton process is one of the most effective AOPs in degrading organic pollutants. The term ‘Fenton reagent’ is defined as a chemical, which consist of ferrous ion and hydrogen peroxide. Among various reactants used in AOPs, Fenton reagent is found to be the most easily handled reactant, which provides high degradation level at atmospheric temperature and pressure (Pawar and Gawande, 2015). Although  $H_2O_2$  is a strong oxidant, it alone is not effective in the removal of certain organic contaminants at high concentration. Improvements can be made by combining  $H_2O_2$  with transition metals, such as iron salt. The general mechanism of Fenton reaction is the utilization of ferrous ion ( $Fe^{2+}$ ) and ferric ion ( $Fe^{3+}$ ) as catalysts for the decomposition of hydrogen peroxide to produce  $\bullet OH$ , as presented from Equations (2.14) to (2.18) (Medien and Khalil, 2010). The  $\bullet OH$  and peroxy radicals ( $HO_2\bullet$ ) generated can then degrade dye molecules existed in wastewater, as illustrated in Figure 2.11.

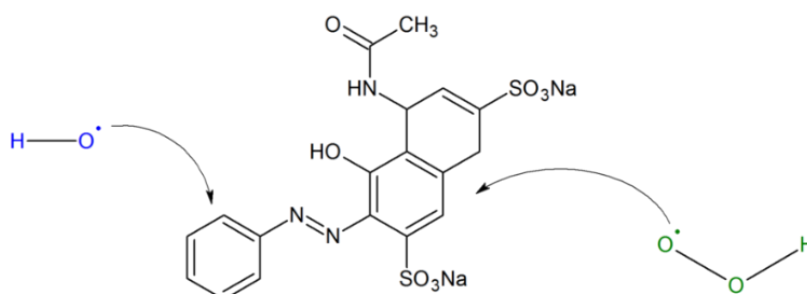
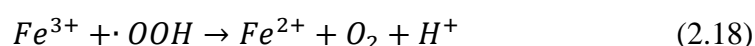
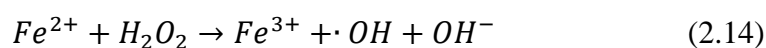
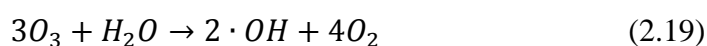


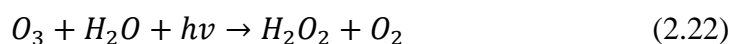
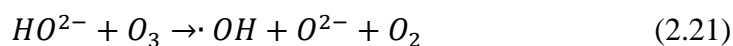
Figure 2.11: Degradation of Red 2G by Hydroxyl and Peroxyl Radicals (Bruin, 2015)

Ozonation is one of the promising methods that can be used for the removal of organic compounds existed in wastewater. Ozone is a strong oxidant with oxidative potential of 2.07 V and 1.25 V in acidic solution and basic

solution, respectively. Ozonation process is accomplished into two mechanisms, which is direct ozonation and indirect ozonation. Direct ozonation involves the electrophilic attack of organic compounds while indirect ozonation attack organic compounds through the formation of  $\bullet\text{OH}$  (Wang and Xu, 2012). Under direct ozonation, ozone is unable to react with the neutral form of organic compound as reaction occurs only when organic compounds are in their dissociated and ionised form. Thus, the production of  $\bullet\text{OH}$  during indirect ozonation can initiate the indiscriminate oxidation (Deng and Zhao, 2015). The overall ozonation reaction is expressed in Equation (2.19).



Ozone oxidation process can be enhanced through the combination with hydrogen peroxide or photolysis using ultraviolet irradiation. By involving hydrogen peroxide in this reaction, additional  $\bullet\text{OH}$  can be produced through a different pathway, as presented in Equations (2.20) and (2.21). In photolysis-ozonation, ozone reacts fast with water through insertion into its OH bond and this causes the production of hydrogen peroxide, as illustrated in Equation (2.22) (Wang and Xu, 2012). As shown in Equation (2.23), the hydrogen peroxide produced will then dissociated into  $\bullet\text{OH}$  as influenced by the ultraviolet irradiation.



Sonolysis involves the utilization of ultrasound with frequency range of 20 kHz-10 MHz to perform oxidation. The overall mechanism of sonolysis is illustrated in Figure 2.12. During this reaction, cavitation bubbles are formed in water. The cavitation bubbles produced will grow in size and gradually get collapsed. The dissipation of stored energy will cause these bubbles to explode, leads to the degradation of organic molecules. Degradation of organic compounds is achieved via pyrolysis at temperature and pressure within 3000-

5000 K and 500-1000 atm, respectively. During pyrolysis,  $\bullet\text{OH}$  are generated through the dissociation of water molecules, which further assist in the oxidation of organic compounds (Mishra, et al., 2017).

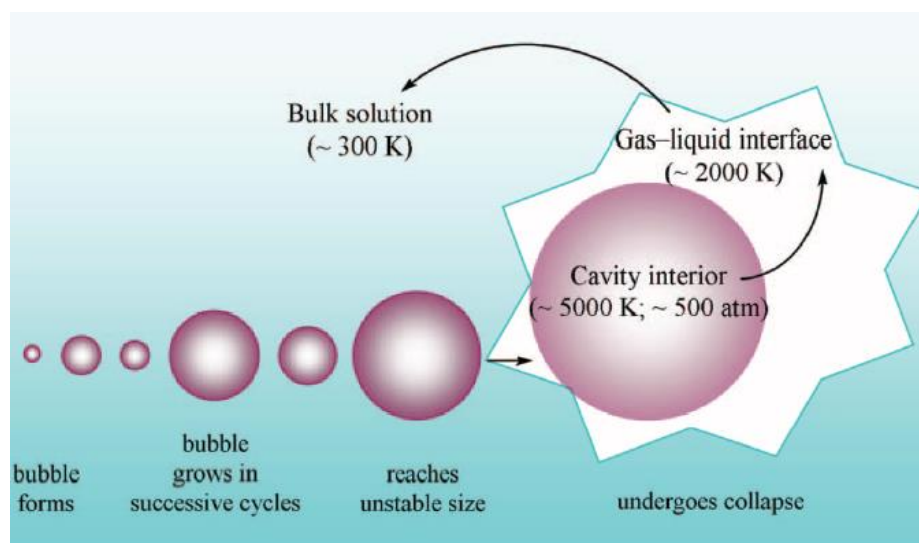


Figure 2.12: Mechanism of Sonolysis Oxidation (Wang and Xu, 2012)

## 2.6 Design of Experiment

Instead of carrying out a series of experiment for the determination of optimum operating conditions, various experimental design methods can be used for the optimization of process parameter. Design Expert is one of the popular analytical software that is specifically used to perform design of experiment. Type of surface designs that can be used in Design Expert for parameters optimization are central composite design (CCD), Box-Behnkan design and one factor design. According to literatures, response surface methodology (RSM) based CCD is the most widely-used method in the optimization of various processes. For example, Aghdasinia, et al. (2017) had studied the optimization of textile dye removal using CCD while Mortazavian, Saber and James (2019) applied CCD for the optimization of photocatalytic degradation of dye.

CCD is useful in RSM and it works by building a quadratic model for the response variables. As illustrated in Figure 2.13, a CCD model is generally built up by a set of  $2^n$  factorial points (cube points), which consisting of a set of  $2n$  axial points and a set of centre points, by which  $n$  is the number of independent variables. By using CCD, each variable is investigated at two levels, where axial points are used for screening analysis to check the variance of model

prediction while centre points are necessary for the estimation of experimental error (Behera, et al., 2018).

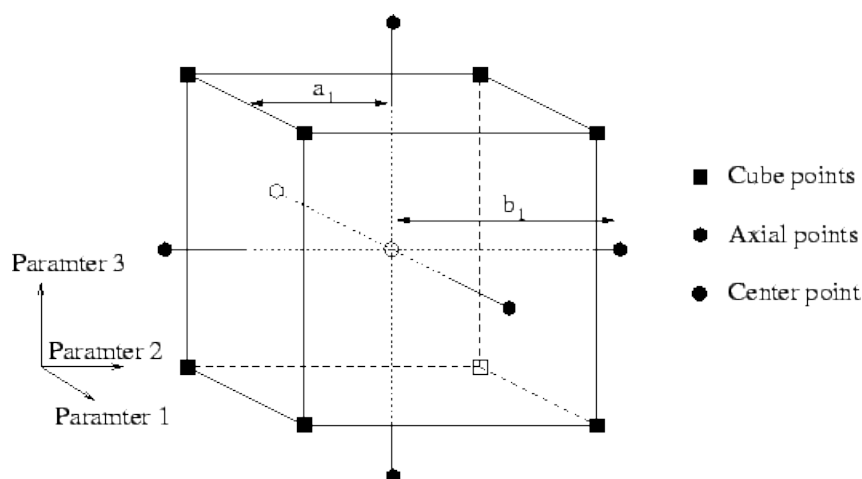


Figure 2.13: CCD model

RSM is a combination of mathematical and statistical model, which can determine regression model and optimize response of an experiment that is affected by a few independent variables. Apart from optimizing and improving process parameters, RSM can analyse the interaction between parameters in studied (Behera, et al., 2018). Before carrying out optimization using RSM, several sets of preliminary experiments are required to be conducted to determine the range and level of experimental factors (Mortazavian, Saber and James, 2019). After that, the experimental runs are randomized and the responses obtain will be used to generate an empirical model, as shown in Equation (2.24). This empirical model shows the correlation between independent variables and response. The fit of model can then be examined by using analysis of variance (ANOVA).

$$Y = \beta_0 + \sum_{i=1}^n \beta_i X_i + \sum_{i=1}^n \beta_{ii} X_i^2 + \sum_{i=1}^n \sum_{j=i+1}^n \beta_{ij} X_i X_j + \varepsilon \quad (2.24)$$

Where,

$Y$  = predicted response

$\beta_0$  = constant coefficient

$\beta_i$  = linear coefficient

$\beta_{ii}$  = quadratic coefficient

$\beta_{ij}$  = interaction coefficient

$n$  = number of factors study

$X_i, X_j$  = coded values of variable parameters

$\varepsilon$  = random error

Suitability of the developed regression model can be examined by using ANOVA. Generally, ANOVA is used to examine the significant of regression model as well as the significance of individual model coefficients. The degree of significant of all individual are presented by using  $F$ -value and  $P$ -value.  $F$ -value is the ratio of the mean square of model to the mean square of residual, indicating whether the model variation is significance as comparing with residual error (Aghdasinia, et al., 2017). On the other hand,  $P$ -value is the probability of  $F$ -value that is used to test the null hypothesis. A model will be considered significant when its  $P$ -value is less than 0.05. Therefore, a model or coefficient is considered significant only when two conditions are fulfilled, by which its  $F$ -value is high and  $P$ -value is lower than 0.05. Apart from these, ANOVA provides some other important information such as standard deviation and  $R^2$  value of the model. A small standard deviation obtained indicates the model is good as it gives near values between actual values and predicted values of the response. Furthermore, the value of  $R^2$  indicates up to what extent the model can estimate the experimental data (Behera, et al., 2018).

Besides, ANOVA can be used to investigate the interaction between independent variables and response by providing response surface and contour plot. Figure 2.14 shows the response surface and contour plot obtained from the study conducted by Mortazavian, Saber and James (2019), which objective is to optimize photocatalytic degradation of Acid Blue. It could be observed that, when other parameters such as reactant dosage and reacting time were set at constant, operating pH within 2 to 3.5 and initial dye concentration within 20 to 90 mg/L could provide nearly 100 % of dye removal.

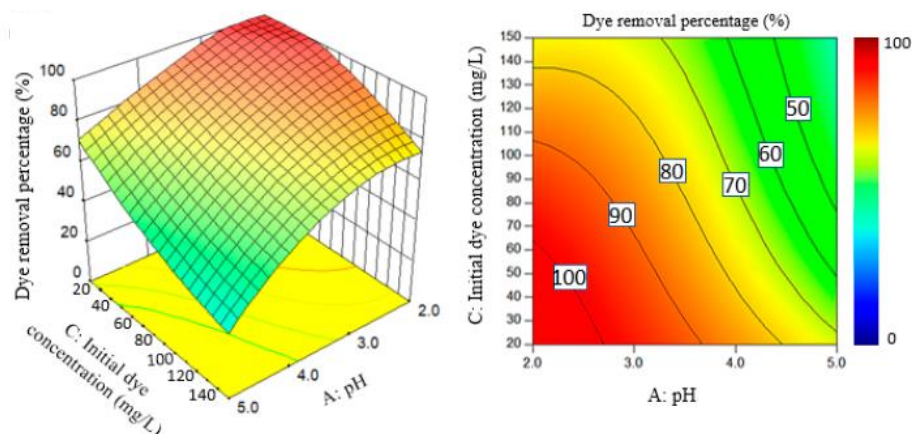


Figure 2.14: Response Surface and Contour Plots (Mortazavian, Saber and James, 2019)

## 2.7 Parameter Studies

Parameter studies are essential to determine the efficiency of a catalyst or reactant in the removal of organic dye. Parameters that could affect the photocatalytic removal of organic dye include type of catalysts, type of oxidants, catalyst dosage, oxidant dosage and pH.

### 2.7.1 Effect of Different Types of Oxidants

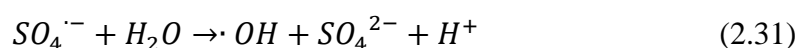
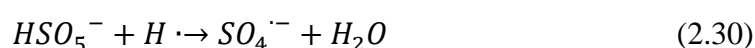
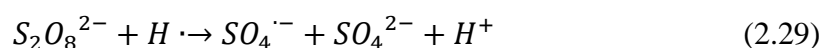
Photolysis in combination with  $H_2O_2$  is the most commonly used AOP technique in degrading toxic organics. This process involves generation of  $\bullet OH$  through photolysis of  $H_2O_2$ , as shown in Equation (2.25). Increasing  $H_2O_2$  concentration will increase  $\bullet OH$  formation, which enhances oxidation process, but only up to an optimum point. When  $H_2O_2$  is in excess, photolytic degradation of organic compounds will be inhibited due to scavenging effect (Wang and Xu, 2012).



AOPs based on light irradiation with PS and PMS were employed for degradation of organic substances in water treatment process. The common PS used in AOPs are sodium persulfate ( $Na_2S_2O_8$ ) and potassium persulfate ( $K_2S_2O_8$ ) while common PMS used in AOPs is potassium peroxydisulfate ( $K_2S_2O_8$ ), which also known as Oxone. Although PS and PMS themselves are

strong oxidizing agent with oxidation potential of 2.01 V and 1.82 V, respectively, they react with organic compounds at low reaction rate. In order to perform effective degradation of organic compounds, appropriate activation such as light irradiation should be provided for the generation of  $SO_4^{\bullet-}$  and  $\bullet OH$  (Wang and Wang, 2018).

For the activation of PS and PMS using light irradiation, three mechanisms are involved. As shown in Equations (2.26) and (2.27), fission of O-O bond first occurs when persulfate ion ( $S_2O_8^{2-}$ ) and peroxymonosulfate ion ( $HSO_5^-$ ) hit by photons and leads to the production of  $SO_4^{\bullet-}$ . In addition, water molecules will produce electrons under light irradiation, which assist in the activation of PS and PMS through electron conduction, as presented from Equations (2.28) to (2.30) (Wang and Wang, 2018). Lastly, the  $SO_4^{\bullet-}$  generated can further react with water to produce  $\bullet OH$ , as shown in Equation (2.31). The presence of both strong oxidants,  $\bullet OH$  and  $SO_4^{\bullet-}$  in this reaction contributes to the high ability of PS and PMS in degrading organic dyes.



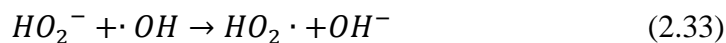
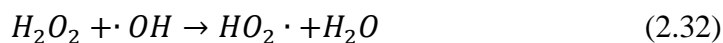
### 2.7.2 Effect of Catalyst Dosage

The dosage of catalyst is a considerable parameter in determining the efficiency of photocatalytic oxidation process. Typically, the increases in catalyst dosage will increase the amount of active sites that is available for reactions such as generation of  $\bullet OH$  to take place. According to Borji, et al. (2014), increased in catalyst dosage would increase the available active sites of catalyst and increase the number of photons absorbed by the catalyst, which led to the high efficiency of photocatalysis. However, beyond a certain limit of catalyst dosage, degradation efficiency of organic compounds started to decline as the excess catalyst caused solution to turn turbid. These excess catalysts acted as shield and

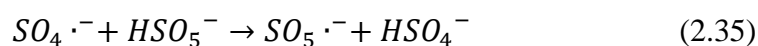
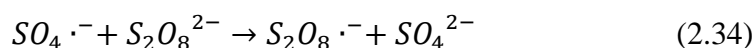
obstructed the penetration of light irradiation into the reacting system. This resulted in the loss of catalyst surface area available for light absorption to take place and consequently led to the reduction in catalytic activity.

### 2.7.3 Effect of Oxidant Dosage

During AOPs, increasing oxidant dosage will generally improve dye degradation efficiency as it increases the generation of  $\bullet\text{OH}$  and  $\text{SO}_4\bullet^-$ , which involve in the decolourization and mineralization of organic dyes. However, when the oxidant concentration increases above the limiting point, degradation efficiency begins to reduce as the generated radicals will in turn react with the excessive primary oxidant to produce less oxidative radicals. For instance, as illustrated in Equations (2.32) and (2.33), scavenging process occurs when excessive concentration of  $\text{H}_2\text{O}_2$  is used, where the  $\text{H}_2\text{O}_2$  will react with  $\bullet\text{OH}$  to form  $\text{HO}_2\bullet$ , which is less effective in the degradation of organic compounds (Wang and Xu, 2012).

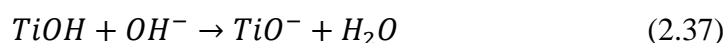


Besides, scavenging effect occurs when excessive PS is used in the degradation of organic dye, where  $\text{S}_2\text{O}_8^{2-}$  will react with the generated  $\text{SO}_4\bullet^-$  to produce persulfate radicals ( $\text{S}_2\text{O}_8\bullet^-$ ), as presented in Equation (2.34) (Gu, et al., 2019). Same goes to PMS, excessive PMS causes side reaction by which the generated  $\text{SO}_4\bullet^-$  will react with  $\text{HSO}_5^-$  to produce peroxymonosulfate radicals ( $\text{SO}_5\bullet^-$ ), as presented in Equation (2.35) (Jiang, Qiu and Sun, 2018). These alternative radicals possess weaker oxidation ability than the desired  $\bullet\text{OH}$  and  $\text{SO}_4\bullet^-$ , thus contributed to the low efficiency of organic dye degradation.



#### 2.7.4 Effect of Solution pH

In photocatalytic process, solution pH is one of the important parameters as it governs the surface charge properties of the catalyst and therefore the adsorption of organic dye onto the catalyst. Generally, different types of photocatalyst required different solution pH to achieve efficient degradation of organic dyes as different catalyst possess different point of zero charge. For instance, the point of zero charge of  $TiO_2$  is at pH 6.8, indicating that  $TiO_2$  surface is negatively charged under alkaline condition of pH more than 6.8 and positively charge under acidic condition of pH less than 6.8 (Alkaim, et al., 2014). This is mainly because, under acidic and alkaline condition, surface of  $TiO_2$  will be protonated and deprotonated, respectively, as illustrated in Equations (2.36) and (2.37) (Kumar and Pandey, 2017).



Besides, different organic dyes can be degraded effectively under different solution pH. At low solution pH, surface of catalyst appears positively charged and thus favours the adsorption of anionic dye, which happens due to the attraction of oppositely charged ions. In contrast, catalyst surface appears negatively charged during high solution pH, resulting in the effective adsorption of cationic dyes (Salleh, et al., 2011). According to Niu (2013), the photocatalytic degradation of Methyl Orange, which is an anionic dye, decreased with increased solution pH and the optimum degradation happened at pH 2.

#### 2.8 Kinetic Study

Analysis of dye degradation kinetic is necessary for better understanding in the reaction mechanism. The study of reaction kinetic involves developing a kinetic model through analysis of changes in reactants concentration as a function of time. The kinetic order of a reaction can be determined by investigating whether the experimental data is well-fitted to pseudo zero order, pseudo first order or pseudo second order kinetic model. The reaction rate of a zero-order reaction is independent of the reactant concentration and its kinetic model is described in

Equation (2.38). As illustrated in Equation (2.39), the reaction rate of a first-order reaction is dependent to the concentration of one reactant. On the other hand, a second-order reaction has either a reaction rate proportional to the square of one reactant or its reaction rate depends on the concentration of two reactants (LibreTexts, 2019). The pseudo second order kinetic models are presented in Equations (2.40) and (2.41).

$$r = -\frac{d[A]}{dt} = k_{app} \quad (2.38)$$

$$r = -\frac{d[A]}{dt} = k_{app}[A] \quad (2.39)$$

$$r = -\frac{d[A]}{dt} = k_{app}[A]^2 \quad (2.40)$$

$$r = -\frac{d[A]}{dt} = k_{app}[A][B] \quad (2.41)$$

Where,

$r$  = reaction rate

$[A]$  = concentration of reactant A

$[B]$  = concentration of reaction B

$k_{app}$  = apparent reaction constant

## CHAPTER 3

### METHODOLOGY AND WORK PLAN

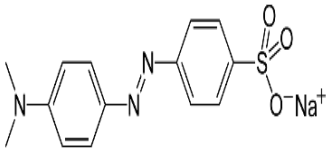
#### 3.1 Materials and Chemicals

The list of materials and chemicals used in the experiment along with their specifications are stated in Table 3.1. The organic dye used in this experiment was Methyl Orange, which is an azo dye commonly used in the textile industry. Table 3.2 shows the structure and chemical properties of Methyl Orange.

Table 3.1: Materials and Chemicals Used in Experiment

Chemical Reagent	Purity (%)	Brand	Purpose
Coconut shell	-	-	Biochar source
Methyl Orange	99	R&M	Organic dye
Zn(NO <sub>3</sub> ) <sub>2</sub>	99	Schmidt	Zinc precursor
TTIP	97	Sigma-Aldrich	Titanium precursor
FeCl <sub>3</sub>	99	R&M	Iron precursor
Melamine	99	Merck	g-C <sub>3</sub> N <sub>4</sub> precursor
H <sub>2</sub> O <sub>2</sub>	30	Sigma-Aldrich	Oxidant
Potassium persulfate (K <sub>2</sub> S <sub>2</sub> O <sub>8</sub> )	99	Merck	Oxidant (PS)
Potassium peroxymonosulfate (KHSO <sub>5</sub> )	45	Merck	Oxidant (PMS)
Ethanol	95	System	Solvent
Potassium carbonate (K <sub>2</sub> CO <sub>3</sub> )	99.5	Schmidt	Precipitator
Ammonium hydroxide (NH <sub>4</sub> OH)	25	R&M	Precipitator
Hydrochloric acid (HCl)	37	Sigma-Aldrich	pH adjuster
Sodium hydroxide (NaOH)	97	Sigma-Aldrich	pH adjuster

Table 3.2: Properties of Methyl Orange

Dye	Structure	Classification	Molecular Weight (g/mol)	Maximum Wavelength Absorption (nm)
Methyl Orange		Azo Anionic Acid	327.33	464

### 3.2 Equipment

Instruments involved in the experiment along with their models and functions are listed in Table 3.3. Carbolite furnace and ultrasonic bath were used for biochar composites synthesis while SEM-EDX, XRD, FTIR, TGA, surface area analysis, zeta potential analysis and UV-Vis DRS were used for their characterizations. Meanwhile, during degradation study, the magnetic stirrer was used to provide uniform mixing for dye solution, while the degradation efficiency of Methyl Orange was examined using a UV-Vis spectrophotometer. Besides, LED lamp was used to provide visible light irradiation for the photocatalytic degradation of dyes. COD reactor and COD spectrophotometer were used to determine the COD removal efficiency.

### 3.3 Overall Experiment Flowchart

Figure 3.1 shows the flowchart of the overall research study. First of all, coconut shell-derived biochar was impregnated in precursors and calcined to produce various biochar composites. Organic dye removal efficiency in the presence of biochar composites was examined, followed by the characterization process. Parameter studies were conducted using different oxidants, catalyst dosage, oxidant dosage and solution pH. Optimization studies were then conducted using CCD. A kinetic study was carried out to determine the kinetic order of the reaction. Lastly, a COD analysis was conducted to identify the organic compounds in the sample solution.

Table 3.3: Instruments Used in Experiment

<b>Instrument</b>	<b>Model</b>	<b>Function</b>
Carbolite furnace	Carbolite RHF 1500	Calcination of biochar and composites
Ultrasonic bath	WiseClean WUC A03H	Ultrasonication
SEM-EDX	Hitachi SEM Model S-3400N	Surface methodology and elemental analysis
XRD	Shimadzu XRD-6000	Crystallinity characterization
FTIR	Nicolet IS10	Functional group characterization
TGA	Perkin Elmer STA8000	Thermal stability characterization
Surface area analysis	Micromeritics	Surface area characterization
Zeta potential analysis	Horiba Scientific SZ-100	Surface charge analysis
UV-Vis DRS	Perkin Elmer	Reflectance and band gap energy determination
LED lamp	Philip	Visible light source
UV-Vis spectrophotometer	Jenway 6320C	Analysis of dye concentration
COD reactor	DRB 200	Allow reaction between oxidant and sample solution
COD spectrophotometer	HACH DR 3900	Determination of COD value

### 3.4 Experimental Setup

The experimental setup for photocatalytic degradation of Methyl Orange in the presence of biochar composite is demonstrated in Figure 3.2. Typically, after adding catalyst into the Methyl Orange solution, the solution was stirred under the dark condition for 30 minutes to achieve equilibrium adsorption-desorption state. After that, oxidant was added into the solution, followed by constant stirring under visible light irradiation. For liquid sample analysis, sample solution was collected in a 5 minutes interval and concentration of Methyl Orange was measured using a UV-Vis spectrophotometer.

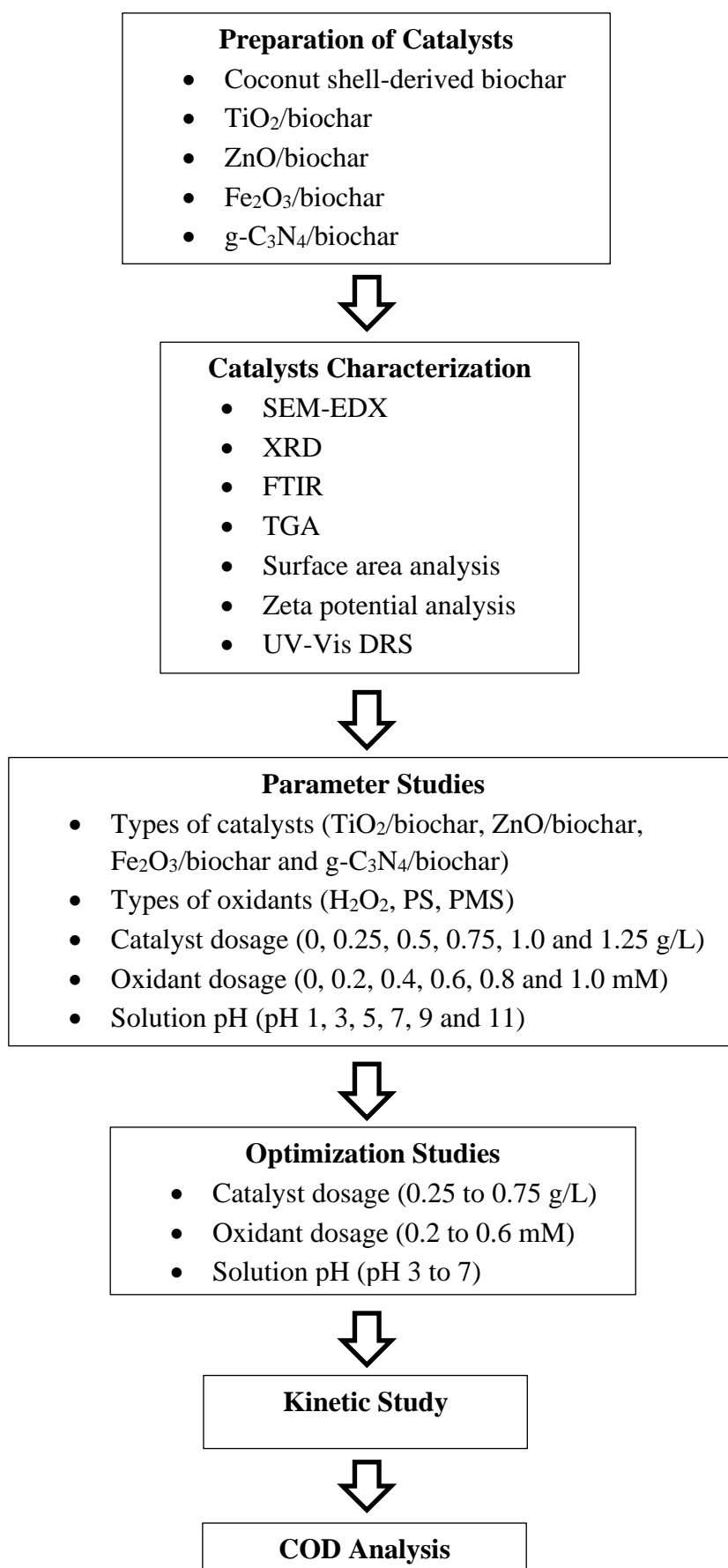


Figure 3.1: Overall Research Flowchart on This Study

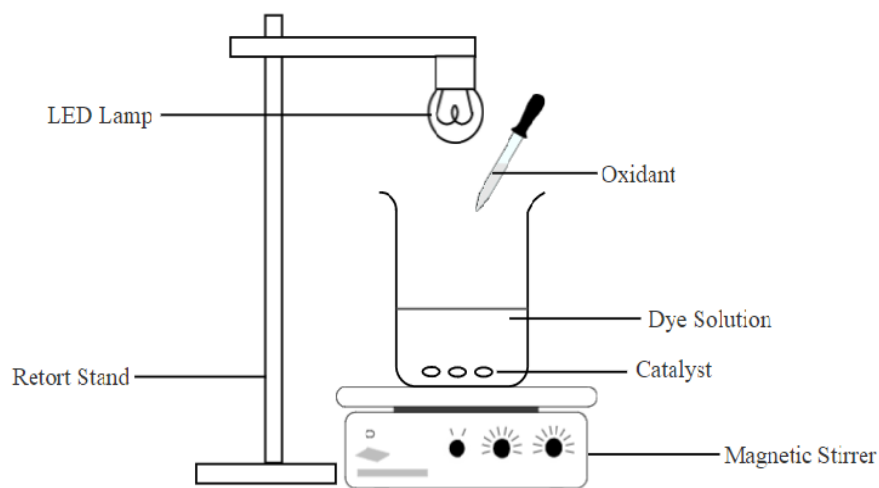


Figure 3.2: Schematic Diagram for Photocatalytic Degradation of Dyes

### 3.5 Synthesis of Catalysts

All the catalysts being studied were synthesized using common methods as proposed by researchers. Besides, all the biochar composites were prepared by dispersing an equal weight percentage of biochar in the catalyst precursors.

#### 3.5.1 Synthesis of Biochar from Coconut Shell

For the synthesis of biochar, coconut shells were first collected and cut into smaller pieces. After rinsing with distilled water, coconut shells were dried in an oven at 80 °C for 12 hours. After that, the coconut shells were calcined under N<sub>2</sub> environment at 500 °C for 2 hours to produce the biochar. After cooling down, biochar was crushed, sieved and stored at ambient temperature for further usage.

#### 3.5.2 Synthesis of Biochar Composites

TiO<sub>2</sub>/biochar was synthesized using the sol-gel method as proposed by Kim and Kan (2016). First of all, biochar was dispersed in 40 mL of water by ultrasonication for 15 minutes, which then followed by the addition of 10 mL TTIP and 40 mL of ethanol. After that, the solution was stirred at ambient temperature for 1 hour. The mixture was then heated to evaporate and the solid product was rinsed using distilled water. After drying in an oven at 80 °C for 12 hours, the dried powder was calcined at 500 °C for 2 hours to yield the TiO<sub>2</sub>/biochar.

ZnO/biochar was synthesized using the co-precipitation method as proposed by Farahmandjou and Jurablu (2014). Firstly, biochar was dispersed in 100 mL of water. Under constant stirring, 0.03 M of  $\text{Zn}(\text{NO}_3)_2$  and 0.05 M of  $\text{K}_2\text{CO}_3$  were added into the solution. The solution was stirred at ambient temperature for 1 hour for the precipitation of zinc carbonate. The solid products were rinsed, dried and calcined in the same condition as the preparation of  $\text{TiO}_2$ /biochar to produce ZnO/biochar.

$\text{Fe}_2\text{O}_3$ /biochar was synthesized using the co-precipitation method as proposed by Farahmandjou and Soflaee (2015). First of all, biochar was dispersed in 150 mL of water prior to the addition of 6 g  $\text{FeCl}_3$ . After that, 2 mL of  $\text{NH}_4\text{OH}$  was added dropwise into the solution. The solution was stirred at ambient temperature for 1 hour for the precipitation of ferric hydroxide. The precipitates were then rinsed, dried and calcined in the same condition as the preparation of  $\text{TiO}_2$ /biochar to yield  $\text{Fe}_2\text{O}_3$ /biochar.

For the preparation of g- $\text{C}_3\text{N}_4$ /biochar, the synthesis method proposed by Li, et al. (2019) was referred. First of all, biochar and melamine were dispersed into 100 mL of distilled water through ultrasonication for 15 minutes. After stirring at ambient temperature for 1 hour, the mixture was rinsed, dried and calcined in the same condition as the preparation of  $\text{TiO}_2$ /biochar for the production of g- $\text{C}_3\text{N}_4$ /biochar.

### 3.6 Characterization of Catalysts

SEM was conducted to analyse the surface morphological structure of catalysts. Double-sided tape was used to adhere catalyst on the specimen holder prior to the analysis process. The acceleration voltage of 15 kV and magnification of 3, 5 and 10 kX were used to obtain the scanning electron images. Besides, the elemental composition of the catalysts was determined by coupling SEM with EDX.

XRD analysis was carried out to identify the crystalline structure of catalysts. The Cu-K $\alpha$  ( $\lambda=1.540562 \text{ \AA}$ ) radiation source was manipulated at 40 kV/30 mA and the interference peaks were eliminated by using K-beta filter. All the powdered samples were then placed on the sample holder. After that, a scan step of  $0.02^\circ$  and a scan rate of  $2^\circ/\text{min}$  were set. The intensity of x-ray

diffraction was recorded by controlling the diffraction pattern that emerged in  $2\theta$  ranging from  $10^\circ$  to  $80^\circ$ .

To determine the active functional groups of catalysts using FTIR, attenuated total reflectance (ATR) sampling technique was used. By using a resolution of  $4\text{ cm}^{-1}$  and 16 scans, FTIR spectra of each catalyst were recorded in the spectrum range of  $400$  to  $4000\text{ cm}^{-1}$ . The recognition of functional groups was being conducted by comparing the spectra with established database.

The thermal stability of catalysts was analysed by using TGA. All the samples were subjected to heating, with temperature ranging from  $30^\circ\text{C}$  to  $1000^\circ\text{C}$  under a heating rate of  $10^\circ\text{C}/\text{min}$ . A graph of weight loss against temperature was plotted to determine the number of volatile components that exist in the catalysts.

For surface area analysis,  $0.5\text{ g}$  of each catalyst sample was first degassed at  $150^\circ\text{C}$  to remove impurities. The specific surface area of catalyst was determined by the physical adsorption of liquid nitrogen onto the catalyst surface. After measuring the amount of adsorbate gas, calculation which assume a monolayer of the nitrogen gas was applied.

For surface charge analysis, the zeta potential of catalyst was measured at  $25^\circ\text{C}$ . Typically,  $5\text{ mg}$  of sample powder was dispersed in  $50\text{ mL}$  of  $0.001\text{ M}$  NaCl solution through ultrasonication for 15 minutes. To obtain the isoelectric point, pH of the suspension were adjusted to pH 2, 4, 6, 8 and 10 through the addition of HCl and NaOH. Three zeta potential readings were taken at every solution pH and the average zeta potential value was plotted against the solution pH.

UV-Vis DRS was conducted to determine the absorbances and band gap energies of catalyst. A monolayer of sample powder was added into the sample holder and inserted into a UV-Vis spectrophotometer. The absorbances of catalysts were examined within the wavelength range from  $300$  to  $800\text{ nm}$ . Band gap energies of catalysts could be identified by plotting a Tauc plot based on Kubelka-Munk function.

### **3.7 Parameter Studies**

Parameter studies were carried out by using different types of catalyst, different types of oxidant, different catalyst dosage, different oxidant dosage as well as different solution pH.

#### **3.7.1 Effect of Different Types of Catalyst**

First of all, 100 mL of 10 mg/L Methyl Orange solution was prepared in a beaker. 1 g/L of TiO<sub>2</sub>/biochar was added, followed by 30 minutes of stirring under the dark condition to achieve equilibrium adsorption-desorption state. Then, the solution was irradiated by visible light irradiation. The sample solution was collected in a 10 minutes interval for 60 minutes and subjected to liquid sample analysis. This process was repeated by replacing TiO<sub>2</sub>/biochar with ZnO/biochar, Fe<sub>2</sub>O<sub>3</sub>/biochar and g-C<sub>3</sub>N<sub>4</sub>/biochar. The catalyst with the best photocatalytic degradation efficiency of Methyl Orange was used in the following studies.

#### **3.7.2 Effect of Different Types of Oxidant**

The effect of different oxidant on photocatalytic degradation of Methyl Orange was investigated. Typically, 100 mL of Methyl Orange solution with a concentration of 10 mg/L was prepared in a beaker. After the addition of 1 g/L of catalyst, Methyl Orange solution was stirred for 30 minutes under dark condition. After that, 1 mM of H<sub>2</sub>O<sub>2</sub> was added into Methyl Orange solution. The dye solution was stirred constantly under visible light irradiation. The sample solution was collected in a 5 minutes interval for 30 minutes and their respective degradation efficiency was examined using a UV-Vis spectrophotometer. The procedures were repeated by replacing H<sub>2</sub>O<sub>2</sub> with PS and PMS. Oxidant with the optimum degradation efficiency of Methyl Orange was used in the subsequent studies.

#### **3.7.3 Effect of Catalyst Dosage**

The effect of catalyst dosage on photocatalytic degradation of Methyl Orange was determined by manipulating the catalyst loading between 0, 0.25, 0.5, 0.75, 1.0 and 1.25 g/L. Firstly, 100 mL of 10 mg/L Methyl Orange solution was prepared in a beaker. Different dosage of the catalyst was then added into the

solution, followed by 30 minutes of constant stirring in dark condition to achieve adsorption-desorption equilibrium. After that, 1 mM of oxidant was added into the solution and the solution was stirred under visible light irradiation. The sample solution was collected in a 5 minutes interval for 30 minutes to determine the concentration of Methyl Orange. The optimum catalyst dosage was brought forward to the following studies.

#### **3.7.4 Effect of Oxidant Dosage**

The effect of oxidant dosage on photocatalytic degradation of Methyl Orange was determined by manipulating the oxidant dosage between 0, 0.2, 0.4, 0.6, 0.8 and 1.0 mM. Similarly, 100 mL of 10 mg/L of Methyl Orange solution was prepared, followed by the addition of catalyst with optimal dosage. After achieving adsorption-desorption equilibrium, a different dosage of oxidant was added into the dye solution before visible light irradiation. Under constant stirring, Methyl Orange solution was collected in a 5 minute interval for 30 minutes. The optimum oxidant dosage was identified and carried forward to the following study.

#### **3.7.5 Effect of Solution pH**

The effect of solution pH on the photocatalytic degradation of Methyl Orange was identified by varying solution pH between 1, 3, 5, 7, 9 and 11. The solution pH was adjusted by using NaOH or HCl. Similar to the previous experiment, 100 mL of 10 mg/L of Methyl Orange solution was first prepared. The solution pH was adjusted to the desired pH before the addition of catalyst and oxidant. After that, the sample solution was collected in a 5 minutes interval for 30 minutes to determine the degradation of Methyl Orange in different solution pH.

### **3.8 Design of Experiment**

In this study, RSM was used to study the interactive relationship between independent variables that would affect the photocatalytic degradation of Methyl Orange. The three independent variables being studied were catalyst dosage ( $X_1$ ), oxidant dosage ( $X_2$ ) and solution pH ( $X_3$ ) while the response variable to be optimized was degradation efficiency of Methyl Orange. In this situation, a total of 20 experimental runs were required for the CCD model,

which could be calculated by using Equation (3.1). Apart from the independent variables involved in the RSM, the remaining factors, which included the type of catalyst, type of oxidant, reaction time and concentration of Methyl Orange solution were set as constant.

$$\text{Total runs} = 2^n \text{ (factorial)} + 2n \text{ (axial)} + 6 \text{ (center)} \quad (3.1)$$

The ranges and levels of independent variables were determined after conducting several preliminary experiments. As presented in Table 3.4, each independent variable was studied at 5 coded levels which were -1.68, -1, 0, 1 and 1.68. Besides, Table 3.5 represented the experiment matrix generated by CCD. For every experimental run, the degradation efficiency of Methyl Orange was obtained after 30 minutes of the experiment. Besides, the experimental runs were randomized to reduce systematic errors.

Table 3.4: Actual Values of Variables and Their Coded Levels Used in CCD

Variables	Factors	Actual Values for the Coded Levels				
		$-\alpha$ (-1.68)	-1	0	1	$\alpha$ (+1.68)
Catalyst Dosage (g/L)	X <sub>1</sub>	0.08	0.25	0.50	0.75	0.92
Oxidant Dosage (mM)	X <sub>2</sub>	0.06	0.2	0.4	0.6	0.74
Solution pH	X <sub>3</sub>	1.64	3.0	5.0	7.0	8.36

### 3.9 Kinetic Study

The kinetic order for photocatalytic degradation of organic dyes was analysed by investigating whether the experimental results could be well-fitted to pseudo zero, pseudo first or pseudo second order kinetic models. The kinetic equation previously listed in Equations (2.36) to (2.39) can be transformed into graphical expression as shown in Equations (3.2) to (3.4). A linear plot was obtained when the kinetic model used could accurately describe the experimental results.

Table 3.5: Experiment Matrix of CCD

Standard Order	Point Type	Coded Independent Variable Levels		
		Catalyst	Oxidant	Solution pH
		Dosage, g/L ( $X_1$ )	Dosage, mM ( $X_2$ )	( $X_3$ )
1	Factorial	0.25 (-1)	0.2 (-1)	3.0 (-1)
2	Factorial	0.75 (+1)	0.2 (-1)	3.0 (-1)
3	Factorial	0.25 (-1)	0.6 (+1)	3.0 (-1)
4	Factorial	0.75 (+1)	0.6 (+1)	3.0 (-1)
5	Factorial	0.25 (-1)	0.2 (-1)	7.0 (+1)
6	Factorial	0.75 (+1)	0.2 (-1)	7.0 (+1)
7	Factorial	0.25 (-1)	0.6 (+1)	7.0 (+1)
8	Factorial	0.75 (+1)	0.6 (+1)	7.0 (+1)
9	Axial	0.08 (-1.68)	0.4 (0)	5.0 (0)
10	Axial	0.92 (+1.68)	0.4 (0)	5.0 (0)
11	Axial	0.5 (0)	0.06 (-1.68)	5.0 (0)
12	Axial	0.5 (0)	0.74 (+1.68)	5.0 (0)
13	Axial	0.5 (0)	0.4 (0)	1.64 (-1.68)
14	Axial	0.5 (0)	0.4 (0)	8.36 (+1.68)
15	Center	0.5 (0)	0.4 (0)	5.0 (0)
16	Center	0.5 (0)	0.4 (0)	5.0 (0)
17	Center	0.5 (0)	0.4 (0)	5.0 (0)
18	Center	0.5 (0)	0.4 (0)	5.0 (0)
19	Center	0.5 (0)	0.4 (0)	5.0 (0)
20	Center	0.5 (0)	0.4 (0)	5.0 (0)

Pseudo zero order kinetic model:

$$C_t = C_0 - k_{app}t \quad (3.2)$$

Pseudo first order kinetic model:

$$\ln C_t = \ln C_0 - k_{app}t \quad (3.3)$$

Pseudo second order kinetic model:

$$\frac{1}{C_t} = \frac{1}{C_0} + k_{app}t \quad (3.4)$$

Where,

$C_0$  = initial concentration of organic dye (mg/L)

$C_t$  = residual concentration of organic dye at certain time (mg/L)

$k_{app}$  = apparent reaction constant (vary unit)

$t$  = reaction time (min)

### 3.10 Liquid Sample Analysis

For each experiment, Methyl Orange solution was collected in a 5 minutes interval for 30 minutes. The liquid samples were examined through UV-Vis spectrophotometry analysis. During analysis, the absorbance of Methyl Orange was measured using a UV-Vis spectrophotometer at its maximum absorbance wavelength of 464 nm. A calibration curve of absorbance versus dye concentration was plotted to determine the concentration of Methyl Orange in every time interval. The degradation efficiency was determined via Equation (3.5).

$$\text{Degradation Efficiency (\%)} = \frac{C_0 - C_t}{C_0} \times 100\% \quad (3.5)$$

Where,

$C_0$  = initial concentration of organic dye (mg/L)

$C_t$  = residual concentration of organic dye at certain time (mg/L)

COD analysis was conducted to identify the quantity of organic compounds in the dye solution before and after the photocatalytic action. The photocatalytic degradation of Methyl Orange was carried out at the optimum operating condition. The collected dye solution was mixed with COD digestion reagent and heated for 2 hours. The COD value of sample solution was then determined by using COD spectrophotometer.

## CHAPTER 4

### RESULTS AND DISCUSSION

#### 4.1 Characterization of Catalysts

The characterization of pure biochar, g-C<sub>3</sub>N<sub>4</sub>, TiO<sub>2</sub>/biochar, ZnO/biochar, Fe<sub>2</sub>O<sub>3</sub>/biochar and g-C<sub>3</sub>N<sub>4</sub>/biochar composite materials were performed by using SEM-EDX, XRD, FTIR, TGA, surface area analysis and UV-Vis DRS. The purpose is to reveal the properties of surface morphology, elemental composition, crystallinity, functional group, thermal stability, surface area and band gap energy.

##### 4.1.1 SEM-EDX

The surface morphology of synthesized biochar, g-C<sub>3</sub>N<sub>4</sub>, g-C<sub>3</sub>N<sub>4</sub>/biochar and other metal oxide/biochar were studied by using SEM as illustrated in Figure 4.1. The biochar pore diameters were lower than 10 μm as shown in Figure 4.1 (a), which was consistent with the result obtained by Angalaeeswari and Kamaldeen (2017), where the pore diameters of coconut shell-derived biochar were found to be varied from 7.26 μm to 10 μm. These macropores were developed due to the release of volatile compounds during the pyrolysis of coconut shell biomass. These highly porous structures proved the ability of biochar acted as an effective adsorbent due to the presence of a large amount of adsorption sites (Rout, et al., 2016).

Figure 4.1 (b) shows the surface morphology of g-C<sub>3</sub>N<sub>4</sub> in the form of small flakes with observable strip textures, which was a typical structural feature of g-C<sub>3</sub>N<sub>4</sub> synthesized by thermal decomposition (Li, et al., 2019). The average length of g-C<sub>3</sub>N<sub>4</sub> was found to be around 5 μm. For the surface morphology of g-C<sub>3</sub>N<sub>4</sub>/biochar as shown in Figure 4.1 (c), the structure of g-C<sub>3</sub>N<sub>4</sub> remain unchanged though being incorporated in the biochar skeleton. This composite material shows a porous and flake-like structure, proving that both substances retained their pristine structures (Pi, et al., 2015).

The surface morphology of TiO<sub>2</sub>/biochar shows that TiO<sub>2</sub> granules were well dispersed on the biochar with little agglomeration as shown in Figure 4.1 (d). Figure 4.1 (e) shows the irregular spherical shape of ZnO particles and the

majority of them were found to be in the form of aggregates once distributed on the biochar. Figure 4.1 (f) shows that  $\text{Fe}_2\text{O}_3$  particles were in the form of a cluster and exhibited an extremely high degree of agglomeration once distributed on biochar. Farahmandjou and Soflaee (2015) reported that less aggregated sphere-like shape and high crystallinity of  $\text{Fe}_2\text{O}_3$  could be obtained when increasing annealing period up to 4 hours.

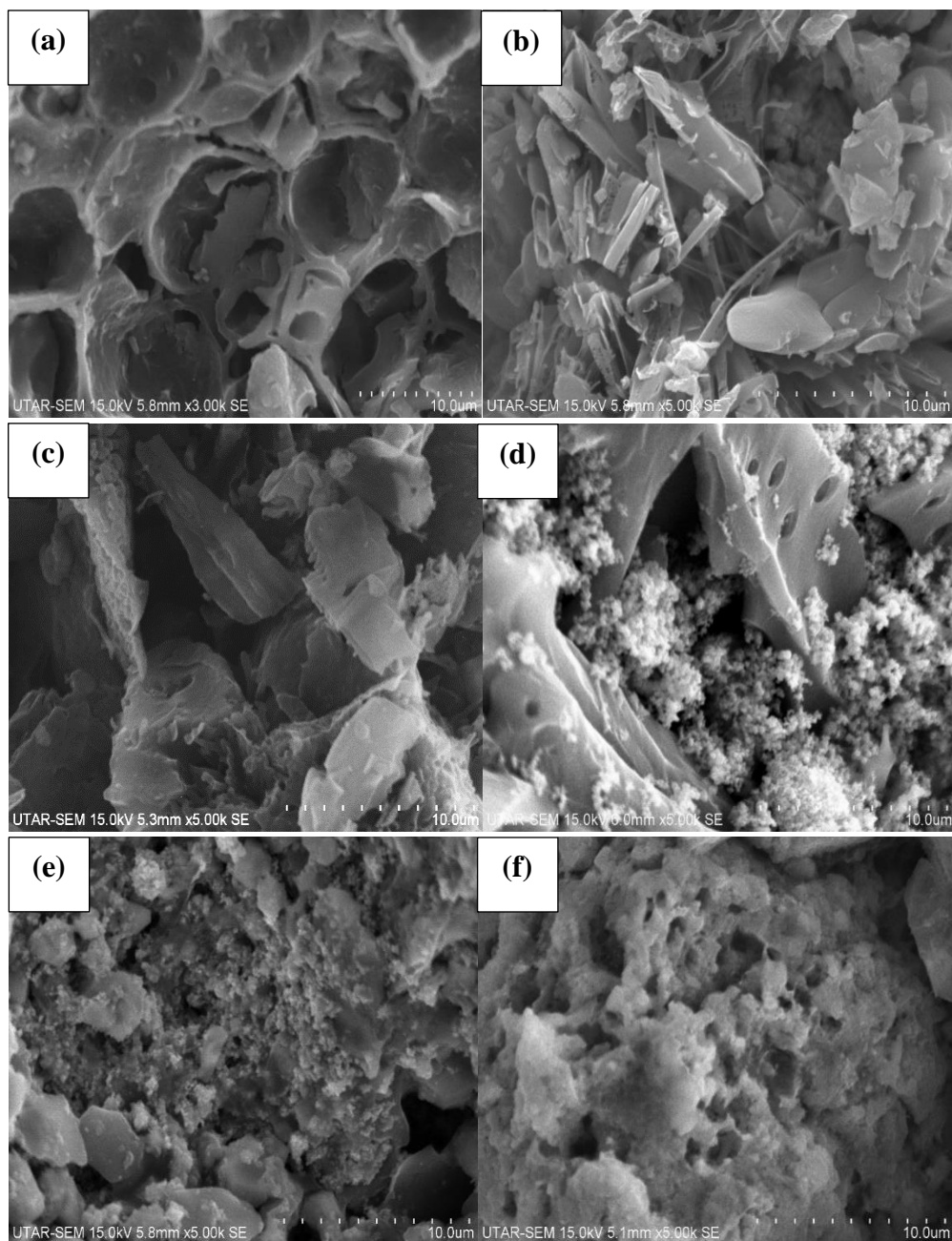


Figure 4.1: SEM Images of (a) Biochar, (b)  $\text{g-C}_3\text{N}_4$ , (c)  $\text{g-C}_3\text{N}_4/\text{biochar}$ , (d)  $\text{TiO}_2/\text{biochar}$ , (e)  $\text{ZnO}/\text{biochar}$  and (f)  $\text{Fe}_2\text{O}_3/\text{biochar}$

The EDX results of particles are shown in Table 4.1. Generally, biochar composed of mainly carbon and oxygen, while the other impurities such as potassium in a negligible amount were also found in biochar. The C/N atomic ratio of pure g-C<sub>3</sub>N<sub>4</sub> was 0.69, which was close to the value of ideal g-C<sub>3</sub>N<sub>4</sub> with a C/N ratio of 0.75. The higher concentration of nitrogen which exceeded the stoichiometric ratio found in this study was mainly due to the incomplete combustion of melamine (Li, et al., 2019). The carbon elements present in the g-C<sub>3</sub>N<sub>4</sub>/biochar increased due to the incorporation of biochar.

The weight percentage of carbon, oxygen and titanium element were 39.65 %, 32.02 % and 28.33 % in TiO<sub>2</sub>/biochar, respectively. In addition, both ZnO/biochar and Fe<sub>2</sub>O<sub>3</sub>/biochar show impurity elements such as potassium and chlorine. This was primarily due to their co-precipitation synthesis method, as K<sub>2</sub>CO<sub>3</sub> and FeCl<sub>3</sub> were used during the synthesis of ZnO and Fe<sub>2</sub>O<sub>3</sub>, respectively. Furthermore, a low carbon weight percentage in both composite materials might be due to the fact that aggregated metal oxide particles were fully distributed and covered on the biochar.

#### 4.1.2 XRD

The XRD results of biochar, g-C<sub>3</sub>N<sub>4</sub>, g-C<sub>3</sub>N<sub>4</sub>/biochar and other metal oxides/biochar are shown in Figure 4.2. Figure 4.2 (a) shows the XRD pattern of biochar derived from the coconut shell. The broad peak at 25° in biochar corresponded to (002) plane in carbon material with amorphous structure (Zakaria, Mansor and Shahrin, 2018). The strong peak at 61° was probably originated from crystalline silicon dioxide, similar to the result obtained by Raju and Rao (2017), where silicon dioxide was found to be one of the major constituents in coconut shell ash. For pure g-C<sub>3</sub>N<sub>4</sub>, the weak peak at 13° and a strong peak at 27° were attributed to the diffraction of (100) and (002) planes of g-C<sub>3</sub>N<sub>4</sub>, respectively. According to Li, et al. (2019), the peak at 13° was originated from the repeating tri-s-triazine ring structure, while the peak at 27° resulted from the accumulation of interlayers along c-axis of the conjugated aromatic structure, which exhibited a graphite layer structure. It was noticed that both peak intensities at 13° and 27° in g-C<sub>3</sub>N<sub>4</sub>/biochar were reduced, indicated that the incorporation of biochar inhibited the formation of bulk layered g-C<sub>3</sub>N<sub>4</sub> during melamine polycondensation process (Li, et al., 2019).

Table 4.1: EDX Results of Different Catalysts

Catalyst	C (%)		O (%)		N (%)		Ti (%)		Zn (%)		Fe (%)		K (%)		Cl (%)	
	Wt.	At.	Wt.	At.	Wt.	At.	Wt.	At.	Wt.	At.	Wt.	At.	Wt.	At.	Wt.	At.
Biochar	88.77	91.32	11.23	8.68	-	-	-	-	-	-	-	-	-	-	-	-
g-C <sub>3</sub> N <sub>4</sub>	37.15	40.80	-	-	62.85	59.20	-	-	-	-	-	-	-	-	-	-
g-C <sub>3</sub> N <sub>4</sub> / biochar	51.54	55.36	-	-	48.46	44.64	-	-	-	-	-	-	-	-	-	-
TiO <sub>2</sub> / biochar	39.65	56.01	32.02	33.96	-	-	28.33	10.03	-	-	-	-	-	-	-	-
ZnO/ biochar	12.17	27.23	24.86	41.76	-	-	-	-	44.44	18.27	-	-	18.53	12.74	-	-
Fe <sub>2</sub> O <sub>3</sub> / biochar	17.09	36.89	22.54	30.32	-	-	-	-	-	-	32.45	15.06	-	-	27.92	17.73

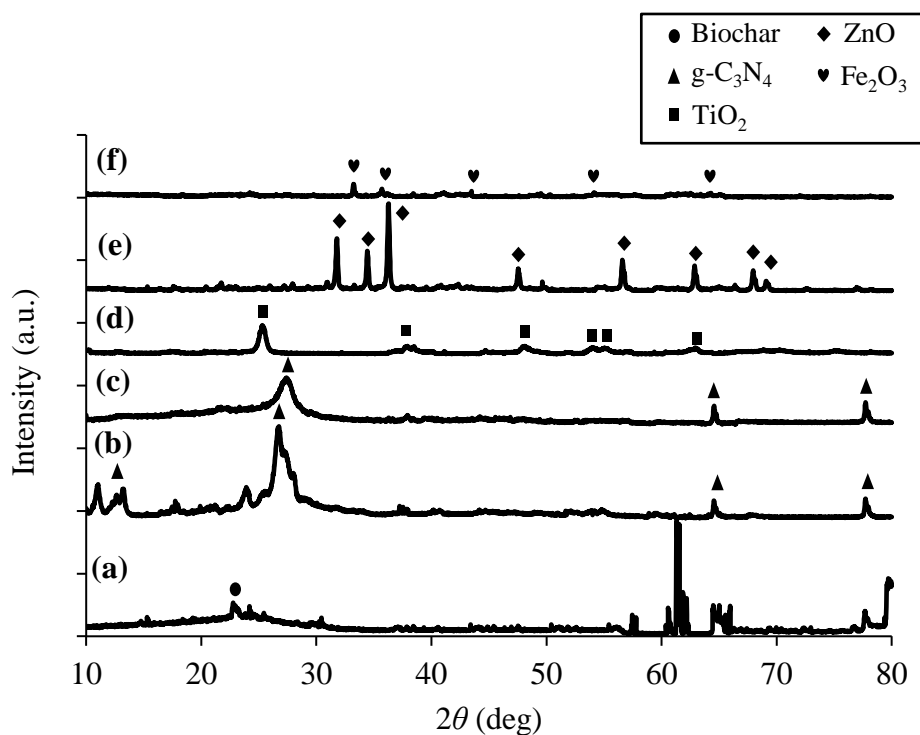


Figure 4.2: XRD patterns of (a) Biochar, (b)  $g\text{-C}_3\text{N}_4$ , (c)  $g\text{-C}_3\text{N}_4/\text{biochar}$ , (d)  $\text{TiO}_2/\text{biochar}$ , (e)  $\text{ZnO}/\text{biochar}$  and (f)  $\text{Fe}_2\text{O}_3/\text{biochar}$

The XRD pattern of  $\text{TiO}_2/\text{biochar}$  shows diffraction peaks at  $25^\circ$ ,  $38^\circ$ ,  $48^\circ$ ,  $54^\circ$ ,  $56^\circ$  and  $63^\circ$ , which were corresponded to the reflection from (101), (004), (200), (105), (211) and (213) planes of  $\text{TiO}_2$ , respectively. All these peak were attributed to anatase- $\text{TiO}_2$ , without any additional peak for rutile and brookite phases (Taweel and Saud, 2016). For  $\text{ZnO}/\text{biochar}$ , the diffraction peaks at  $32^\circ$ ,  $34^\circ$ ,  $36^\circ$ ,  $47^\circ$ ,  $57^\circ$ ,  $63^\circ$ ,  $68^\circ$  and  $69^\circ$  corresponded to the reflection from (100), (002), (101), (102), (110), (103), (112) and (201) crystal planes of ZnO (Farahmandjou and Jurablu, 2014). For  $\text{Fe}_2\text{O}_3/\text{biochar}$ , the diffraction peaks at  $33^\circ$ ,  $36^\circ$ ,  $44^\circ$ ,  $54^\circ$  and  $66^\circ$  corresponded to the (104), (110), (113), (116) and (300) planes of a rhombohedral structure of  $\alpha\text{-Fe}_2\text{O}_3$ , which proved that  $\alpha\text{-Fe}_2\text{O}_3$  was the only metal oxide presented in the composite material (Farahmanjou and Soflaee, 2015). For all the metal oxide composites, the characteristic peak of biochar at  $25^\circ$  could not be seen clearly in the XRD patterns, possibly owing to the coverage of aggregated metal oxide particles on the carbon structure (Lu, et al., 2019).

### 4.1.3 FTIR

The results from the FTIR analysis of biochar, g-C<sub>3</sub>N<sub>4</sub>, g-C<sub>3</sub>N<sub>4</sub>/biochar and other metal oxides/biochar are shown in Figure 4.3. For pure biochar, broad absorption peak appeared at 3376 cm<sup>-1</sup> indicated the -OH bond stretching vibration. The absorption peaks at 1557 cm<sup>-1</sup> and 1148 cm<sup>-1</sup> were attributed to the presence of C=C bond in the aromatic ring and C-O bond, respectively (Zhang, et al., 2018). Besides, a weak absorption band at 744 cm<sup>-1</sup> indicated that C-H bond was present in the coconut shell-derived biochar (Angalaeeswari and Kamaldeen, 2017).

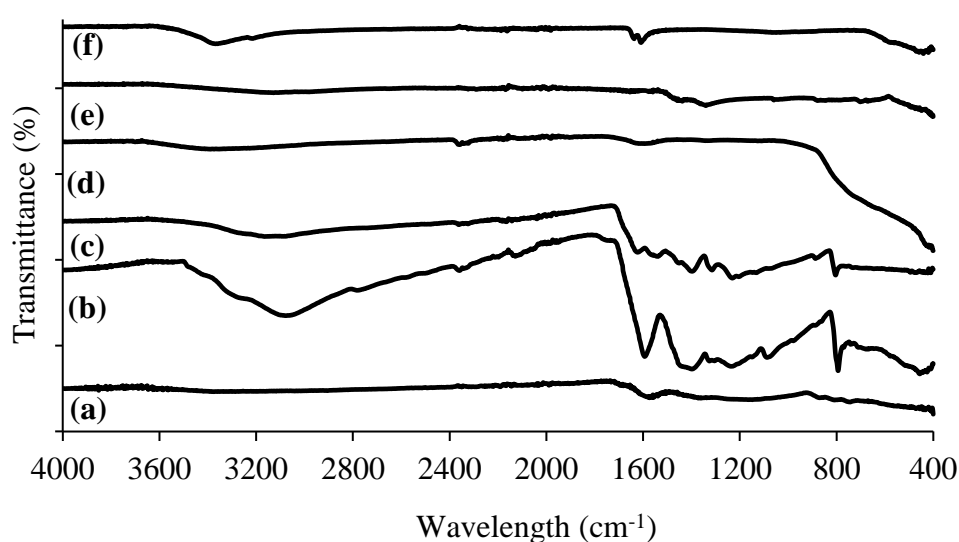


Figure 4.3: FTIR Spectra of (a) Biochar, (b) g-C<sub>3</sub>N<sub>4</sub>, (c) g-C<sub>3</sub>N<sub>4</sub>/biochar, (d) TiO<sub>2</sub>/biochar, (e) ZnO/biochar and (f) Fe<sub>2</sub>O<sub>3</sub>/biochar

For pure g-C<sub>3</sub>N<sub>4</sub>, the broad peak centered at 3080 cm<sup>-1</sup> corresponded to the stretching vibration of primary (-NH<sub>2</sub>) and secondary (=NH) amine group. Besides, the strong band at 794 cm<sup>-1</sup> was derived from the intense bending vibration mode of tri-s-triazine unit. In addition, g-C<sub>3</sub>N<sub>4</sub> presented a series of the bands at 1593 cm<sup>-1</sup>, 1397 cm<sup>-1</sup>, 1232 cm<sup>-1</sup> and 1088 cm<sup>-1</sup>, which could be attributed to the stretching vibration of C-N heterocycles (Li, et al., 2019). The FTIR spectra of g-C<sub>3</sub>N<sub>4</sub>/biochar were substantially similar to the pure g-C<sub>3</sub>N<sub>4</sub>, indicated that the incorporation of biochar did not greatly change the bulk structure of g-C<sub>3</sub>N<sub>4</sub>.

FTIR spectra of TiO<sub>2</sub>/biochar shows a broad absorption peak from 400 cm<sup>-1</sup> to 700 cm<sup>-1</sup>, which were assigned to the stretching vibration of Ti-O bond, indicating the existence of TiO<sub>2</sub> in the composite material (Lu, et al., 2019). Besides, the FTIR spectra show the Zn-O peak from 400 cm<sup>-1</sup> to 600 cm<sup>-1</sup>, suggesting the formation of ZnO on the composite material (Martinez, et al., 2011). The stretching mode of Fe-O was seen at the peak of 500 cm<sup>-1</sup>, confirming the incorporation of Fe<sub>2</sub>O<sub>3</sub> in the composite material (Fard, Mirjalili and Najafi, 2016). For all the metal oxide/biochar, the absorption band at around 3300 cm<sup>-1</sup> and 1600 cm<sup>-1</sup> were related to the stretching and bending vibration of -OH group, respectively (Lu, et al., 2019).

#### 4.1.4 TGA

Figure 4.4 shows the TGA curve of biochar, g-C<sub>3</sub>N<sub>4</sub>, g-C<sub>3</sub>N<sub>4</sub>/biochar and other metal oxides/biochar from 30 °C to 1000 °C at a heating rate of 10 °C/min. According to Zhang, et al. (2018), the heating process could be divided into water evaporation stage and decomposition stage. At the first stage, a small weight loss of less than 10 % within the temperature of 30 °C to 100 °C was noted in the TGA curve of biochar, g-C<sub>3</sub>N<sub>4</sub>, g-C<sub>3</sub>N<sub>4</sub>/biochar and TiO<sub>2</sub>/biochar due to the evaporation of moisture contents. Meanwhile, ZnO/biochar and Fe<sub>2</sub>O<sub>3</sub>/biochar show a significant weight loss of around 20 % due to the accumulation of water during the co-precipitation synthesis process.

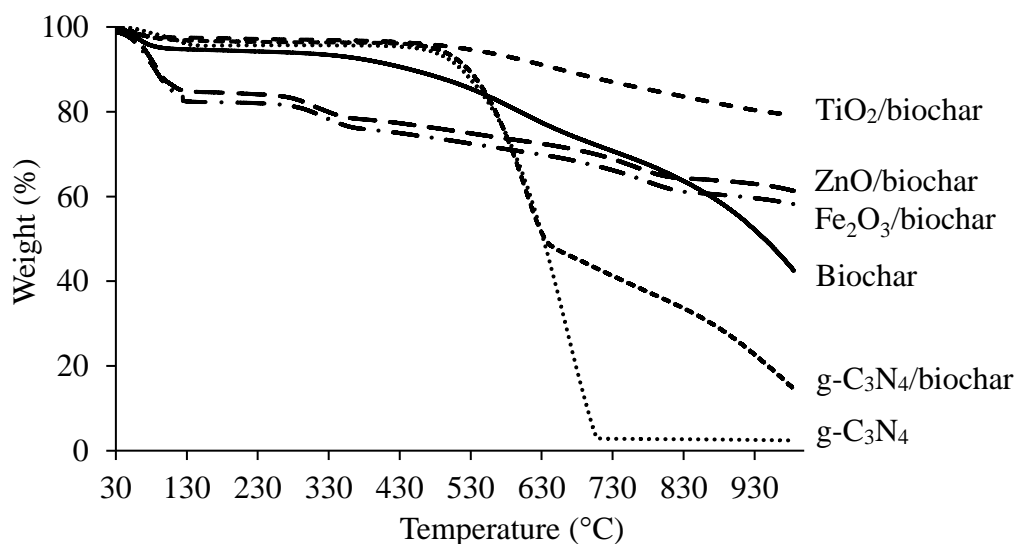


Figure 4.4: TGA Plot of Different Catalyst

Biochar decomposition process started at 350 °C and the residual ash content was around 42 % at 1000 °C. Both the g-C<sub>3</sub>N<sub>4</sub> and g-C<sub>3</sub>N<sub>4</sub>/biochar started to decompose at 500 °C, with a similar decomposing rate within heating temperature of 500 °C to 650 °C. g-C<sub>3</sub>N<sub>4</sub> was completely decomposed at 700 °C with a total weight loss of 98 %, while g-C<sub>3</sub>N<sub>4</sub>/biochar had a residual ash content of 15 % when the heating temperature reached 1000 °C. These results suggested that biochar could improve the thermal stability of g-C<sub>3</sub>N<sub>4</sub>.

Besides, the total weight loss of TiO<sub>2</sub>/biochar was 20 %, which was the lowest among other composite materials. This might be related to the high purity and high thermal stability of TiO<sub>2</sub>/biochar, without a significant amount of water and organics that were attached on the surface of the sample (Saja and Haider, 2016). Meanwhile, ZnO/biochar and Fe<sub>2</sub>O<sub>3</sub>/biochar started to decompose at a relatively low temperature of 300 °C and their total weight losses at 1000 °C were 39 % and 42 %, respectively.

#### 4.1.5 Surface Area Analysis

Table 4.2 shows the specific surface area, average pore volume and average pore diameter of biochar, g-C<sub>3</sub>N<sub>4</sub>, g-C<sub>3</sub>N<sub>4</sub>/biochar and other metal oxides/biochar. The specific surface area and average pore volume of all the composite materials were significantly higher than the biochar. Generally, the large specific surface area could facilitate the adsorption of dye molecules and provide more catalytic active sites for the photocatalytic activity to take place. According to the IUPAC classification, the pore diameter of all the catalyst samples belonged to the mesopore group ( 2 – 50 nm).

Table 4.2: Surface Area Analysis Results of Different Catalyst

Sample	Specific Surface Area (m <sup>2</sup> /g)	Average Pore Volume (x 10 <sup>-3</sup> cm <sup>3</sup> /g)	Average Pore Diameter (nm)
Biochar	1.224	3.025	9.900
g-C <sub>3</sub> N <sub>4</sub>	2.074	2.543	4.906
g-C <sub>3</sub> N <sub>4</sub> /biochar	5.242	11.26	8.591
TiO <sub>2</sub> /biochar	183.1	173.5	3.790
ZnO/biochar	158.6	162.8	4.108
Fe <sub>2</sub> O <sub>3</sub> /biochar	5.222	17.28	13.23

The specific surface area of coconut shell-derived biochar was as low as  $1.224 \text{ m}^2/\text{g}$ , which was slightly lower than the pure  $\text{g-C}_3\text{N}_4$  ( $2.075 \text{ m}^2/\text{g}$ ). When the biochar and  $\text{g-C}_3\text{N}_4$  combined, the surface area of composite material increased moderately ( $5.242 \text{ m}^2/\text{g}$ ). It was suggested that the presence of biochar skeleton could prevent excessive accumulation of  $\text{g-C}_3\text{N}_4$  to obtain a higher specific surface area (Li, et al., 2019). Besides, the specific surface area of  $\text{TiO}_2/\text{biochar}$  and  $\text{ZnO}/\text{biochar}$  reached as high as  $183.1 \text{ m}^2/\text{g}$  and  $158.6 \text{ m}^2/\text{g}$ , respectively. These results were probably caused by the small grain size of the metal oxides that were synthesized using their common synthesis method (Kim and Kan, 2016; Farahmandjou and Jurablu, 2014). However, the catalytic activities of  $\text{TiO}_2/\text{biochar}$  and  $\text{ZnO}/\text{biochar}$  were not only affected by the specific surface area, other properties such as average pore diameter, pore volume, surface morphology, crystallinity, band gap energy, functional group and thermal stability would determine the catalytic activity too.

Figure 4.5 shows the nitrogen adsorption-desorption isotherms of catalyst samples. All of the catalyst samples exhibited a typical type IV isotherm according to the IUPAC classification, which indicated a predominantly mesoporous structure. The isotherms of biochar,  $\text{g-C}_3\text{N}_4$ ,  $\text{g-C}_3\text{N}_4/\text{biochar}$  and  $\text{Fe}_2\text{O}_3/\text{biochar}$  show a type of H1 hysteresis loop, which is a typical character of porous material with cylindrical pores (Peng, et al., 2020). Meanwhile,  $\text{TiO}_2/\text{biochar}$  and  $\text{ZnO}/\text{biochar}$  show a H3 hysteresis loop, indicated a slit-shaped pore structure with a degree of disorder (Silvestri, et al., 2019).

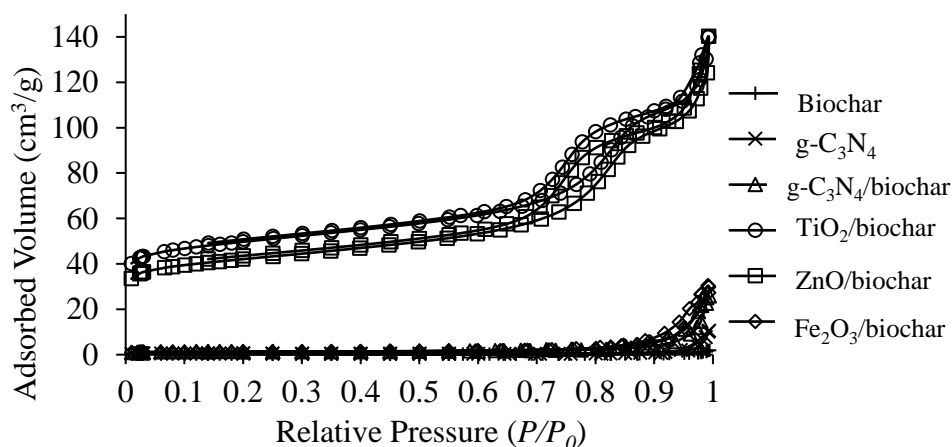


Figure 4.5: Nitrogen Adsorption-Desorption Isotherms on the Surface of Different Catalyst

The pore size distribution of catalyst samples are presented in Figure 4.6. It can be observed that the pore size distribution of  $\text{TiO}_2/\text{biochar}$  and  $\text{ZnO}/\text{biochar}$  were much narrow, which indicated that both of the catalyst samples had much homogeneous pores (Peng, et al., 2020).

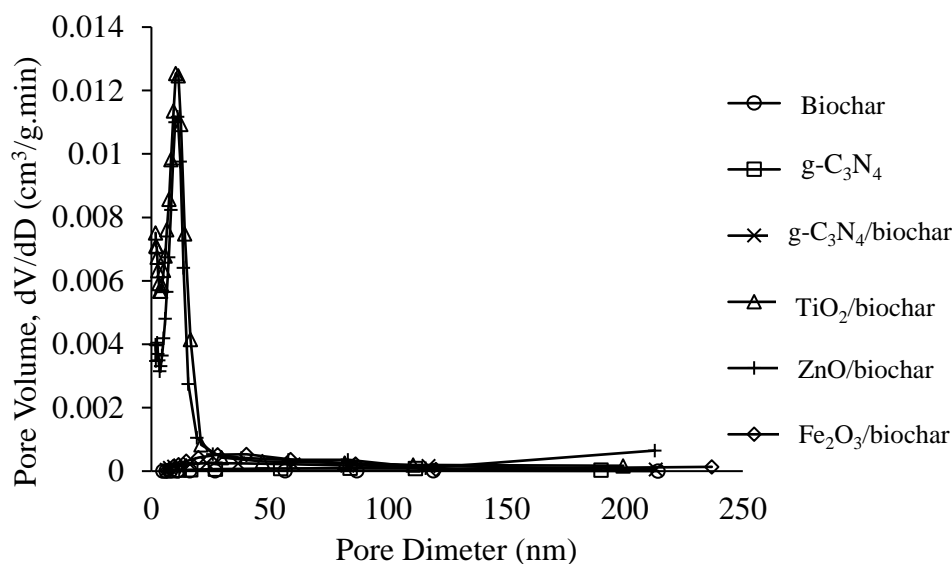


Figure 4.6: Pore Size Distribution of Biochar,  $\text{g-C}_3\text{N}_4$ ,  $\text{g-C}_3\text{N}_4/\text{biochar}$ ,  $\text{TiO}_2/\text{biochar}$ ,  $\text{ZnO}/\text{biochar}$  and  $\text{Fe}_2\text{O}_3/\text{biochar}$

#### 4.1.6 UV-Vis Diffuse Reflectance Spectroscopy (DRS)

Figure 4.7 shows the absorbance spectra of  $\text{g-C}_3\text{N}_4$ ,  $\text{g-C}_3\text{N}_4/\text{biochar}$ ,  $\text{TiO}_2/\text{biochar}$ ,  $\text{ZnO}/\text{biochar}$  and  $\text{Fe}_2\text{O}_3/\text{biochar}$ . The absorption edge of pure  $\text{g-C}_3\text{N}_4$  was around 400 nm. After the incorporation of low reflectivity biochar,  $\text{g-C}_3\text{N}_4/\text{biochar}$  shows stronger absorption in the entire wavelength range, especially a higher absorbance in the visible light region, indicated that the incorporation of biochar significantly improved the optical absorption of the composite material (Li, et al., 2019). Typically,  $\text{TiO}_2$  and  $\text{ZnO}$  would show high absorbance in the UV region of wavelength lower than 400 nm and low absorbance in the visible region. Hence, for the synthesized  $\text{TiO}_2/\text{biochar}$  and  $\text{ZnO}/\text{biochar}$ , the absorption at the UV region confirms the presence of metal oxides, while the absorption in the visible range could be attributed by the biochar content (Fazal, et al., 2019).  $\text{Fe}_2\text{O}_3/\text{biochar}$  shows a strong absorption in the UV range of 300 – 400 nm and a weak absorption at 400 – 800 nm of the visible region, which was in good agreement with the spectrum of  $\alpha\text{-Fe}_2\text{O}_3$

characterized by Kamali, et al. (2014), this confirmed the presence of  $\alpha$ - $\text{Fe}_2\text{O}_3$  in the composite material.

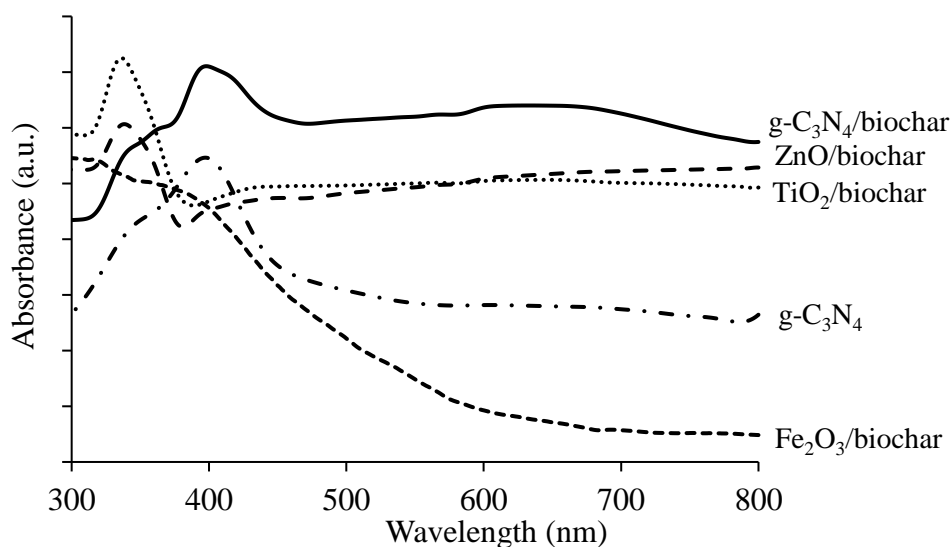


Figure 4.7: Absorbance Spectra of  $g\text{-C}_3\text{N}_4$ ,  $g\text{-C}_3\text{N}_4/\text{biochar}$ ,  $\text{TiO}_2/\text{biochar}$ ,  $\text{ZnO}/\text{biochar}$  and  $\text{Fe}_2\text{O}_3/\text{biochar}$

By using Tauc's relationship, a graph of  $(h\nu F(R))^{1/2}$  versus photon energy was plotted and a tangent line was drawn to obtain the band gap energy of catalyst. As shown in Figure 4.8, the indirect band gap energies of  $g\text{-C}_3\text{N}_4$ ,  $g\text{-C}_3\text{N}_4/\text{biochar}$ ,  $\text{TiO}_2/\text{biochar}$ ,  $\text{ZnO}/\text{biochar}$  and  $\text{Fe}_2\text{O}_3/\text{biochar}$  were found to be 2.7 eV, 2.47 eV, 3.17 eV, 3.02 eV and 2.11 eV, respectively. The band gap energies of all the synthesized metal oxides/biochar were slightly lower than the pure metal oxides, where the typical band gap energies of  $\text{TiO}_2$ ,  $\text{ZnO}$  and  $\text{Fe}_2\text{O}_3$  are 3.2 eV, 3.3 eV and 2.2 eV, respectively (Lu, et al., 2019; Das, Nikhil and Nair, 2019; Mallick and Dash, 2013). According to Li, et al. (2019), the incorporation of biochar skeleton could facilitate a photocatalyst to capture more visible light and adjust its optical properties through the electronic excitation process. Furthermore, it was reported that the incorporation of semiconductors with a carbon matrix could create vacancies, which led to band gap narrowing (Gholami, et al., 2019). Since the band gap energy of  $g\text{-C}_3\text{N}_4/\text{biochar}$  was significantly lower than the pure  $g\text{-C}_3\text{N}_4$ , the composite material was expected to exhibit better photocatalytic performance as it could harvest more visible light than the pure  $g\text{-C}_3\text{N}_4$ .

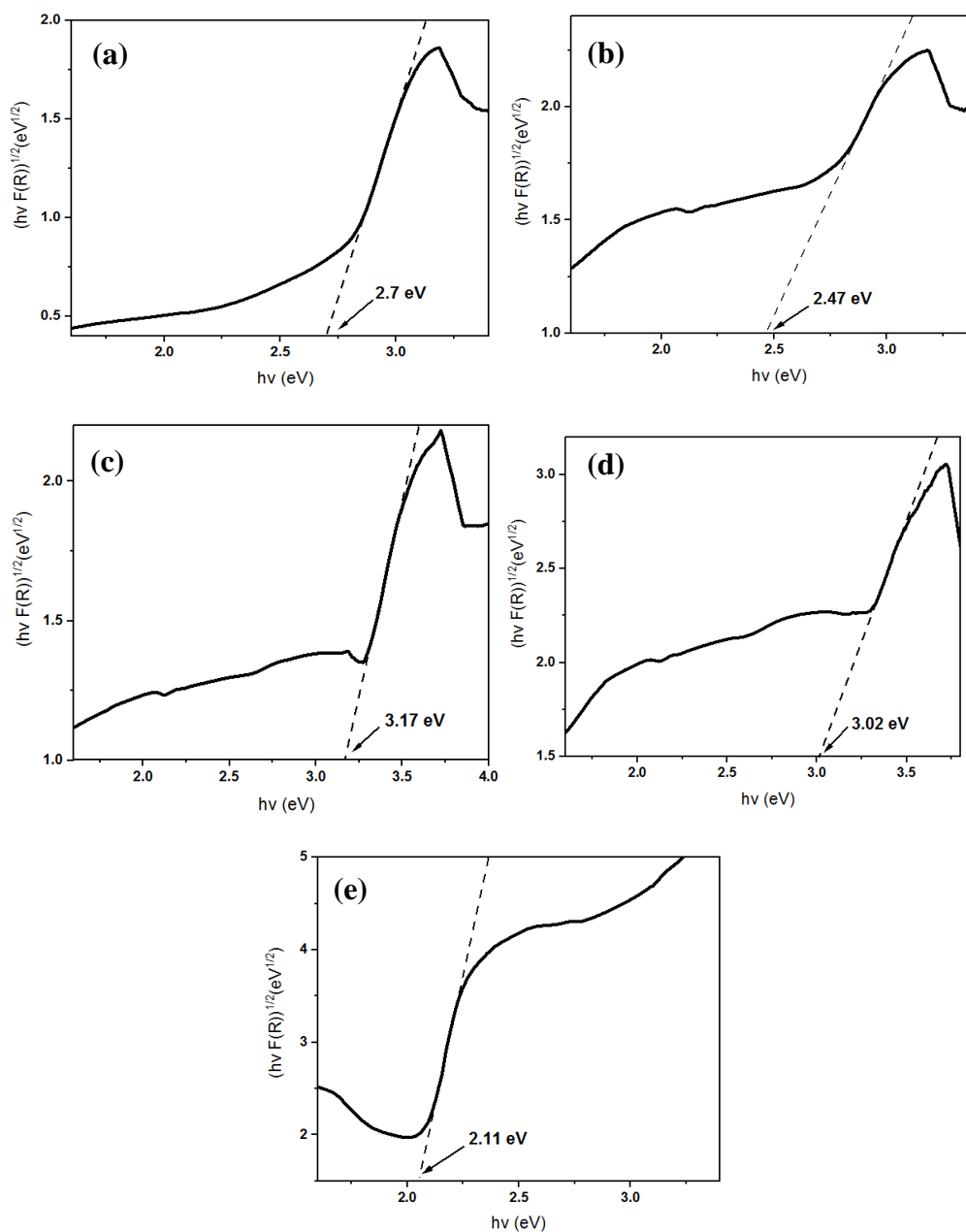


Figure 4.8: Band Gap Energy of (a) g-C<sub>3</sub>N<sub>4</sub>, (b) g-C<sub>3</sub>N<sub>4</sub>/biochar, (c) TiO<sub>2</sub>/biochar, (d) ZnO/biochar and (e) Fe<sub>2</sub>O<sub>3</sub>/biochar

#### 4.1.7 Zeta Potential Analysis

Zeta potential analysis was conducted to investigate the surface charge of biochar, g-C<sub>3</sub>N<sub>4</sub> and g-C<sub>3</sub>N<sub>4</sub>/biochar at different solution pH. Generally, particles exhibit protonation and deprotonation in aqueous suspension, which could be attributed to the interaction between H<sup>+</sup> or OH<sup>-</sup> from the aqueous medium with surface of the particle. Under different solution pH, the extend of these interactions could diverse, thereby resulted in various surface charges and

zeta potential values (Zhu, et al., 2015). The pH value resulting in a zero net charge is called the isoelectric point. Figure 4.9 shows that the isoelectric points of biochar, g-C<sub>3</sub>N<sub>4</sub> and g-C<sub>3</sub>N<sub>4</sub>/biochar are pH 2.2, 4 and 3.7, respectively. Under the strong acidic conditions, all the sample possesses a positively charged surface. According to Xu, et al. (2015), surface with positive charge could promote the adsorption of anionic dye, such as Methyl Orange. Consequently, the good adsorption of dye could facilitate their degradation through the subsequent photocatalysis reaction.

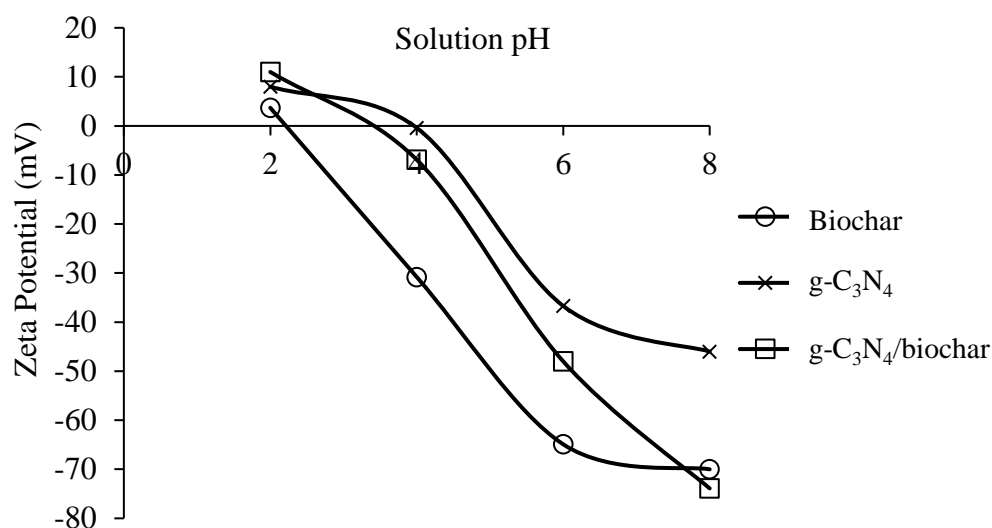


Figure 4.9: Zeta Potential of Biochar, g-C<sub>3</sub>N<sub>4</sub> and g-C<sub>3</sub>N<sub>4</sub>/biochar

To examine the stability of the particles, generally, the higher the zeta potential value (+/-), the more stable the particles are. A large value of zeta potential indicates a good physical stability of particles due to the electrostatic repulsion between individual particles. When the zeta potential value is low, particles could aggregate and flocculate due to Van der Waals forces and hydrophobic interaction, which then resulted in physical instability (Joseph and Singhvi, 2019). This indicated that g-C<sub>3</sub>N<sub>4</sub>/biochar was the most stable catalyst under the strong acidic condition of pH 2 due to the highest value of zeta potential (+11 mV). Furthermore, g-C<sub>3</sub>N<sub>4</sub> was the least stable particles within a pH range of 4 to 8. The stability of this composite material improved significantly as compared to the pure g-C<sub>3</sub>N<sub>4</sub>, especially under pH condition of 8, where the zeta potential improved from -46 mV to -73.9 mV.

## 4.2 Parameter Studies

Several parameter studies were conducted to study the photocatalytic degradation of Methyl Orange under different operating conditions. These included effect of different types of catalyst, effect of different types of oxidant, effect of catalyst dosage, effect of oxidant dosage and solution pH.

### 4.2.1 Effect of Different Types of Catalyst

The effect of a various catalyst on the photocatalytic degradation of Methyl Orange was studied and the results are shown in Figure 4.10. It was found that g-C<sub>3</sub>N<sub>4</sub>/biochar demonstrated the highest degradation efficiency of Methyl Orange among all the pure and composite materials. This was mainly due to the narrow band gap energy of g-C<sub>3</sub>N<sub>4</sub>/biochar (2.47 eV), which enables it to be excited in the visible light region for the production of electron-hole pairs, leading to the generation of •OH. This highly reactive radical would mineralize organic dye, contributing to the degradation of the dye solution.

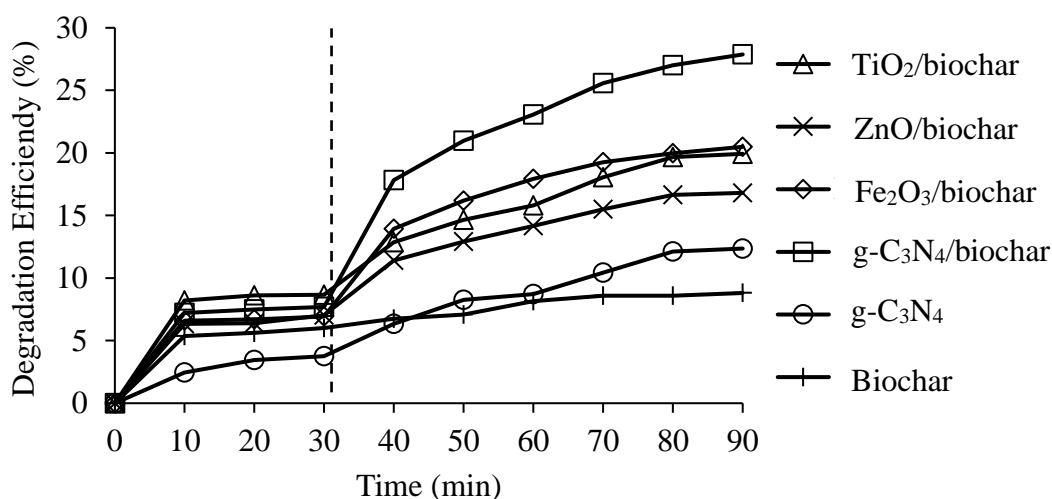


Figure 4.10: Effect of Different Catalyst on the Photocatalytic Degradation of Methyl Orange (Catalyst Dosage = 1 g/L, Natural Solution pH)

Fe<sub>2</sub>O<sub>3</sub>/biochar provided the second highest photocatalytic activity, owing to its low band gap energy (2.11 eV). However, the photocatalytic activity of Fe<sub>2</sub>O<sub>3</sub>/biochar was significantly lower than the g-C<sub>3</sub>N<sub>4</sub>/biochar, even though possesses narrower band gap energy. According to Mishra and Chun (2015), the photocatalytic activity of Fe<sub>2</sub>O<sub>3</sub> was usually limited due to its high

recombination rate of electron-hole pairs. On the other hand, TiO<sub>2</sub>/biochar and ZnO/biochar had the lowest photocatalytic efficiency of Methyl Orange among other composite materials. The large band gap energies of TiO<sub>2</sub> (3.17 eV) and ZnO (3.02 eV) restricted the utilization of visible light spectrum for the excitation process, thus affected the production of •OH for the photocatalytic degradation of organic dye.

Typically, biochar is a good adsorbent, but it did not possess photocatalytic activity. Meanwhile, g-C<sub>3</sub>N<sub>4</sub> possessed lower photocatalytic activity as compared to g-C<sub>3</sub>N<sub>4</sub>/biochar, which might due to its wider band gap energy (2.7 eV), low surface area, weak visible light absorption and high recombination rate of electron-hole pairs (Xie and Li, 2016). According to Li, et al. (2019), the intimate interface between g-C<sub>3</sub>N<sub>4</sub> and amorphous carbon in biochar could accelerate the charge transfer kinetics and prolong the charge carrier lifetime. Besides, the carbon rich material could serve as an electron collector and transporter in a composite material, which could delay the recombination rate of electron-hole pairs. The large surface area of composite material could also provide more catalytic active sites for the photocatalytic activity to take place (Li, et al., 2019).

#### **4.2.2 Effect of Different Types of Oxidant**

The effect of adding several oxidizing agents, including H<sub>2</sub>O<sub>2</sub>, PS and PMS in photocatalytic degradation of Methyl Orange were investigated and the results are shown in Figure 4.11. The photocatalytic degradation efficiency of Methyl Orange in the presence of H<sub>2</sub>O<sub>2</sub>, PS and PMS could achieve 39 %, 60 % and 89 %, respectively.

In these oxidation processes, •OH and SO<sub>4</sub>•<sup>-</sup> played an important role in oxidizing organic dye molecules. These oxidizing agents would be activated under visible light irradiation, leading to the generation of •OH and SO<sub>4</sub>•<sup>-</sup>, as illustrated in Equations (4.1), (4.2) and (4.3), respectively. In the case of PS and PMS, part of the SO<sub>4</sub>•<sup>-</sup> produced would further react with water molecules to produce •OH, as shown in Equation (4.4) (Saien and Solyemani, 2014). The coexistent of both oxidative radicals in the PS and PMS systems contributed to a high degradation efficiency of dye. The photocatalytic degradation efficiency of organic dye in the presence of H<sub>2</sub>O<sub>2</sub> was significantly lower than other

oxidants since only  $\bullet\text{OH}$  are involved in the reaction. Jiang, Qiu and Sun (2018) reported that the lifetime of  $\bullet\text{OH}$  was merely around 20 ns, which limited its reactivity time with the organic pollutants. Thus,  $\text{SO}_4\bullet^-$  with a longer half-life of 40  $\mu\text{s}$  was recently more attractive to be utilized for the oxidative degradation of organic dye.

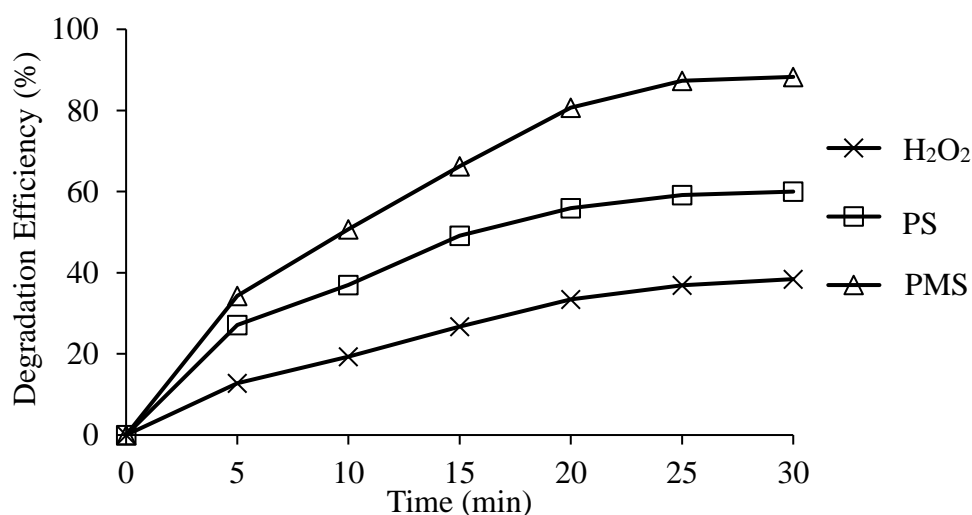
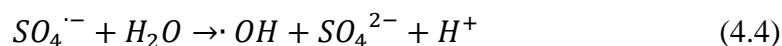


Figure 4.11: Effect of Different Oxidant on the Photocatalytic Degradation of Methyl Orange (Catalyst Dosage = 1 g/L, Oxidant Dosage = 1 mM, Natural Solution pH = 6.5)

#### 4.2.3 Effect of Catalyst Dosage

Figure 4.12 shows the effect of catalyst dosage on the photocatalytic degradation of Methyl Orange. It could be seen that the degradation efficiency was initially directly proportional to the catalyst dosage, as the degradation efficiencies were 58 %, 68 %, 74 % and 87 % at a catalyst dosage of 0, 0.25, 0.50 and 0.75 g/L, respectively. When catalyst dosage raised beyond 0.75 g/L, the photocatalytic degradation efficiency of Methyl Orange shows a negligible change.

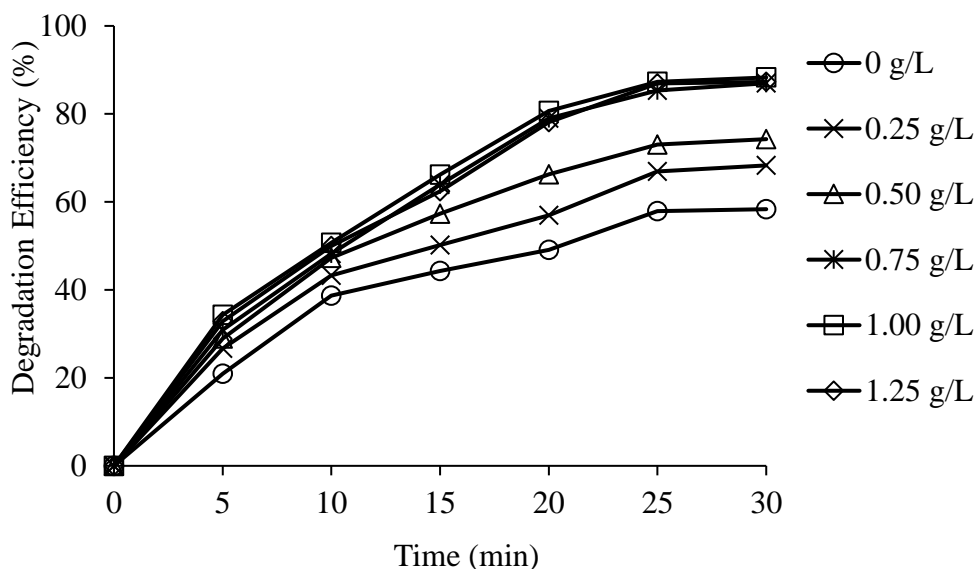


Figure 4.12: Effect of Catalyst Dosage on the Photocatalytic Degradation of Methyl Orange (Oxidant Dosage = 1 mM, Natural Solution pH = 6.5)

In the absence of catalyst, the degradation efficiency of Methyl Orange was only contributed by photolysis and the oxidant. The degradation efficiency increased from 68 % up to a stagnant level of around 87 % when catalyst dosage raised from 0.25 g/L to 0.75 g/L. This improvement was attributed to the increment in the availability of catalytic active sites, which in turn enhanced the generation of  $\bullet\text{OH}$  and promoted the photocatalytic reaction (Khataee, et al., 2017).

However, the degradation efficiency of Methyl Orange showed insignificant changes of around 1 % increment when the catalyst dosage increased from 0.75 g/L to 1.00 g/L. Nevertheless, the degradation efficiency started to decline when the catalyst dosage further increased up to 1.25 g/L. This phenomenon was mainly attributed to the scattering effect (Yu, et al., 2013). As the concentration of catalyst increased upon the optimum level, the high turbidity of catalyst could reduce the penetration depth of visible light irradiation. As the photocatalyst could not be absorbed and activated by light irradiation, the number of oxidative radicals that could be generated would reduce, leading to a low photocatalytic degradation efficiency.

#### 4.2.4 Effect of Oxidant Dosage

Figure 4.13 shows the degradation efficiency improved significantly from 21 % to 86 % when the oxidant dosage increased from 0 mM to 0.6 mM, but the degradation efficiency remained nearly unchanged when the oxidant dosage further increased up to 1.0 mM. Generally, increasing oxidant dosage would increase the generation of  $\cdot\text{OH}$  and  $\text{SO}_4\cdot^-$ , which will in turn improve the degradation efficiency of Methyl Orange. Exceeding the optimum amount of oxidant, the reduction in degradation efficiency could be observed due to a scavenging effect from the excessive oxidant. As presented in Equations (4.5) and (4.6), an excessive amount of PMS would lead to a side reaction, where the oxidative radicals would react with excess  $\text{HSO}_5^-$  to produce  $\text{SO}_5\cdot^-$ .  $\text{SO}_5\cdot^-$  is a weaker oxidizing agent when compared to the desired  $\cdot\text{OH}$  and  $\text{SO}_4\cdot^-$  and thus contributed to the decrement in degradation efficiency (Jiang, Qiu and Sun, 2018).

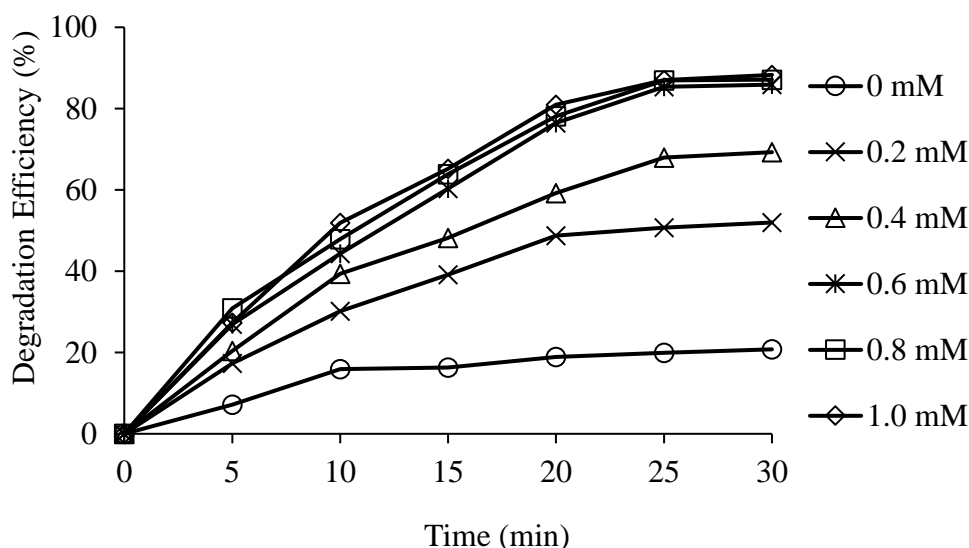
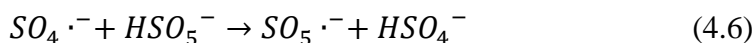
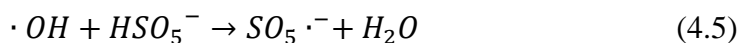


Figure 4.13: Effect of Oxidant Dosage on the Photocatalytic Degradation of Methyl Orange (Catalyst Dosage = 0.75 g/L, Natural Solution pH = 6.5)

#### 4.2.5 Effect of Solution pH

Figure 4.14 shows that the optimum solution pH for the photocatalytic degradation of Methyl Orange occurred at the acidic condition as the degradation efficiency increased linearly when solution pH decreased from pH 11 to pH 3. The increase in degradation efficiency with a decrease in pH could be explained by the surface charge of g-C<sub>3</sub>N<sub>4</sub>/biochar and the structural change of Methyl Orange.

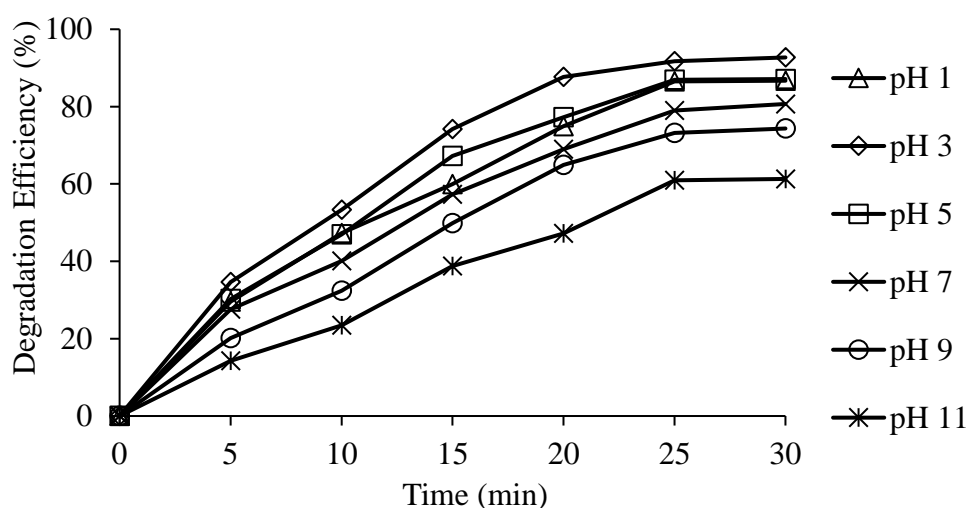


Figure 4.14: Effect of Solution pH on the Photocatalytic Degradation of Methyl Orange (Catalyst Dosage = 0.75 g/L, Oxidant Dosage = 0.6 mM)

Generally, a catalyst would be protonated and become positively charged when they react with H<sup>+</sup> under acidic conditions, while in alkaline conditions, the catalyst would become negatively charged as they react with OH<sup>-</sup> (Kumar and Pandey, 2017). Since Methyl Orange is an anionic dye with the negative charge on its surface, positively charged catalyst under acidic condition would improve the adsorption and therefore enhance the subsequent degradation of the anionic dye. Meanwhile, the catalyst experienced low adsorption at alkaline conditions due to the repulsive electrostatic force existed between the catalyst and organic dye (Xu, et al., 2015). Another possible reason for effective photocatalytic degradation under acidic conditions was the structural change of Methyl Orange from azo to quinoid at low pH (Niu, 2013). The quinoid structure has lower bond energy, which is easier to be decomposed as compared to the azo structure.

### 4.3 Optimization Studies

In the previous parameter studies, three parameters, catalyst dosage ( $X_1$ ), oxidant dosage ( $X_2$ ) and solution pH ( $X_3$ ) were considered. Consequently,  $X_1$ ,  $X_2$  and  $X_3$  were selected as the independent variables while the photocatalytic degradation efficiency of Methyl Orange ( $Y$ ) was chosen as the response of the study. CCD model was used to examine the interactive relationship between the participating parameters and between parameters and the response.

#### 4.3.1 Regression Analysis

As shown in Table 4.3, the photocatalytic degradation efficiency of Methyl Orange ranged from 43.82 % to 94.39 % in response to the variation in the experimental condition. The model obtained for degradation efficiency of Methyl Orange with significant terms was quadratic as suggested by software and their empirical relations could be explained using Equation (4.7). Positive and negative coefficient indicated the positively and negatively individual effect towards the Methyl Orange degradation, respectively.

$$Y = 87.29 + 2.70X_1 + 14.32X_2 - 7.11X_3 - 0.1950X_1X_2 - 0.8475X_1X_3 - 0.6275X_2X_3 - 4.51X_1^2 - 6.80X_2^2 - 7.94X_3^2 \quad (4.7)$$

The accuracy of the model was justified by ANOVA and the results are presented in Table 4.4. The model  $F$ -value of 994.03 implied that the model developed was significant and there was only 0.01 % of the chance that the  $F$ -value could occur due to noise. On the other hand,  $P$ -value is the probability of  $F$ -value and was used to test the null hypothesis. Generally, parameters having  $P$ -value less than 0.05 were said to be significant. In this case,  $X_1$ ,  $X_2$ ,  $X_3$ ,  $X_1X_2$ ,  $X_1X_3$ ,  $X_2X_3$ ,  $X_1^2$ ,  $X_2^2$  and  $X_3^2$  were significant. Therefore, this analysis confirmed the significance of all the individual variables and interaction terms in the photodegradation of Methyl Orange. Furthermore, the lack of fit  $F$ -value of 2.55 indicated that the lack of fit was not significant relative to the pure error. The non-significant lack of fit indicated good predictability of the model and there was only a 16.42 % chance that the lack of fit  $F$ -value could occur due to noise.

Table 4.3: Experimental Results for the Three Independent Variables

Standard Order	Point Type	Coded Independent Variable Levels			Degradation Efficiency (%)	
		Catalyst Dosage, g/L ( $X_1$ )	Oxidant Dosage, mM ( $X_2$ )	Solution pH ( $X_3$ )	Experimental Values	Predicted Values
1	Factorial	0.25 (-1)	0.2 (-1)	3.0 (-1)	57.34	56.47
2	Factorial	0.75 (+1)	0.2 (-1)	3.0 (-1)	64.01	63.95
3	Factorial	0.25 (-1)	0.6 (+1)	3.0 (-1)	86.72	86.75
4	Factorial	0.75 (+1)	0.6 (+1)	3.0 (-1)	94.39	93.45
5	Factorial	0.25 (-1)	0.2 (-1)	7.0 (+1)	44.49	45.20
6	Factorial	0.75 (+1)	0.2 (-1)	7.0 (+1)	49.55	49.29
7	Factorial	0.25 (-1)	0.6 (+1)	7.0 (+1)	73.14	72.97
8	Factorial	0.75 (+1)	0.6 (+1)	7.0 (+1)	75.64	76.28
9	Axial	0.08 (-1.68)	0.4 (0)	5.0 (0)	69.93	69.99
10	Axial	0.92 (+1.68)	0.4 (0)	5.0 (0)	78.81	79.06
11	Axial	0.5 (0)	0.06 (-1.68)	5.0 (0)	43.82	43.99

Standard Order	Point Type	Coded Independent Variable Levels			Degradation Efficiency (%)	
		Catalyst Dosage, g/L ( $X_1$ )	Oxidant Dosage, mM ( $X_2$ )	Solution pH ( $X_3$ )	Experimental Values	Predicted Values
12	Axial	0.5 (0)	0.74 (+1.68)	5.0 (0)	92.00	92.15
13	Axial	0.5 (0)	0.4 (0)	1.64 (-1.68)	75.83	76.81
14	Axial	0.5 (0)	0.4 (0)	8.36 (+1.68)	53.55	52.89
15	Center	0.5 (0)	0.4 (0)	5.0 (0)	86.81	87.29
16	Center	0.5 (0)	0.4 (0)	5.0 (0)	88.14	87.29
17	Center	0.5 (0)	0.4 (0)	5.0 (0)	86.93	87.29
18	Center	0.5 (0)	0.4 (0)	5.0 (0)	87.23	87.29
19	Center	0.5 (0)	0.4 (0)	5.0 (0)	86.83	87.29
20	Center	0.5 (0)	0.4 (0)	5.0 (0)	87.87	87.29

Table 4.4: ANOVA Results for Photocatalytic Degradation Efficiency of Methyl Orange

<b>Factors</b>	<b>Squares Sum</b>	<b>Freedom Degrees</b>	<b>Square Average</b>	<b>F-value</b>	<b>Probability, P-value</b>	
<b>Quadratic model</b>	5180.05	9	575.56	994.03	< 0.0001	Significant
$X_1$	99.35	1	99.35	171.58	< 0.0001	
$X_2$	2799.44	1	2799.44	4834.82	< 0.0001	
$X_3$	690.53	1	690.53	1192.59	< 0.0001	
$X_1 X_2$	3.04	1	3.04	5.25	0.0485	
$X_1 X_3$	5.75	1	5.75	9.92	0.0103	
$X_2 X_3$	3.15	1	3.15	5.44	0.0419	
$X_1^2$	293.49	1	293.49	506.88	< 0.0001	
$X_2^2$	665.74	1	665.74	1149.78	< 0.0001	
$X_3^2$	907.44	1	907.44	1567.21	< 0.0001	
<b>Residual</b>	5.79	10	0.5790			
<b>Lack of fit</b>	4.16	5	0.8314	2.55	0.1642	Insignificant
<b>Pure error</b>	1.63	5	0.3267			
<b>Corrected total</b>	5185.84	19				

$R^2 = 0.9989$  ; adequate precision = 91.9289

A high value of determination coefficient ( $R^2 = 0.9989$ ) implied that 99.89 % of the total variation for the photocatalytic degradation of Methyl Orange could be described by the suggested model. Besides, the value of the signal to noise ratio (adequate precision) was found to be 91.9289, indicated that the model had an adequate signal. Principally, an adequate precision ratio greater than 4 implied that the developed model could be used to navigate the design space and find the optimum condition of the process.

Figure 4.15 shows the predicted and actual values for the photocatalytic degradation of Methyl Orange. It could be observed that the values calculated using the developed model were in good agreement with the actual experimental values, with a satisfactory correlation between these values. Therefore, the model suggested by the software is suitable for predicting the photocatalytic degradation of Methyl Orange under different operating conditions.

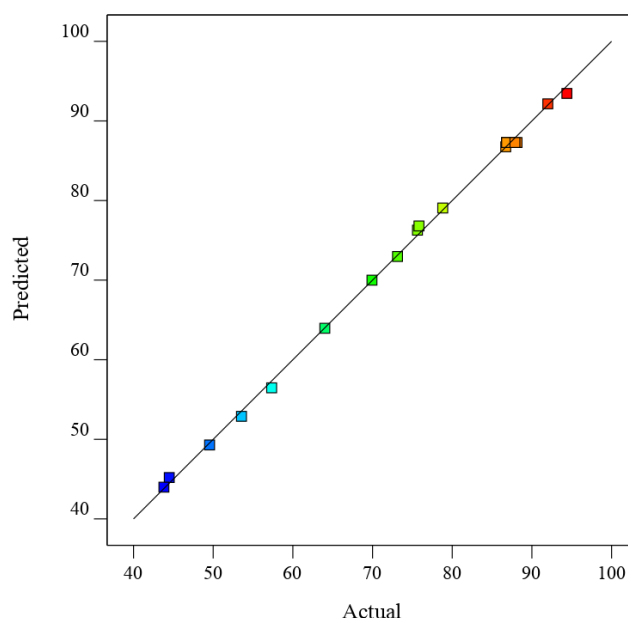


Figure 4.15: Predicted and Actual Values for Photocatalytic Degradation of Methyl Orange ( $R^2 = 0.9989$ )

### 4.3.2 Response Surface Analysis

A comparison of the effects of all three parameters was performed by using perturbation plots as illustrated in Figure 4.16. The perturbation plots can assist to identify the effectiveness of each factor in affecting the removal of Methyl Orange. The steep curvature of catalyst dosage, oxidant dosage and solution pH as denoted by *A*, *B* and *C*, respectively indicated that the photocatalytic degradation of Methyl Orange was highly affected by these three operating parameters. It could be observed that the degradation efficiency increased with increasing catalyst and oxidant dosage but decreasing solution pH, which was in accordance with the results obtained from parameter studies performed previously. The steepest curvature of oxidant dosage implied that it was the most effective parameter in affecting the degradation of Methyl Orange.

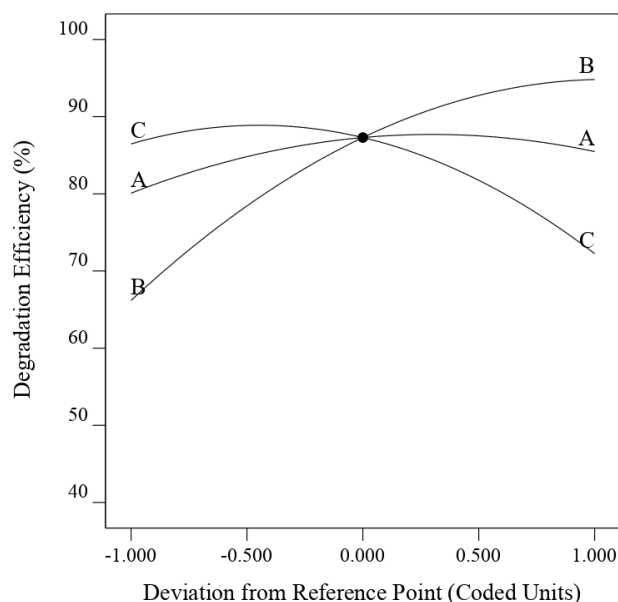


Figure 4.16: Perturbation Plot for Three Factors Study

The response surface plots were displayed to show the influence of independent variables on the photocatalytic degradation of Methyl Orange, as shown in Figure 4.17. The degradation efficiency increased by changing the oxidant dosage from 0.2 to 0.6 mM in a certain catalyst dosage at the fixed value of solution pH 5. This result confirmed the experimental result obtained from the previous parameter study, where the optimum oxidant dosage was found to be 0.6 mM. This was primarily due to the increasing amount of  $\bullet\text{OH}$  and  $\text{SO}_4^{\bullet-}$  as the oxidant dosage increased. Figure 4.17 (a) also shows the increase of catalyst dosage from 0.25 g/L to 0.75 g/L resulted in the increasing degradation efficiency, which was mainly attributed to the availability of catalytic active sites. It was noted that one of the important parameters determining the degradation efficiency of Methyl Orange was oxidant dosage. For example, by comparing run 1 with run 3 and run 1 with run 2, the interaction between these two factors could be observed. The degradation efficiency increased from 57.34 % to 86.72 % when the oxidant dosage increased from 0.2 mM to 0.6 mM under constant catalyst dosage and solution pH. Meanwhile, the degradation efficiency increased slightly from 57.34 % to 64.01 % as the catalyst dosage enhanced from 0.25 g/L to 0.75 g/L under constant oxidant dosage and solution pH. This result showed that oxidant dosage had a greater effect on the degradation of Methyl Orange as compared to the catalyst dosage.

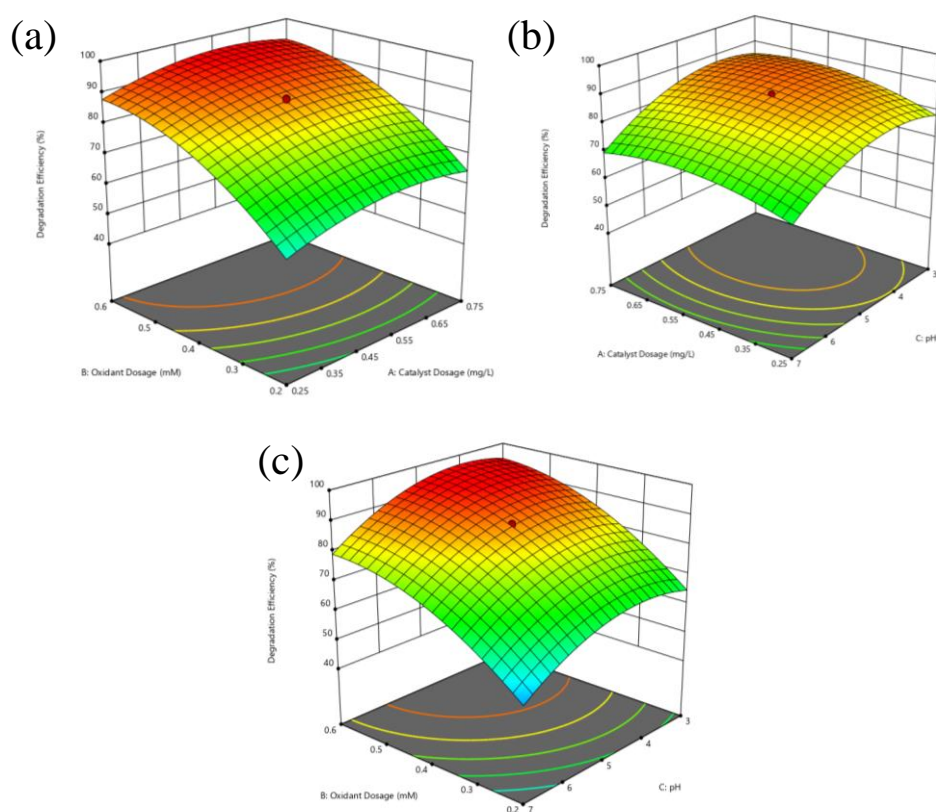


Figure 4.17: Effect of Three Factors on the Photocatalytic Degradation of Methyl Orange at Fixed (a) Solution pH 3 (b) Oxidant Dosage 0.4 mM and (c) Catalyst Dosage 0.5 g/L

The interaction between catalyst dosage and solution pH is shown in Figure 4.17 (b). Generally, photocatalytic degradation efficiency increased when the solution pH decreased within different catalyst dosage range at a fixed oxidant dosage of 0.4 mM. The results aligned to the optimum findings found in the preliminary study, where the photocatalytic degradation of Methyl Orange could be performed effectively under acidic conditions. This could be attributed to the surface charge of photocatalyst as well as the structural change of Methyl Orange under different solution pH. Besides, it was noted that solution pH affected the degradation efficiency slightly greater than the catalyst dosage. According to the result of run 1 and run 5, degradation efficiency increased from 44.49 % to 57.34 % when the solution pH changed from pH 7 to pH 3. Meanwhile, degradation efficiency increased from 86.72 % to 94.39 % when the catalyst dosage increased from 0.25 g/L in run 3 to 0.75 g/L in run 4. Both the independent variables have a subtle effect on the photocatalytic

degradation of Methyl Orange if compared to oxidant dosage. The significance of oxidant dosage was even clearer when observing Figure 4.17 (c), which illustrated the interaction between oxidant dosage and solution pH under constant catalyst dosage.

### 4.3.3 Model Validation and Experimental Confirmation

The model validation and process optimization runs were conducted simultaneously and the results are presented in Table 4.5. DOE software generated a few optimum solutions and the results were arranged according to the order of suitability. The first five solutions of the optimum condition were selected and experiments were conducted based on the parameter combinations. The experimental values obtained from photocatalytic degradation of Methyl Orange were found to be within 5 % accuracy to the predicted values. For instance, the predicted degradation efficiency of 94.86 % was obtained at the catalyst dosage of 0.75 g/L, oxidant dosage of 0.57 mM and solution pH of 3.48, while the experimental value was found to be 96.63 %, with merely 1.8 % of disparity. It was noted that the experimental values obtained were in good agreement with the predicted values. Thus, it could be confirmed that the RSM method was a reliable and effective method for optimizing the photocatalytic degradation of Methyl Orange.

Table 4.5: Experimental and Predicted Results Conducted at Optimized Condition for Model Validation

<b>Runs</b>	<b>X<sub>1</sub></b>	<b>X<sub>2</sub></b>	<b>X<sub>3</sub></b>	<b>Experimental</b>	<b>Predicted</b>
1	0.75	0.57	3.48	96.63	94.86
2	0.63	0.52	3.57	94.27	95.16
3	0.66	0.52	3.88	92.78	95.05
4	0.55	0.54	3.59	93.91	95.89
5	0.53	0.57	4.52	95.71	96.18

#### 4.4 Kinetic Studies

Kinetic studies were performed based on the degradation rate of Methyl Orange to identify the reaction order for photocatalytic degradation of organic dye. Figure 4.18 shows that photocatalytic degradation of Methyl Orange followed the pseudo first order kinetic due to the high determination of coefficient ( $R^2 > 0.95$ ) under different operating temperatures. The reaction kinetic model of photocatalytic degradation of dye is presented in Equation (4.8). Gholami, et al. (2019) reported that the reaction order of dye degradation could be determined by the concentration of dye at a different time interval. This is mainly due to the short half-life of oxidative radicals ( $\bullet\text{OH}$  and  $\text{SO}_4^{\bullet-}$ ), where their concentration were not likely to be identified and measured, thus considered as constant at a specific time.

$$\ln\left(\frac{C_0}{C_t}\right) = k_{app}t \quad (4.8)$$

Where,

$C_0$  = initial concentration of organic dye (mg/L)

$C_t$  = residual concentration of organic dye at certain time (mg/L)

$k_{app}$  = apparent reaction constant ( $\text{min}^{-1}$ )

$t$  = reaction time (min)

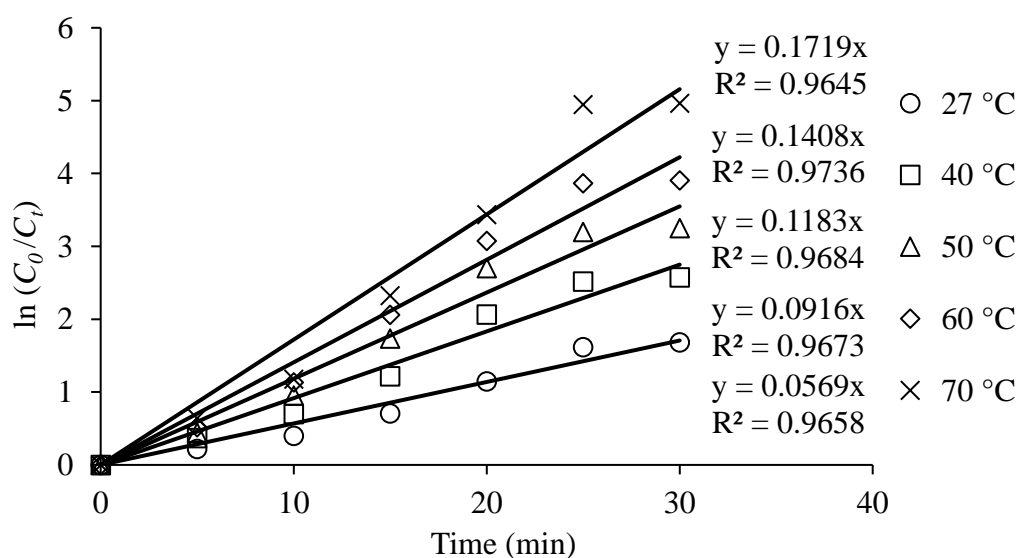


Figure 4.18: Pseudo First Order Reaction Kinetic Plot for Photocatalytic Degradation of Methyl Orange

It could be observed that the apparent rate constant ( $k_{app}$ ) increased greatly from  $0.0569 \text{ min}^{-1}$  to  $0.1719 \text{ min}^{-1}$  over the solution temperature range from  $27 \text{ }^\circ\text{C}$  to  $70 \text{ }^\circ\text{C}$ . Typically, the oxidation rate of organic molecules at the catalyst interface could be enhanced at high operating temperatures (Gnanaprakasam, Sivakumar and Thirumarimurugan, 2015). Table 4.6 further validated the pseudo first kinetic order of photocatalytic degradation of Methyl Orange as the experimental results could not well-fitted to pseudo zero and pseudo second kinetic model, with  $R^2$  lower than 0.90.

Table 4.6: Rate Coefficient for Photocatalytic Degradation of Methyl Orange Under Different Temperature

Temperature ( $^\circ\text{C}$ )	Pseudo Zero Order		Pseudo First Order		Pseudo Second Order	
	$R^2$	$k_{app}$ ( $\frac{\text{mg}}{\text{L.min}}$ )	$R^2$	$k_{app}$ ( $\text{min}^{-1}$ )	$R^2$	$k_{app}$ ( $\frac{\text{L}}{\text{mg.min}}$ )
27	0.9629	0.3071	0.9658	0.0569	0.8628	0.0131
40	0.8565	0.3744	0.9673	0.0916	0.8461	0.0367
50	0.7577	0.4029	0.9684	0.1183	0.8335	0.0746
60	0.6873	0.4161	0.9736	0.1408	0.7769	0.1398
70	0.6269	0.4249	0.9645	0.1719	0.6579	0.3749

The  $k_{app}$  value obtained from different reaction temperatures could be correlated by Arrhenius-type expression as shown in Equation (4.9) to identify the activation energy ( $E_a$ ) and pre-exponential factor ( $A_0$ ) of the reaction model. Figure 4.19 shows a good linear relationship between  $\ln k_{app}$  and  $1/T$ , with  $R^2$  value of 0.9842. Values obtained from the Arrhenius plot were then assigned to the Arrhenius expression and the result is presented in Equation (4.10). The  $E_a$  and  $A_0$  obtained from photocatalytic degradation of Methyl Orange were  $21.64 \text{ kJ/mol}$  and  $352.76 \text{ min}^{-1}$ , respectively. The high value of  $E_a$  suggested that thermal activation is important to accelerate the photocatalytic degradation of organic dye as the photocatalytic action is highly temperature-dependent (Qi, et al., 2010).

$$\ln k_{app} = \ln A_0 - \frac{E_a}{RT} \quad (4.9)$$

$$\ln k_{app} = -2603.2 \left( \frac{1}{T} \right) + 5.8658 \quad (4.10)$$

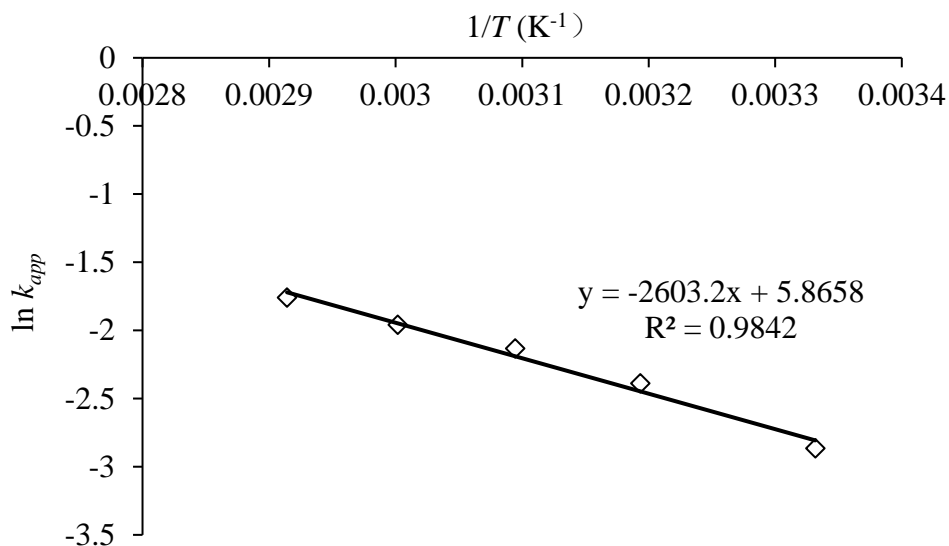


Figure 4.19: Arrhenius Plot of  $\ln k_{app}$  versus  $1/T$

#### 4.5 Chemical Oxygen Demand (COD) Removal

Figure 4.20 shows the COD removal for 30 min pre-adsorption followed by 120 min of photocatalytic degradation of Methyl Orange. The overall COD removal efficiency of Methyl Orange after 2 hours was 67.2 % under the optimum operating condition as determined by RSM (catalyst dosage of 0.75 g/L, PMS oxidant dosage of 0.57 mM and solution pH 3.48). The COD removal efficiency of 67.2 % was significantly lower than the degradation efficiency of 96.63 %.

The reduction in the COD value of dye solution indicates the mineralization of dye molecules into CO<sub>2</sub> and H<sub>2</sub>O. Since the colour of a dye is depending on its chromophore group and not the whole molecule, the decolourization of the dye solution did not imply that the entire dye molecule was successfully converted into CO<sub>2</sub> and H<sub>2</sub>O. Thus, the low COD removal efficiency of 67.2 % could be attributed to the complex structure of Methyl Orange. According to Xie, et al. (2016), the original azo bond in Methyl Orange structure would be destructed and converted into intermediate products of N,N-dimethylbenzenamine (C<sub>8</sub>H<sub>11</sub>N) and N,N-dimethyl-p-phenylenediamine (C<sub>8</sub>H<sub>12</sub>N<sub>2</sub>) during the degradation process, led to its decolourization. It was

believed that the intermediate products were too difficult to be oxidized and thus the COD level remained high. If further oxidized Methyl Orange, the intermediate products would further convert into sulfanilic acid ( $C_6H_6NSO_3$ ),  $CO_2$  and  $H_2O$  (Xie, et al., 2016).

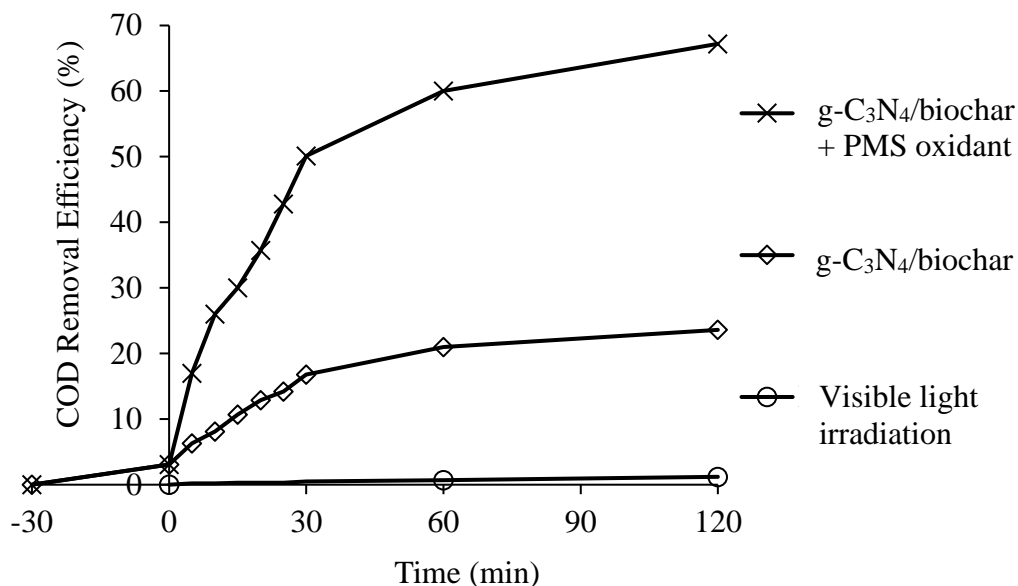


Figure 4.20: COD Removal Efficiencies of Methyl Orange (Adsorption = -30 to 0 min ; Degradation = 0 to 120 min)

Without the addition of PMS oxidant, the COD removal efficiency of Methyl Orange using g-C<sub>3</sub>N<sub>4</sub>/biochar was 23.6 %. Besides, in the absence of photocatalyst and oxidant, the COD removal efficiency of Methyl Orange under visible light irradiation was merely 1.2 %. This indicated that the PMS oxidant and catalyst played important roles during the photocatalytic degradation of Methyl Orange.

## CHAPTER 5

### CONCLUSIONS AND RECOMMENDATIONS

#### 5.1 Conclusions

In this study, various biochar-based photocatalysts were prepared using sol-gel and co-precipitation methods. The characterization and photocatalytic abilities of coconut shell-derived biochar, g-C<sub>3</sub>N<sub>4</sub>, g-C<sub>3</sub>N<sub>4</sub>/biochar, TiO<sub>2</sub>/biochar, ZnO/biochar and Fe<sub>2</sub>O<sub>3</sub>/biochar were investigated. All the samples were characterized by SEM-EDX, XRD, FTIR, TGA, surface area analyses and UV-Vis DRS. SEM results depicted that biochar derived from coconut shell had a porous structure with plenty of meso and macropores. The images also showed the morphological change of biochar after incorporation with g-C<sub>3</sub>N<sub>4</sub> and metal oxides. The XRD and FTIR results indicated that all the characteristic peaks of metal oxides and g-C<sub>3</sub>N<sub>4</sub> could be found in their respective composite materials, which suggested that the catalysts were well incorporated on the biochar. Besides, TGA results proved that biochar could improve thermal stability of g-C<sub>3</sub>N<sub>4</sub>. The surface area analysis results showed that biochar could increase the specific surface area and average pore volume of catalyst sample. According to the result of UV-Vis DRS, band gap energies of g-C<sub>3</sub>N<sub>4</sub>, g-C<sub>3</sub>N<sub>4</sub>/biochar, TiO<sub>2</sub>/biochar, ZnO/biochar and Fe<sub>2</sub>O<sub>3</sub>/biochar were found to be 2.7 eV, 2.47 eV, 3.17 eV, 3.02 eV and 2.11 eV, respectively. Furthermore, zeta potential analysis proved that biochar, g-C<sub>3</sub>N<sub>4</sub> and g-C<sub>3</sub>N<sub>4</sub>/biochar presented positively and negatively charged surface under acidic and alkaline condition, respectively.

The effect of various parameters on the photocatalytic degradation of Methyl Orange had been studied. g-C<sub>3</sub>N<sub>4</sub>/biochar was found to be the most effective photocatalyst as compared to other composite materials, mainly attributed to its low band gap energy. Besides, PMS was the best oxidant in enhancing the degradation of Methyl Orange. The optimum condition for photocatalytic degradation of Methyl Orange was identified at g-C<sub>3</sub>N<sub>4</sub>/biochar composite dosage of 0.75 g/L, PMS oxidant dosage of 0.6 mM and solution pH 3 to achieve 92.71 % degradation efficiency after 30 minutes. The optimum condition was further validated by using RSM, where the highest photocatalytic degradation efficiency (96.63 %) could be obtained at catalyst dosage of 0.75

g/L, PMS oxidant dosage of 0.57 mM and solution pH 3.48. The interactions between parameters were also studied and it could be concluded that oxidant dosage had a major effect on the photocatalytic degradation of Methyl Orange as compared to catalyst dosage and solution pH.

Photocatalytic degradation of Methyl Orange using g-C<sub>3</sub>N<sub>4</sub>/biochar was found to have follow the pseudo first order kinetic due to the high determination of coefficient ( $R^2 > 0.95$ ) under different operating temperatures. Under the optimum operating condition as determined by RSM, the overall COD removal efficiency was 67.2 %. In conclusion, this study was conducted to provide basic information as to the possibility of biochar composites in photocatalytic degradation of organic dye. The overall results suggested that g-C<sub>3</sub>N<sub>4</sub>/biochar can be used for the photocatalytic degradation of Methyl Orange. The utilization of biochar in wastewater treatment is a viable waste management option and coconut shell seems like a suitable feedstock that could be provided in great quantities.

## **5.2 Recommendations for future work**

Inductively coupled plasma – optical emission spectroscopy (ICP-OES) analysis could be carried out to determine the stability of photocatalyst. Meanwhile, different biomass source could be used to replace coconut shell in order to identify the optimum biochar in assisting photocatalytic degradation of Methyl Orange. Besides, g-C<sub>3</sub>N<sub>4</sub>/biochar with different weight percentage of g-C<sub>3</sub>N<sub>4</sub> and biochar should be synthesized to study their respective photocatalytic degradation ability in order to determine the optimum weight percentage.

## REFERENCES

- Adegoke, K. A. and Bello, O. S., 2015. Dye sequestration using agricultural wastes as adsorbents. *Water Resources and Industry*, 12, pp. 8–24.
- Agamuthu, P., Khidzir, K. M. and Fauziah, S. H., 2009. Drivers of sustainable waste management in Asia. *Waste Management Research*, 27, pp. 625-633.
- Aghdasinia, H., Vahid, B., Arehjani, P. and Khataee, A., 2017. Optimization of a textile dye degradation in a recirculating fluidized-bed reactor using magnetite/S<sub>2</sub>O<sub>8</sub><sup>2-</sup> process. *Environmental Technology*, 38(19), pp. 2486-2496.
- Alkaim, A. F., Aljeboree, A. M., Alrazaq, N. A., Baqir, S. J., Hussien, F. H. and Lilo, A. J., 2014. Effect of pH on adsorption and photocatalytic degradation efficiency of different catalysts on removal of methyl blue. *Asian Journal of Chemistry*, 26(24), pp. 8445-8448.
- Ammayappan, L., Jose, S. and Raj, A., 2016. Sustainable production processes in textile dyes. *Green Fashion*, 1, pp. 185-216.
- Angalaeeswari, K. and Kamaldeen, S., 2017. Production and characterization of coconut shell and mesquite wood biochar. *International Journal of Chemical Studies*, 5(4), pp. 442-446.
- Behera, S. K., Meena, H., Chakraborty, S. and Meikap, B. C., 2018. Application of response surface methodology for optimization of leaching parameters for ash reduction from low-grade coal. *International Journal of Mining Science and Technology*, 28, pp. 621-629.
- Borji, S. H., Nasser, S., Mahvi, A. H., Nabizadeh, R. and Javadi, A. H., 2014. Investigation of photocatalytic degradation of phenol by Fe(III)-doped TiO<sub>2</sub> and TiO<sub>2</sub> nanoparticles. *Journal of Environmental Health Science and Engineering*, 12(1), pp.101.
- Bruin, 2015. *Fenton process dye degradation*. [online] Available at: <[https://commons.wikimedia.org/wiki/File:Fenton\\_Process\\_dye\\_degradation.png](https://commons.wikimedia.org/wiki/File:Fenton_Process_dye_degradation.png)> [Accessed 8 June 2019].
- Cagnon, B., Py, X., Guillot, A., Stoeckli, S. and Chambat, G., 2009. Contribution of hemicellulose, cellulose and lignin to the mass and the porous properties of chars and steam activated carbon from various lignocellulosic precursors. *Bioresource Technology*, 100(1), pp. 292-298.
- Cha, J. S., Parl, S. H., Jung, S. C., Ryu, C., Jeon, J. K., Shin, M. C. and Park, Y. K., 2016. Production and utilization of biochar: A review. *Journal of Industrial and Engineering Chemistry*, 40, pp. 1-15.
- Challa, K. ed., 2009. *Magnetic Nanomaterials*. Volume 4. LA: Wiley-VCH.

Chaukura, M., Murimba, E. C. and Gwenzi, W., 2016. Synthesis, characterization and methyl orange adsorption capacity of ferric oxide-biochar nano-composites derived from pulp and paper sludge. *Applied Water Science*, 7, pp. 2175-2186.

Chen, B., Wang, B., Duan, M., Ma, X., Hong, J., Xie, F., Zhang, R. and Li, X., 2019. In search of key: Protecting human health and the ecosystem from water pollution in China. *Journal of Cleaner Production*, 228, pp. 101–111.

Cheng, X. and Li, X., 2018. Preparation and application of biochar-based catalysts for biofuel production. *Catalysts*, 8(9), pp. 346.

D'Anthony, B. M., Iraca, F. and Romero, M., 2017. *Color removal from textile effluents by biological processes*. Italy: Panta Rei Water Solutions.

Das, A., Nikhil, S. K. and Nair, R. G., 2019. Influence of surface morphology on photocatalytic performance of zinc oxide: A review. *Nano-structure & nano-objects*, 19, pp. 1-18.

Deng, Y. and Zhao, R., 2015. Advanced oxidation processes (AOPs) in wastewater treatment. *Current Pollution Report*, 1(3), pp. 167-176.

Department of Environment (DOE), 2018. *Environment quality report: pollution sources inventory*. [pdf] Malaysia: DOE. Available at: <<https://www.doe.gov.my/portalv1/wp-content/uploads/2018/09/BebanPencemaran.pdf>> [Accessed 30 May 2019].

Desipio, M. M., Bramer, S. E. V., Thorpe, R. and Saha, D., 2019. Photocatalytic and photo-fenton activity of iron oxide-doped carbon nitride in 3D printed and LED driven photon concentrator. *Journal of Hazardous Materials*, 376, pp. 178-187.

Dutrow, B. L. and Clark, C. M., 2019. *X-Ray powder diffraction*. [online] Available at: <[https://serc.carleton.edu/research\\_education/geochemsheets/techniques/XRD.html](https://serc.carleton.edu/research_education/geochemsheets/techniques/XRD.html)> [Accessed 16 June 2019].

EPA Victoria, 2018. *Point and nonpoint sources of water pollution*. [online] Available at: <<https://www.epa.vic.gov.au/your-environment/water/protecting-victorias-waters/point-and-nonpoint-sources-of-water-pollution>> [Accessed 30 May 2019].

Farahmandjou, M. and Jurablu, S., 2014. Co-precipitation synthesis of zinc oxide (ZnO) nanoparticles by zinc nitrate precursor. *International Journal of Bio-Inorganic Hybrid Nanomaterials*, 3(3), pp. 179-184.

Farahmandjou, M. and Soflaee, F., 2015. Synthesis and characterization of  $\alpha$ -Fe<sub>2</sub>O<sub>3</sub> nanoparticles by simple co-precipitation method. *Physical Chemistry Research*, 3(3), pp. 193-198.

Fazal, T., Razzaq, A., Javed, F., Hafeez, A., Rashid, N., Amjad, U. S., Regman, M., Faisal, A. and Rehman, F., 2019. Integrating adsorption and photocatalysis: A cost effective strategy for textile wastewater treatment using hybrid biochar-TiO<sub>2</sub> composite. *Journal of Hazardous Materials*, 390, pp. 1-14.

Foo, K. Y. and Hameed, B. H., 2010. An overview of dye removal via activated carbon adsorption process. *Desalination and Water Treatment*, 19(1-3), pp. 255-274.

Gholami, P., Dinpazhoh, L., Khataee, A. and Orooji, Y., 2019. Sonocatalytic activity of biochar-supported ZnO nanorods in degradation of Gemifloxacin: Synergy study, effect of parameters and phytotoxicity evaluation. *Ultrasonic-Sonochemistry*, 55, pp.44-56.

Gnanaprakasam, A., Sivakumar, V. and Thirumarimurugan, M., 2015. Influencing parameters in the photocatalytic degradation of organic effluent via nanometal oxide catalyst: A review. *Indian Journal of Material Science*, 15, pp. 1-16.

Gosh, M., 2018. *The future of water treatment: Advanced oxidation process*. [online] Available at: <<https://iwa-network.org/the-future-of-water-treatment-advanced-oxidation-process/>> [Accessed 6 June 2019].

Gu, D., Guo, C., Lv, J., Hou, S., Zhang, Y., Feng, Q., Zhang, Y. and Xu, J., 2019. Removal of methamphetamine by UV-activated persulfate: Kinetics and mechanisms. *Journal of Photochemistry and Photobiology A: Chemistry*, 379, pp. 32-38.

Hao, Z., Wang, C., Yan, Z., Jiang, H. and Xu, H., 2018. Magnetic particles modification of coconut shell-derived activated carbon and biochar for effective removal of phenol from water. *Chemosphere*, 211, pp. 962-969.

Hariz, A. R., Azlina, W. A. K. G., Fazly, M., Norziana, Z. Z., Ridzuan, M. D., Tosiah, S. and Ain, A. B., 2015. Local practises for production of rice husk biochar and coconut shell biochar: Production methods, product characteristics, nutrient and field water holding capacity. *Journal of Tropical Agriculture and Food Science*, 43(1), pp. 91-101.

Hassan, M. A. and Nemr, A. E., 2017. Health and environmental impact of dyes: Mini review. *American Journal of Environmental Science and Engineering*, 1(3), pp. 64-67.

Jeon, P., Lee, M. E. and Baek, K., 2017. Adsorption and photocatalytic activity of biochar with graphitic carbon nitride (g-C<sub>3</sub>N<sub>4</sub>). *Journals of the Taiwan Institute of Chemical Engineers*, 77, pp. 244-249.

Jiang, F., Qiu, B. and Sun, D., 2018. Advanced degradation of refractory pollutants in incineration leachate by UV/peroxymonosulfate. *Chemical Engineering Journal*, 349, pp.338-346.

Joseph, E. and Singhvi, G., 2019. *Nanomaterials for drug delivery and therapy*. New York: William Andrew Publisher.

Joshi, M. and Bhattacharyya, A., 2008. Characterization techniques for nanotechnology applications in textiles. *Indian Journal of Fibre and Textile Research*, 33(3), pp. 304-317.

Kamali, K. Z., Alagarsamy, P., Huang, N. M., Ong, B. H. and Lim, H. N., 2014. Hematite nanoparticles-modified electrode based electrochemical sensing platform for dopamine. *The Scientific World Journal*, 14, pp. 1-13.

Kandisa, R. V., Saibaba, K. V. N., Shaik, K. B. and Gopinath. R., 2016. Dye removal by adsorption: A review. *Journal of Bioremediation & Biodegradation*, 7, pp. 1-10.

Khan, M. M., Adil, S. F. and Al-Mayouf, A., 2015. Metal oxides as photocatalyst. *Journal of Saudi Chemical Society*, 19(5), pp. 462-464.

Khataee, A., Kayan, B., Gholami, P., Kalderis, D. and Akay, S., 2017. Sonocatalytic degradation of an anthraquinone dye using TiO<sub>2</sub>-biochar nanocomposite. *Ultrasonics-Sonochemistry*, 39, pp. 120-128.

Kim, J. R. and Kan, E., 2016. Heterogeneous photocatalytic degradation of sulfamethoxazole in water using a biochar-supported TiO<sub>2</sub> photocatalyst. *Journal of Environmental Management*, 180, pp. 94-101.

Kumar, A. and Pandey, G., 2017. A review on factors affecting the photocatalytic degradation of hazardous materials. *Material Science and Engineering International Journal*, 1(3), pp. 106-114.

Lade, H., Kadam, A., Paul, D. and Govindwar, S., 2015. Biodegradation and detoxification of textile azo dyes by bacterial consortium under sequential microaerophilic/ aerobic processes. *EXCLI Journal*, 14, pp. 158-174.

Lee, J., Kim, K. H. and Kwon, E. E., 2017. Biochar as a catalyst. *Renewable and Sustainable Energy Reviews*, 77, pp. 70-79.

LibreTexts, 2019. *Second-order reactions*. [online] Available at: <[https://chem.libretexts.org/Bookshelves/General\\_Chemistry/Map%3A\\_General\\_Chemistry\\_\(Petrucci\\_et\\_al.\)/14%3A\\_Chemical\\_Kinetics/14.06%3A\\_Second-Order\\_Reactions](https://chem.libretexts.org/Bookshelves/General_Chemistry/Map%3A_General_Chemistry_(Petrucci_et_al.)/14%3A_Chemical_Kinetics/14.06%3A_Second-Order_Reactions)> [Accessed 22 June 2019].

Li, K., Huang, Z., Zhu, S., Luo, S., Yan, L., Dai, Y., Guo, Y. and Yang, Y., 2019. Removal of Cr(IV) from water by a biochar-coupled g-C<sub>3</sub>N<sub>4</sub> nanosheets composite and performance of a recycled photocatalyst in single and combined pollution system. *Applied Catalyst B: Environmental*, 243, pp. 386-396.

- Li, X., Qian, X., An, X. and Huang, J., 2019. Preparation of a novel composite comprising biochar skeleton and “chrysanthemum” g-C<sub>3</sub>N<sub>4</sub> for enhanced visible light photocatalytic degradation of formaldehyde. *Applied Surface Science*, 487, pp. 1262-1270.
- Lu, L., Shan, L., Shi, Y., Wang, S. and Yuan, H., 2019. A novel TiO<sub>2</sub>/biochar composite catalyst for photocatalytic degradation of methyl orange. *Chemosphere*, 222, pp. 391-398.
- Lyon, 2010. *Some aromatic amines, organic dyes and related exposure*. France: International Agency for Research on Cancer.
- Mallick, P. and Dash, B. N., 2013. X-ray diffraction and UV-visible characterization of  $\alpha$ -Fe<sub>2</sub>O<sub>3</sub> nanoparticles annealed at different temperature. *Nanoscience and Nanotechnology*, 3(5), pp. 130-134.
- Martinez, C. R., Joshi, P., Vera, J. L., Ramirez-Vick, J. E., Perales, O. and Singh, P., 2011. Cytotoxic studies of PEG functionalized ZnO nanoparticles on MCF-7 cancer cells. *NSTI-Nanotech*, 3, pp. 420-423.
- Mazille, F. and Spuhler, D., 2019. *Advanced oxidation process*. [online] Available at: <<https://sswm.info/sswm-university-course/module-6-disaster-situations-planning-and-preparedness/further-resources-0/advanced-oxidation-processes>> [Accessed 6 June 2019].
- McLaughlin, H., 2016. *An overview of the current biochar and activated carbon markets*. [online] Available at: <<https://www.biofuelsdigest.com/bdigest/2016/10/11/an-overview-of-the-current-biochar-and-activated-carbon-markets/>> [Accessed 13 June 2019].
- Medien, H. A. A. and Khalil, S. M. E., 2010. Kinetics of the oxidative decolourization of some organic dyes utilizing Fenton-like reaction in water. *Journal of King Saud University*, 22, pp. 147-153.
- Mishra, M. and Chun, D., 2015.  $\alpha$ -Fe<sub>2</sub>O<sub>3</sub> as a photocatalytic material: A review. *Applied Catalyst A: General*, 498, pp. 126-141.
- Mishra, N. S., Reddy, R., Kuila, A., Rani, A., Mukherjee, P., Nawaz, A. and Saravanan, P., 2017. A review on advanced oxidation processes for effective water treatment. *Current World Environment*, 12(3), pp. 470-490.
- Mortazavian, S., Saber, A. and James, D. E., 2019. Optimization of photocatalytic degradation of Acid Blue 113 and Acid Red 88 textile dyes in a UV-C/TiO<sub>2</sub> suspension system: Application of response surface methodology (RSM). *Catalyst*, 9(4), pp. 1-19.
- Nanakoudis, A., 2018. *EDX analysis with a scanning electron microscope (SEM): How does it works*. [online] Available at: <<https://blog.phenom-world.com/edx-analysis-scanning-electron-microscope-sem>> [Accessed 16 June 2019].

- Neetha, J. N., Sandesh, K., Kumar, K. G., Chidananda, B. and Ujwal, P., 2019. Optimization of direct blue-14 dye by *Bacillus Fermus* (Kx898362) an alkaliphilic plant endophyte and assessment of degraded metabolite toxicity. *Journal of Hazardous Materials*, 364, pp. 742-751.
- Nemr, A. E., Hassaan, M. A. and Madkour, F. F., 2018. Advanced oxidation process (AOP) for detoxification of acid red 17 dye solution and degradation mechanism. *Environmental Processes*, 5(1), pp. 95–113.
- Niu, P., 2013. Photocatalytic degradation of Methyl Orange in aqueous TiO<sub>2</sub> suspensions. *Asian Journal of Chemistry*, 25(2), pp. 1103-1106.
- Nqombolo, A., Mpupa, A., Moutloali, R. M. and Nomngongo, P. N., 2017. *Wastewater treatment using membrane technology*. [online] Available at: <<https://www.intechopen.com/books/wastewater-and-water-quality/wastewater-treatment-using-membrane-technology>> [Accessed 4 June 2019].
- Pawar, V. and Gawande, S., 2015. An overview for the Fenton process for industrial wastewater. *IOSR Journal of Mechanical and Civil Engineering*, 2, pp. 127-136.
- Peng, L., Zheng, R., Feng, D., Yu, H. and Dong, X., 2020. Synthesis of eco-friendly porous g-C<sub>3</sub>N<sub>4</sub>/SiO<sub>2</sub>/SnO<sub>2</sub> composite with excellent visible-light responsive photocatalysis. *Arabian Journal of Chemistry*, 13(2), pp. 4275 - 4285.
- Petrier, C., 2015. The use of power ultrasound for water treatment. *Application of high intensity ultrasound*, pp. 939-972.
- Pi, L., Jiang, R., Zhou, W., Zhu, H., Xiao, W., Wang, D. and Mao, X., 2015. g-C<sub>3</sub>N<sub>4</sub> modified biochar as an adsorptive and photocatalytic material for decontamination of aqueous organic pollutants. *Applied Surface Science*, 358, pp. 231-239.
- Premarathna, K. S. D., Rajapaksha, A. U., Sarkar, B., Kwon, E. E., Bhatnagar, A., Ok, Y. S. and Vithanage, M., 2019. Biochar-based engineered composites for sorptive decontamination of water: A review. *Chemical Engineering Journal*, pp. 536–550.
- Qi, H., Baoshun, L., Zhengzhong, Z., Mingxia, S. and Xiujian, Z., 2010. Temperature effect on the photocatalytic degradation of Methyl Orange under UV-vis light irradiation. *Journal of Wuhan University of Technology*, 25(2), pp. 210-213.
- Ragnar, M., Eriksson, T. and Reitberger, T., 1999. Radical formation in ozone reactions with lignin and carbohydrate model compounds. *Holzforschung*, 53(3), pp. 292-298.

Rajapaksha, A. U., Chen, S. S., Tsang, D. C. W., Zhang, M., Vithanage, M., Mandal, S., Gao, B., Bolan, N. S. and Ok, Y. S., 2016. Engineered/designer biochar for contaminant removal/immobilization from soil and water: Potential and implication of biochar modification. *Chemosphere*, 148, pp. 276-291.

Raja, P. and Barron, A., 2012. *Physical methods in chemistry and nanoscience*. Rice University: OpenStax CNX.

Rajeswari, K., Subashkumar, R. and Vijayaraman, K., 2011. Biodegradation of mixed textile dyes by bacterial strains isolated from dyewaste effluent. *Research Journal of Environmental Toxicology*, 5(2), pp. 97-107.

Raju, R. and Rao, G., 2017. Assessment of tribological performance of coconut shell ash particle reinforced Al-Si-Fe composites using grey-fuzzy approach. *Tribology in Industry*, 39(3), pp. 364-377.

Rangabhashiyam, S., Anu, N. and Selvaraju, N., 2013. Sequestration of dye from textile industry wastewater using agricultural waste products as adsorbents. *Journal of Environmental Chemical Engineering*, 1(4), pp. 629–641.

Rodriguez, A., Rosal, R., Perdigon, J. A., Mezcua, M., Aguera, A., Hernando, M. D., Leton, P., Fernandez, A. R. and Garcia, E., 2008. *Emerging contaminants from industrial and municipal waste. The handbook of environmental chemistry: Removal technologies*. 1<sup>st</sup> Edition. Berlin: Springer-Verlag.

Rodriguez, S. G., Rodriguez, E., Singh, D. N. and Chueca, J. R., 2018. Assessment of sulfate radical-based advanced oxidation processes for water and wastewater treatment: A review. *Water*, 10(12), pp. 1-19.

Rout, T., Pradhan, D., Singh, R. and Kumari, N., 2016. Exhaustive study of products obtained from coconut shell pyrolysis. *Journal of Environmental Chemical Engineering*, 4, pp. 3696-3705.

Saien, J. and Soleymani, A. R., 2014. UV/persulfate and UV/hydrogen peroxide processes for the treatment of salicylic acid: Effect of operating parameters, kinetic and energy consumption. *Desalination and Water Treatment*, 56(11), pp. 1-9.

Saja, S. and Haider, R., 2016. New route for synthesis of pure anatase TiO<sub>2</sub> nanoparticles via ultrasound-assisted sol-gel method. *Journal of Chemical and Pharmaceutical Research*, 8(2), pp. 620-626.

Salleh, M. A. M., Mahmoud, D. K., Karim, W. A. and Idris, A., 2011. Cationic and anionic dye adsorption by agricultural solid waste: A comprehensive review. *Desalination*, 280(1-3), pp. 1-13.

Silvestri, S., Goncalves, M., Veiga, P., Matos, T., Zamora, P. and Mangrich, A., 2019. TiO<sub>2</sub> supported on *Salvinia molesta* biochar for heterogenous photocatalytic degradation of Acid Orange 7 dye. *Journal of Environmental Chemical Engineering*, 7(1), pp. 1-8.

Sivarajasekar, N. and Baskar, R., 2015. Agriculture waste biomass valorisation for cationic dye sequestration: A concise review. *Journal of Chemical and Pharmaceutical Research*, 7(9), pp. 737-748.

Speight, J. G., 2017. Transformation of inorganic chemicals in the environment. *Environmental Inorganic Chemistry for Engineers*, pp. 333-382.

Sun, Y., Yu, I. K. M., Tsang, D. C. W., Cao, X., Lin, D., Wang, L., Graham, N. J. D., Alessi, D. S., Komarek, M., Ok, Y. S., Feng, Y. and Li, X. D., 2019. Multifunctional iron biochar composites for the removal of potentially toxic elements, inherent cations, and hetero-chloride from hydraulic fracturing wastewater. *Environmental International*, 124, pp. 521-532.

Taweel, S and Saud, S., 2016. New route for synthesis of pure anatase TiO<sub>2</sub> nanoparticles via ultrasound-assisted sol-gel method. *Journal of Chemical and Pharmaceutical Research*, 8(2), pp. 620-626.

Terracciano, A., Christodoulatos, C., Koutsospyros, A., Zheng, Z., Su, T. L., Smolinski, B., Arienti, P. and Meng, X., 2018. Degradation of NTO in wastewater with UV/H<sub>2</sub>O<sub>2</sub> oxidation. *Chemical Engineering Journal*, 354, pp. 481-494.

Tsamo, C., Assabe, M., Argue, J. and Ihimbru, S. O., 2019. Discoloration of methylene blue and slaughter house wastewater using maize cob biochar produced using a constructed burning chamber: A comparative study. *Scientific African*, 3, pp. 1-13.

Verma, A. K., Dash, R. R. and Bhunia, P., 2012. A review on chemical coagulation/flocculation technologies for removal of colour from textile wastewaters. *Journal of Environmental Management*, 93(1), pp. 154-168.

Wang, J. L. and Wang, S. Z., 2018. Activation of persulfate (PS) and peroxymonosulfate (PMS) and application for the degradation of emerging contaminants. *Chemical Engineering Journal*, 334, pp. 1502-1517.

Wang, J. L. and Xu, L. J., 2012. Advanced oxidation processes for wastewater treatment: Formation of hydroxyl radical and application. *Critical Review in Environmental Science and Technology*, 42(3), pp. 251-325.

Winter, A., 2016. *Organic chemistry 1 for dummies, second edition*. [e-book] US: John Wiley & Son. Available through: Dummies website <<https://www.dummies.com/education/science/chemistry/how-to-find-functional-groups-in-the-ir-spectrum/>> [Accessed 17 June 2019].

Xie, J. and Li, X., 2016. A review on g-C<sub>3</sub>N<sub>4</sub>-based photocatalyst. *Applied Surface Science*, 391, pp. 52.

Xie, S., Huang, P., Kruzic, J., Zheng, X. and Qian, H., 2016. A highly efficient degradation mechanism of Methyl Orange using Fe-based metallic glass powders. *Scientific Reports*, 6, pp. 1-10.

Xu, H. Y., Wu, L. C., Zhao, H., Jin, L. G. and Qi, S. Y., 2015. Synergic effect between adsorption and photocatalysis of metal-free g-C<sub>3</sub>N<sub>4</sub> derived from different precursors. *Public Library of Science*, 10(11), pp. 1-20.

Yang, S., Wang, P., Yang, X., Shan, L., Zhang, W., Shao, X. and Niu, R., 2010. Degradation efficiencies of azo dye Acid Orange 7 by the interaction of heat, UV and anions with common oxidants: Persulfate, peroxy monosulfate and hydrogen peroxide. *Journal of Hazardous Materials*, 179(1-3), pp. 552-558.

Yaseen, D. A. and Scholz, M., 2018. Textile dye wastewater characteristics and constituents of synthetic effluents: A critical review. *International Journal of Environmental Science and Technology*, 16(2), pp. 1193-1226.

Yu, L., Huang, Y., Yang, Y., Xu, Y., Wang, G. and Yang, S., 2013. Photocatalytic degradation of organic dye by H<sub>4</sub>SiW<sub>6</sub>MO<sub>6</sub>O<sub>40</sub>/SiO<sub>2</sub> sensitized by H<sub>2</sub>O<sub>2</sub>. *International Journal of Photoenergy*, 1, pp. 1-7.

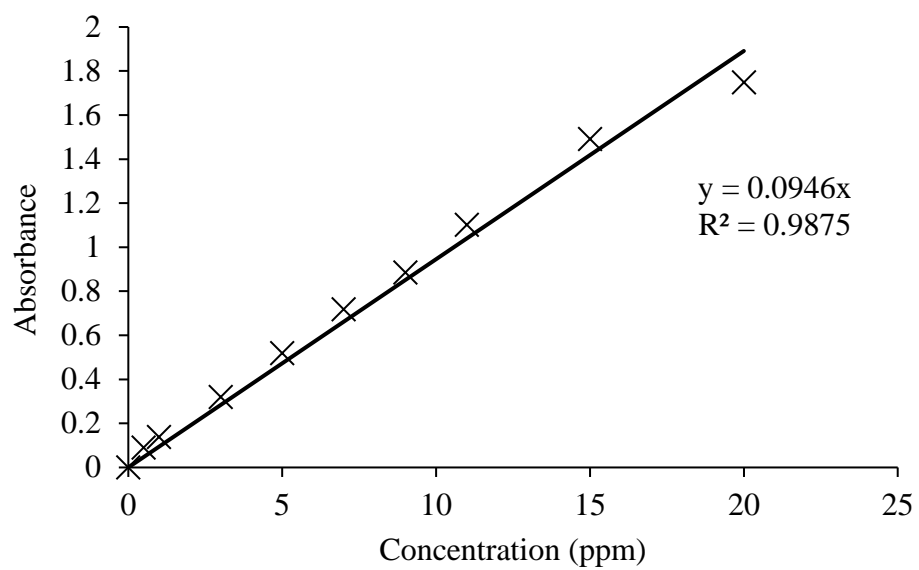
Zakaria, H., Mansor, W. and Shahrin, N., 2018. Development of water treatment sachets from the seeds of moringa oliefera and activated carbon. *International Journal of Science and Technology*, 3(3), pp. 240-252.

Zhang, L., Tu, L., Liang, Y., Chen, Q., Li, Z., Li, C., Wang, Z. and Li, W., 2018. Coconut-based activated carbon fibers for efficient adsorption of various organic dyes. *Royal Society of Chemistry*, 8(74), pp. 42280-42291.

Zhang, Y., Chen, T., Zhao, Y., Chen, D., Zhou, Y. and Liu, H., 2019. Catalytic effect of siderite on H<sub>2</sub>O<sub>2</sub> oxidation of carmine dye: Performance, mechanism and kinetics. *Applied Geochemistry*, 106, pp. 26-33.

Zhu, B., Xia, P., Ho, W. and Yu, H., 2015. Isoelectric point and adsorption activity of porous g-C<sub>3</sub>N<sub>4</sub>. *Applied Surface Science*, 344, pp. 188-195.

Zhu, Z., Cai, H. and Sun, D. W., 2018. Titanium dioxide photocatalysis technology for nonthermal inactivation of microorganisms in food. *Trends in Food Science & Technology*, 75, pp. 23-35.

**APPENDICES****APPENDIX A: Calibration Curve of Organic Dye**

Graph A-1: Calibration Curve of Methyl Orange